



# Proton Conduction in Metal-Organic Frameworks and Coordination Polymers Studied by Impedance Spectroscopy

Dissertation

approved for the attainment of the degree of

Doctor of Natural Sciences

(Dr. rer. nat.)

from the Faculty of Sciences of the University of Paderborn

Ali Javed

Paderborn, May 2022

The present work was carried out from June 2017 to December 2021 at the department of Chemistry at the University of Paderborn in the working group of Prof. Dr. Michael Tiemann.

Reviewer: Prof. Dr. Michael Tiemann

Prof. Dr. Claudia Schmidt

Day of Disputation: 19.05.2022

## STATEMENT OF AUTHORSHIP

By signing this document, I hereby certify that I completed my thesis independently with the indicated support and resources. This work has never been submitted to any examining authority previously in the same or similar form.

Paderborn, May 21, 2022

A handwritten signature in black ink, appearing to read "mfm".

## ACKNOWLEDGEMENTS

First and foremost, I would like to express my profound gratitude to my advisor Prof. Dr. Michael Tiemann for providing me this opportunity to join his lab and work on this project. Apart from that, his continuous support, motivation, patience, ideas and suggestions, and critical analysis on results have made this work possible. Whenever I fell into a snag or had a question regarding my research, the door to his office was always open. I was guided in the right direction as and when I needed it. I must declare that I have learnt a lot from him, and his trust in me has strengthened my confidence.

I thank to the board of examiners for conducting an evaluation of this thesis and introducing insightful comments. I must thank my collaboration partners for the excellent cooperation and joint publications. Particularly, I appreciate the enthusiasm and hard work of Dr. Hana Bunzen and Felix Steinke.

My sincere thanks to Dr. Christian Weinberger and Dr. Thorsten Wagner for the moral support and fruitful discussions. I would also like to thank the former and current fellow lab mates for assisting me when I absolutely required it, and great enjoyable working atmosphere especially in the coffee rounds.

Many thanks to “**DFG**” and “**COORNets**” for funding this research project and offering numerous opportunities to exhibit the research and discuss with other project and program members.

Most importantly, thanks to my family members for their genuine and explicit support.

## DEDICATION

*In honor of my father and late mother,  
who always encouraged me to pursue my ambitions.*

## TABLE OF CONTENTS

Chapter 1: Motivation .....	1
Chapter 2: Background.....	3
2.1 Introduction.....	3
2.2 Fuel Cells.....	4
2.3 Coordination Polymers (CPs) and Metal-Organic Frameworks (MOFs).....	9
2.4 Proton Conductivity.....	12
2.5 Activation Energy.....	13
2.6 Proton Conduction Mechanisms .....	15
Chapter 3: Methodology: The Fundamentals and Analysis Approach of Impedance Spectroscopy .....	17
3.1 Introduction.....	17
3.2 Basics of Impedance .....	18
3.3 Impedance of Ideal Circuit Elements.....	20
3.4 Impedance of Ideal Electrical Circuits .....	21
3.4.1 RC in Series Combination .....	21
3.4.2 RC in Parallel Combination .....	22
3.5 Impedance of Real Systems .....	25
3.6 Representation of Impedance Data .....	26
3.7 Relation between Impedance and Dielectric Spectroscopies .....	26
Chapter 4: Experimental Setup .....	28
Chapter 5: Publications .....	32
5.1 Proton Conduction in a Single Crystal of a Phosphonato-Sulfonate-Based Coordination Polymer: Mechanistic Insight .....	32
5.1.1 Outline and Outcome.....	32
5.1.2 Manuscript .....	34

5.1.3 Published Data Details.....	42
5.2 Humidity-Mediated Anisotropic Proton Conductivity through the 1D Channels of Co-MOF-74 .....	43
5.2.1 Outline and Outcome.....	43
5.2.2 Manuscript .....	44
5.2.3 Published Data Details.....	56
5.3 The Role of Sulfonate Groups and Hydrogen Bonding in the Proton Conductivity of Two Coordination Networks .....	59
5.3.1 Outline and Outcome.....	59
5.3.2 Manuscript .....	61
5.3.3 Published Data Details.....	72
5.4 Studies on a Fringing Electric Field Sensor (Unpublished) .....	75
Chapter 6: Synopsis of Thesis .....	80
6.1 Summary of Findings .....	80
6.2 Challenges and Perspectives .....	84
Bibliography.....	86
List of Tables .....	92
List of Figures.....	93
Appendix.....	96
List of Publications.....	96
List of Posters.....	97
Oral Presentations .....	97
Workshops.....	97
Curriculum Vitae.....	98

## LIST OF ABBREVIATIONS AND ACRONYMS

Metal-Organic Framework	MOF
Coordination Polymer	CP
Proton Exchange Membrane Fuel Cell	PEMFC
Impedance Spectroscopy	IS
Catalyst-Coated Membrane	CCM
Catalyst-Coated Substrate	CCS
Membrane Electrode Assembly	MEA
Gas Diffusion Layer	GDL
Hydrogen Oxidation Reaction	HOR
Oxygen Reduction Reaction	ORR
Acid Dissociation Constant	pKa
Carboxylic acid	CA
Phosphonic Acid	PA
Sulfonic Acid	SA
One-Dimensional	1D
Two-Dimensional	2D
Three-Dimensional	3D
Barium-based Coordination Polymer	Ba-CP
Cobalt-based Metal Organic Framework	Co-MOF-74
Magnesium-based Coordination Polymer	Mg-CP
Lead-based Metal Organic Framework	Pb-MOF
Equivalent Circuit Model	ECM
Mass Flow Controllers	MFCs
Potential	$U$
Electrical/Ionic/Proton Conductivity	$\sigma$
Current Density	$J$
Charge	$q$
Mobility of Mobile Charge	$\mu$
Velocity	$v$
Concentration of Mobile Charge	$n$
Activation Energy	$E_A$
Alternating Current	AC
Direct Current	DC
Impedance	$Z$
Real Part of Impedance	$Re(Z)$
Imaginary Part of Impedance	$Im(Z)$
Frequency	$f$
Angular Frequency	$\omega$
Resistance	$R$
Capacitance	$C$
Constant Phase Element	CPE
Phase-Sift	$\theta$
Time Constant	$\tau$

## ABSTRACT

The high proton conductivity and hydrothermal stability are common challenges to utilize porous and non-porous coordination networks in hydrogen fuel cell membranes. Numerous studies have revealed the vagueness in correlating proton conduction pathways with crystal structures of metal-organic frameworks (MOFs) and coordination polymers (CPs). This thesis discusses this subject and provides insight into anisotropic proton conduction mechanism.

Impedance spectroscopy was used to measure the proton conductivity of MOFs and CPs. Two setups were established to measure the impedance of single crystals (in-plane) and pellets (through-plane). The experiments were conducted under defined conditions at variable temperature and relative humidity.

The first part of the thesis is devoted to single crystal studies of a barium-based CP (**Ba-CP**),  $[\text{Ba}(\text{H}_3\text{L})(\text{H}_2\text{O})]\cdot\text{H}_2\text{O}$ , and cobalt-based MOF (**Co-MOF**), Co-MOF-74. Linear 1-dimensional pores in Co-MOF possess adsorbed water molecules, whereas channels in Ba-CP contain non-coordinating water molecules. Both materials show anisotropic proton conductivity and a hopping mechanism in the channels or pores running along the length of the crystal. The second part of the thesis is focused on studying proton conductivity in microcrystalline pressed powder samples of a magnesium-based CP (**Mg-CP**),  $[\text{Mg}(\text{H}_2\text{O})_2(\text{H}_3\text{L})]\cdot\text{H}_2\text{O}$ , and a lead-based MOF (**Pb-MOF**),  $[\text{Pb}_2(\text{HL})]\cdot\text{H}_2\text{O}$ . Although both materials contain the same linker molecule, their crystal structures differ significantly. This tended to a remarkable change in proton conductivity with very low conductivity in Pb-MOF, and moderate conductivity in Mg-CP. Furthermore, the coordinated sulfonate group in Pb-MOF did not provide a possibility for extended hydrogen bonding, while Mg-CP demonstrated proton hopping due to dangling sulfonate group.

This research was a part of the DFG Priority Program 1928 program “Coordination Networks: Building Blocks for Functional Systems”. The project focused on “Proton-conducting and hydrophilic coordination polymers - synthesis, spectroscopic investigation and incorporation into fuel cells”. In this project, the aim of this thesis was to characterize the novel materials through impedance spectroscopy. Therefore, the materials synthesis and their structural characterization was done by the collaboration partners. The dissertation is comprised of three key articles that were published in a systematic sequence.

## KURZFASSUNG

Die hohe Protonenleitfähigkeit und hydrothermale Stabilität sind allgemeine Herausforderungen bei der Verwendung poröser und nicht poröser Koordinationsnetzwerke in Wasserstoff-Brennstoffzellenmembranen. Zahlreiche Studien haben gezeigt, dass die Protonenleitwege nicht eindeutig mit den Kristallstrukturen von metallorganischen Gerüsten (MOFs) und Koordinationspolymeren (CPs) korreliert werden können. Die vorliegende Arbeit befasst sich mit diesem Thema und gibt Einblick in den Mechanismus der anisotropen Protonenleitung.

Zur Messung der Protonenleitfähigkeit von MOFs und CPs wurde die Impedanzspektroskopie eingesetzt. Es wurden zwei Versuchsaufbauten zur Messung der Impedanz von Einkristallen (in der Ebene) und Pellets (durch die Ebene) eingerichtet. Die Experimente wurden unter definierten Bedingungen bei variabler Temperatur und variabler relativer Luftfeuchtigkeit durchgeführt.

Der erste Teil der Arbeit befasst sich mit Untersuchungen zu Einkristallen eines bariumbasierten CP (**Ba-CP**)  $[\text{Ba}(\text{H}_3\text{L})(\text{H}_2\text{O})]\cdot\text{H}_2\text{O}$  und eines cobaltbasierten MOF (**Co-MOF**) Co-MOF-74. Die linearen, 1-dimensionalen Poren in Co-MOF besitzen adsorbierte Wassermoleküle, während die Kanäle in Ba-CP nicht-koordinierende Wassermoleküle enthalten. Beide Materialien zeigen eine anisotrope Protonenleitfähigkeit und einen Sprungmechanismus in den Kanälen oder Poren, die sich über die Länge des Kristalls erstrecken. Der zweite Teil der Arbeit konzentriert sich auf die Untersuchung der Protonenleitfähigkeit in mikrokristallinen, gepressten Pulverproben eines magnesiumbasierten CPs (**Mg-CP**),  $[\text{Mg}(\text{H}_2\text{O})_2(\text{H}_3\text{L})]\cdot\text{H}_2\text{O}$ , und eines bleibasierten MOFs (**Pb-MOF**),  $[\text{Pb}_2(\text{HL})]\cdot\text{H}_2\text{O}$ . Obwohl beide Materialien das gleiche Linkermolekül enthalten, unterscheiden sich ihre Kristallstrukturen erheblich. Dies führte zu einer bemerkenswerten Veränderung der Protonenleitfähigkeit mit sehr geringer Leitfähigkeit in Pb-MOF und mäßiger Leitfähigkeit in Mg-CP. Außerdem bot die koordinierte Sulfonatgruppe in Pb-MOF keine Möglichkeit für eine ausgedehnte Wasserstoffbrückenbindung, während Mg-CP aufgrund der beweglichen Sulfonatgruppe Protonensprünge zeigte.

Diese Arbeit war ein Teil des DFG-Schwerpunktprogramms 1928 "Koordinationsnetzwerke: Bausteine für funktionale Systeme". Das Projekt befasste sich mit dem Thema "Protonenleitende und hydrophile Koordinationspolymere - Synthese, spektroskopische

Untersuchung und Einbindung in Brennstoffzellen". Das Ziel dieser Arbeit war es, die neuartigen Materialien durch Impedanzspektroskopie zu charakterisieren. Daher wurde die Synthese der Materialien und ihre strukturelle Charakterisierung von den Kooperationspartnern durchgeführt. Die Dissertation besteht aus drei Schlüsselartikeln, die in systematischer Abfolge veröffentlicht wurden.

## Chapter 1: Motivation

Researchers must read a large number of papers to gain a comprehensive view of their research topic. The analysis of review articles can offer a valuable insight in understanding the general trends in the field. In 2021, 12418 and 3782 scientific articles were published on metal-organic frameworks (MOFs) and coordination polymers (CPs), respectively. In the previous two decades, the MOFs field has grown exponentially, as shown in Figure 1.1 (a). This is because MOFs have a great deal of potential in sectors including gas storage and transportation, gas separation, water sorption, catalysis, drug delivery, luminescence, and so on.<sup>[1-5]</sup> On the other hand, the growth in CPs publications is divided into two stages: (i) 2000-2010, which shows a gradual increase; and (ii) 2010-2020, which displays an almost steady phase. In short, MOFs research has been in full swing for the past decade, and this trend enables to predict that this number will continue to rise statistically. In respect of proton conductivity, 190 and 85 research articles were published in 2021 on MOFs and CPs, respectively.

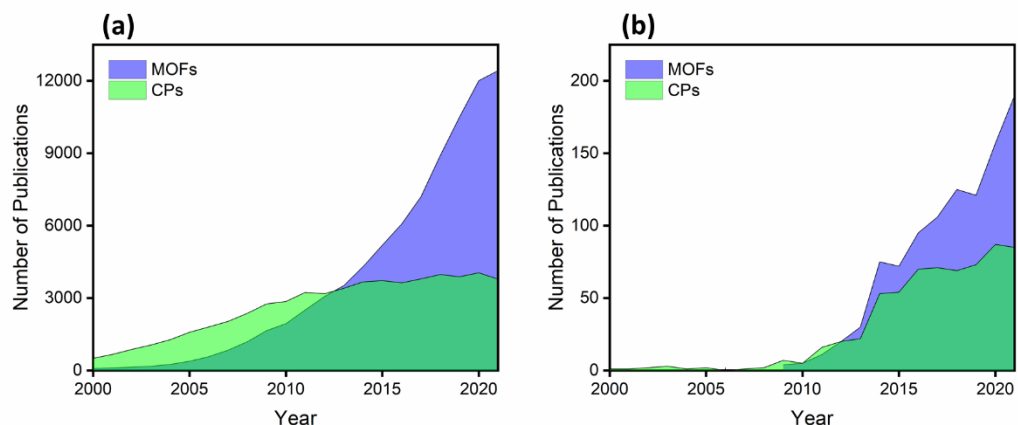


Figure 1.1: Chronological advancement on publications of MOFs and CPs: a) in all possible sectors, b) in proton conductance world (ISI Web of Science, accessed 18.01.2022).

The focus of this work is the implementation of MOFs and CPs for proton conducting applications, such as proton exchange membrane fuel cells, which plays an indispensable part in attaining today's green energy demands. The humidity dependence and high cost of benchmark Nafion membranes led scientists to explore new proton conducting materials. MOFs as well as CPs are promising systems in this regard.<sup>[6]</sup> Proton conductivity is frequently analyzed by impedance spectroscopy. Most of the time, the studies are performed by using powder samples in a pellet form, which bears some pitfalls, such as grain boundary effects,

impact of surface-adsorbed water, and difficulty to distinguish between intrinsic and extrinsic proton conduction mechanisms. These drawbacks can be alleviated by using a single crystal probe.<sup>[7]</sup> Most conveniently, this also offers an opportunity to study anisotropic effects in proton conductance. Therefore, in this work, impedance spectroscopic studies of proton conduction in single crystal as well as in pellets of MOFs and CPs were carried out. In addition to that, to prevent blockage of pores or channels, the electrical contact between sample and electrodes was established without using glue or conducting paste. Other approaches in the literature, particularly in the case of single crystal studies, reported the inclusion of additives.<sup>[8-14]</sup>

Concerning single crystals, a Ba-based coordination polymer (Ba-CP) and a Co-based metal-organic framework (Co-MOF) were examined in different orientations with varying humidity and temperature. Anisotropy revealed two distinct proton conduction processes in each crystal. A Mg-based coordination polymer (Mg-CP) and a Pb-based metal-organic framework (Pb-MOF) were investigated at macroscopic scale (samples in pellet form).

## Chapter 2: Background

### 2.1 Introduction

Population surge, energy dearth and global warming are the dilemma of the 21<sup>st</sup> century. These issues are interconnected, and the primary challenge is figuring out how to resolve them.<sup>[15]</sup> In mid-2019, the world's population was 7.7 billion people, with projections of 8.5 billion in 2030, 9.7 billion in 2050, and 10.9 billion in 2100.<sup>[16]</sup> According to this demographic prediction, the future energy demands can be fulfilled, if we will have enough energy resources. Most of today's energy demands are met by fossil fuels, although renewable energy resources continue to gain prominence. The excessive consumption of fossil fuels is producing a significant change in the earth's temperature and an increase in greenhouse gases emission.

At the "United Nations Climate Change Conference" held in 2015 in Paris, leaders from 195 countries committed to limiting global average temperature rise to 1.5 °C above pre-industrial levels. The goal of this agreement was to achieve net worldwide decarbonization of human activities by the year 2100, as this may be the only way to mitigate global warming effects.<sup>[17]</sup> In 2021, World Energy Outlook provided the details of how far the countries reach to fulfill the Paris agreement by their clean energy transition. In this regard, they have proposed that huge push in clean electrification, innovation in clean energy, improvement in energy efficiency, and leakage control of fossil-fuel operations are the key actions which should be adopted in next decades to keep the door open for 1.5 °C stabilization. Moreover, the net zero CO<sub>2</sub> emissions can be achieved by explosive growth in clean energy technology which only requires the unparallel clean energy investment.<sup>[18]</sup>

The combined size of clean energy market is comprised of wind turbine, solar panels, nuclear energy, lithium-ion batteries, electrolyzers and fuel cells. Currently, the rapid diffusion of these new energy technologies is impeded by high cost, technical flaws, limitation such as nuclear fusion, and public normalization. Therefore, the market does not encourage to deploy their use, even though they offer significant benefits such as minimal carbon emissions. Their development can be fostered by monetizing the social value they offer instead of putting prices on greenhouse gases and emissions.<sup>[19]</sup> The emphasis in this research work is to characterize novel functional materials for hydrogen fuel cell membrane, which are described in the following sections.

## 2.2 Fuel Cells

Fuel cells are electrochemical cells that convert the chemical energy of a fuel into electrical energy in a single step without utilizing any moving parts, by-passing all the steps involved in a traditional energy production unit (see Figure 2.1).<sup>[20,21]</sup> They are analogous to batteries, with the exception that batteries consume their electrodes when producing clean energy, whereas fuel cells do not use any of their components and produce green energy as long as fuel and oxidant are accessible.<sup>[22]</sup>

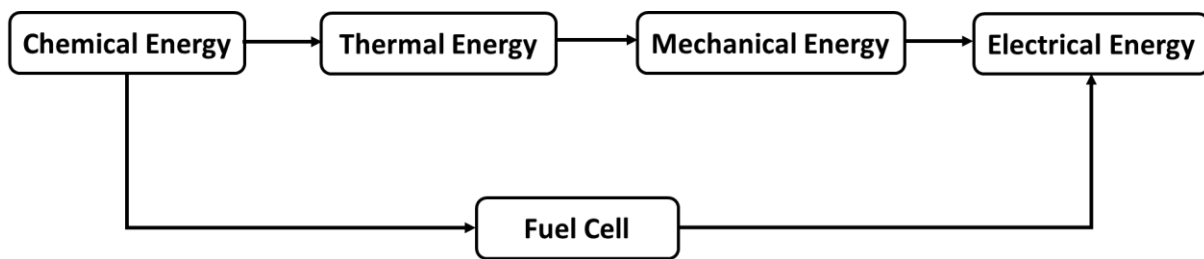


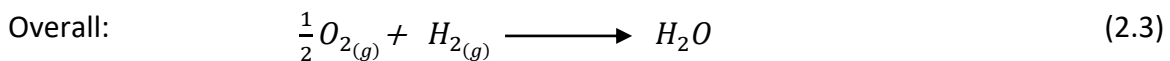
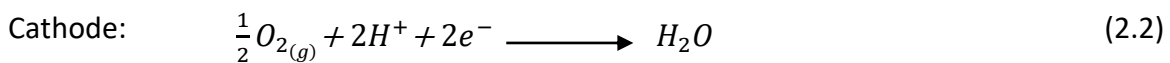
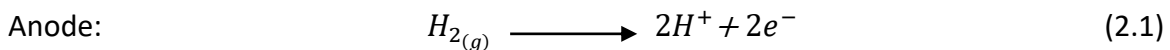
Figure 2.1: Flow diagram presenting the comparison of energy generation by conventional method and electrochemical process.

Fuel cells have a sandwich-like structure where an electrolyte is squeezed between two working electrodes known as anode and cathode. Fuel is supplied to the anode, and an oxidant to the cathode. The most commonly used oxidant is oxygen because of its abundance in nature and high reactivity, while the most efficient fuel is hydrogen due to its high electrochemical reactivity. Fuel and oxidant are supplied in the gaseous form and the electrolyte is used in the solid or liquid form.<sup>[23]</sup> Fuel cells are classified according to the substance used as an electrolyte. Different types of ions can conduct through the electrolyte, which is also depending on the operating temperature. The two types of fuel cells that can be used above 600 °C are solid oxide and molten carbonate. On the other hand, alkaline, phosphoric acid, and proton exchange membrane operate below 250 °C. Each type of fuel cell has advantages and disadvantages, the most significant of which is the use of noble metals as a catalyst. Low temperature fuel cells require an expensive catalyst to conduct an electrochemical reaction, and pure hydrogen gas as a fuel. On account of that, they have a rapid start-up time and low thermal deterioration. High temperature fuel cells, on the other hand, can be used directly with hydrocarbons without the use of rare metals as a catalyst. Nevertheless, they have a long start-up time and require a high temperature to commence the electrochemical process.<sup>[22,24,25]</sup> Table 2.1 contains the additional information.

Table 2.1: Characteristics of different types of fuel cells based on electrolyte material.<sup>[26]</sup>

Fuel Cell Type	Electrolyte Material	Charge Carrier	Operating Temperature (°C)	Efficiency (%)
<b>Solid Oxide</b>	Yttria-Stabilized Zirconia	O <sup>-2</sup>	600 – 1000	60 – 65
<b>Molten Carbonate</b>	Li/K or Li/Na Carbonates	CO <sub>3</sub> <sup>-2</sup>	600 – 650	45 – 60
<b>Alkaline</b>	Potassium Hydroxide	OH <sup>-</sup>	50 – 200	45 – 60
<b>Phosphoric Acid</b>	Phosphoric Acid	H <sup>+</sup>	180 – 210	40 – 45
<b>Proton Exchange Membrane</b>	Perfluorosulfonic Acid	H <sup>+</sup>	40 – 80	40 – 60

Since last decades the proton exchange membrane fuel cell (PEMFC) has got immense attraction and higher attention than other types of fuel cells due to its compact size, light weight, low temperature operation range, high efficiency, quick start-up, long life etc. The practical constraints of low temperature operation led PEMFC to three major categories: low temperature PEMFC (40-80) °C, medium temperature PEMFC (100-150) °C, and high temperature PEMFC (120-200) °C.<sup>[27]</sup> A polymer solid electrolyte is fused between the anode and cathode electrodes in a common structure of single PEMFC (see Figure 2.2). Hydrogen gas is used as a fuel at the anode, where protons and electrons are released on the catalyst's surface. Protons go via the electrolyte while electrons travel through an external circuit, eventually meeting at the cathode. The electrons transform the oxidant into oxide ions, and the electrochemical process is completed at the three-phase boundary region of the catalyst on the cathode side, where electrons, protons, and oxidant interact. As a result, green energy is generated with minimal toxic emissions and heat, as well as water. The excess airflow at the cathode side washes away the produced water. Equations 2.1 to 2.3 illustrate the chemical reactions that take place in a PEMFC.<sup>[28]</sup>



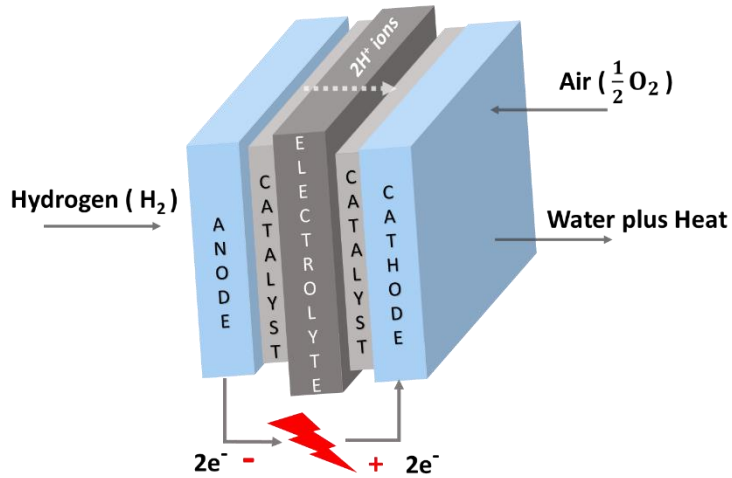


Figure 2.2: Schematic diagram presenting the operating principle of single PEMFC.

A single PEMFC can generate a maximum output voltage of 0.8 V. The output can be enhanced by connecting more cells in series and stacking them like batteries. The primary components of single PEMFC are endplates and flow-fields, sealing material, gas diffusion layer (GDL) and catalyst-coated membrane (CCM). The core component of the cell is membrane electrode assembly (MEA), which is comprised of GDL and CCM and that is where electrochemical reactions take place. The most common methods to fabricate MEA are the deposition of catalyst on the membrane (mentioned above as CCM) or the deposition of catalyst over the substrate, known as catalyst-coated substrate (CCS), where carbon black serves as substrate. Porous carbon material is used as an electrode that contains highly dispersed platinum (Pt) nanoparticles in order to improve the surface area to volume ratio and prevent the Pt-agglomeration.<sup>[29,30]</sup> Pt or Pt-alloys are employed as a catalyst due to its high electro-catalytical activity, excellent stability, and good electrical conductivity. Pt is recognized a benchmark material for hydrogen oxidation reaction (HOR) at anode, and oxygen reduction reaction (ORR) at cathode of PEMFC.<sup>[31,32]</sup> The heart of MEA is a polymer membrane which allows the protons to conduct and inhibits the electrons to transfer from anode to cathode. Perfluorosulfonic acid membrane, which is also known as “Nafion”, is the most extensively used electrolyte material for PEMFC applications because of its high proton conductivity, strong chemical stability, and outstanding performance under the mild conditions. The outer-layer of MEA is GDL, which acts as an interface between MEA and flow-fields, distributing reactant gases from flow-fields to the catalyst layer and transporting generated water, heat, and electrons from the electrode to the flow-fields. Hence, GDL should have high porosity, low

electrical resistance, and high thermal conductivity.<sup>[33]</sup> GDL is made of a carbon fiber paper (gas diffusion substrate), and a microporous carbon layer. Using a polytetrafluoroethylene coated fiberglass gasket as a sealing material, GDL and MEA are merged between two flow-fields. The flow-fields, made of graphite or graphite composites, have precise flow-patterns machined onto its surfaces that serve as a path for the reactant gases to pass through.

This study is motivated by the objective of discovering new proton conducting materials; hence a special focus is devoted to PEM materials in the following. In the recent decades, there has been an exponential increase in the development of new proton conducting membranes for PEMFCs.<sup>[34]</sup> The promising candidate must satisfy a number of characteristics, including high proton conductivity ( $> 0.01 \text{ S/cm}$ ), chemical and thermal stability, compatibility with other cell components, thin-film mechanical strength, low permeability to reactant gases ( $\text{H}_2$  and  $\text{O}_2$ ), and low-cost large-scale production.<sup>[35]</sup>

Until now, a significant number of proton-conducting membranes have been synthesized and characterized, which have been categorized into 3 families.<sup>[36]</sup> The fluorine-containing polymers, also known as perfluorosulfonic acid polymers, are the first of them. The benchmark material for the PEM fuel cell industry "Nafion" belongs to this class.<sup>[37]</sup> These materials offer good chemical and thermal stability, as well as high proton conductivity at high relative humidity and temperatures below 90 °C.<sup>[38]</sup> Above 100 °C, the PEMFC operation is advantageous because it enhances electrode kinetics, decreases catalytic poisoning, and simplifies water and thermal management.<sup>[39]</sup> The loss of water molecules from "Nafion" due to elevated temperatures causes a decrease in proton conductivity. As a result, contemporary research has shifted its focus to intermediate and high temperature PEMFCs, limiting the use of "Nafion", which can only function at temperature (50-90) °C.<sup>[27]</sup>

The second group of proton conducting materials is sulfonated aromatic polymers which are non-fluorinated. The most extensively investigated polymers for fuel cell applications are sulfonated poly(arylene ether ketone)-(SPAEK), and poly(ether ether ketone)-(SPEEK). Chemical modifications, such as sulfonation of the aromatic position, improve their proton conductivity based on enhanced hydrophilicity and acidity.<sup>[40]</sup> SPEEK can be used in intermediate temperature PEMFCs due to its high thermal, mechanical, and chemical stability. However, the shorter lifetime of SPEEK than Nafion under the same conditions and drop in conductivity above 120 °C restrict its use to temperature range (80-120) °C. Interestingly,

another polymer, polyphenylene, which belongs to the same class has showed improved stability under the same conditions.<sup>[41–43]</sup>

Heterocyclic aromatic compounds, including polybenzimidazole derivatives, constitute the third group of materials.<sup>[44]</sup> They are a viable contender for high temperature PEMFC because of their strong thermal stability, and high resistance to inorganic acidic and basic chemicals.<sup>[45]</sup> The materials' low conductivity necessitates doping with an inorganic acid such as phosphoric acid, which has enabled it to achieve 0.1 S/cm conductivity under dry conditions. The usage of inorganic acids causes some severe drawbacks, such as acid-leaching which leads to membrane degradation. Other inorganic acids, which are unable to achieve such high conductivity, were used as a dopant to mitigate these adverse effects.<sup>[46–51]</sup>

The above-mentioned families of materials do not satisfy all the criteria for use as a membrane in a PEMFC. Many of them fulfill the physical requirements but do not provide adequate proton conductivity. Therefore, the preparation of mixed-matrix-membranes (MMMs) is a widely used method, which involves the mixing of polymer matrix with inorganic materials. The inorganic phase improves the physical properties, water-uptake, and proton conductivity while the polymer matrix provides flexibility and ion exchange capacity. As inorganic fillers zeolites, carbon nanotubes, mesoporous inorganic oxides, graphene, and MOFs have been studied extensively,<sup>[27,52]</sup> but only MOFs and CPs are investigated in this study to determine their proton conducting behavior.

## 2.3 Coordination Polymers (CPs) and Metal-Organic Frameworks (MOFs)

Coordination polymers (CPs) are compounds containing metal centers, coordinated by organic molecules, and linked in at least one dimension to form a polymer. According to IUPAC, coordinated polymers are compounds that repeat in at least one dimension via coordination units. In the case of two or three dimensions of linkage, the term "coordination network" is used. If a coordination network exhibits porosity as part of the crystal structure, they are usually referred to as metal-organic frameworks (MOFs).<sup>[53]</sup>

Hybrid inorganic-organic crystalline materials such as MOFs or porous CPs are formed by linking two basic building blocks: organic ligands and inorganic metal nodes.<sup>[54]</sup> It is an emerging class of functional materials that have been intensively studied in the last two decades for gas storage/separation, energy storage and conversion, sensing, catalysis, ionic conductors, etc.<sup>[55,56]</sup> This is due to their porosity, high surface areas, and tunability. In contrast with conventional proton conductors used in PEMFC, MOFs have several advantages, such as their designability, tunable properties, and chemical and thermal stability.<sup>[57]</sup>

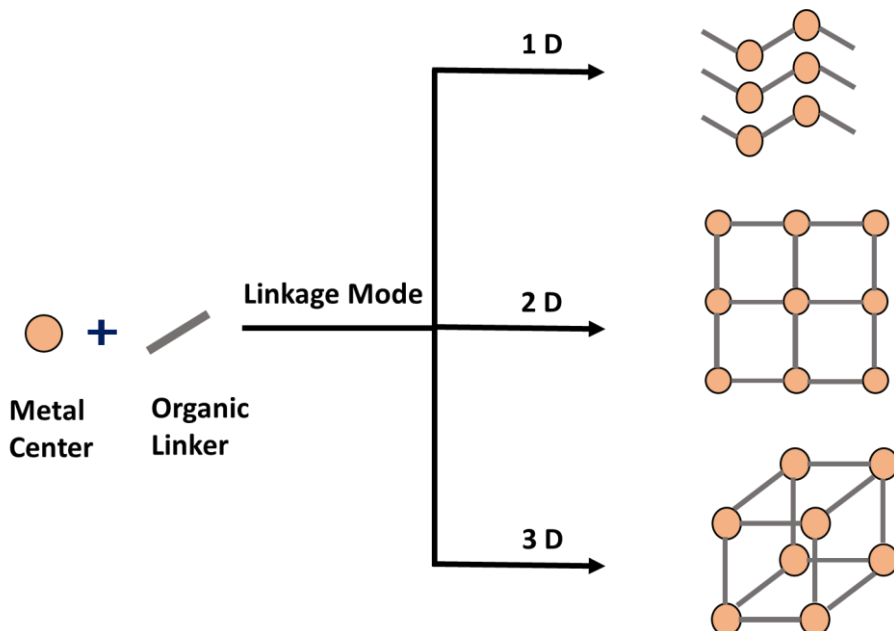


Figure 2.3: Schematic structure of 1D, 2D and 3D coordination networks.

MOFs can be divided into two categories according to their proton conductivity. The first type involves proton conducting MOFs that work at low temperatures (20-80) °C. In these MOFs, water-mediated hydrogen bonding networks provide pathways for protons to pass through. The second type of MOFs is anhydrous that conduct at high temperatures (100-250) °C. These MOFs have water-free pathways for the protons to conduct.<sup>[58,59]</sup> In MOFs, the concentration

and mobility of proton carriers can tune their proton conductivity. The concentration of proton carriers is determined by the total acidity of proton sources, while proton mobility is aided by the presence of a continuous H-bond network comprising protic sites.<sup>[60]</sup> There have been three types of sources recently reported in literature that have the potential to improve the proton conductivity of MOFs: (i) modification of the bridging ligands with functional groups, such as -OH, -COOH, -PO<sub>3</sub>H<sub>2</sub>, or -SO<sub>3</sub>H, (ii) introduction of acidic guest molecules into the pores, such as hydronium ions, organic and inorganic acids, ammonium cations, and N-heterocycles, (iii) encapsulation of protic organic molecules into pores, such as imidazole and histamine.<sup>[59-62]</sup>

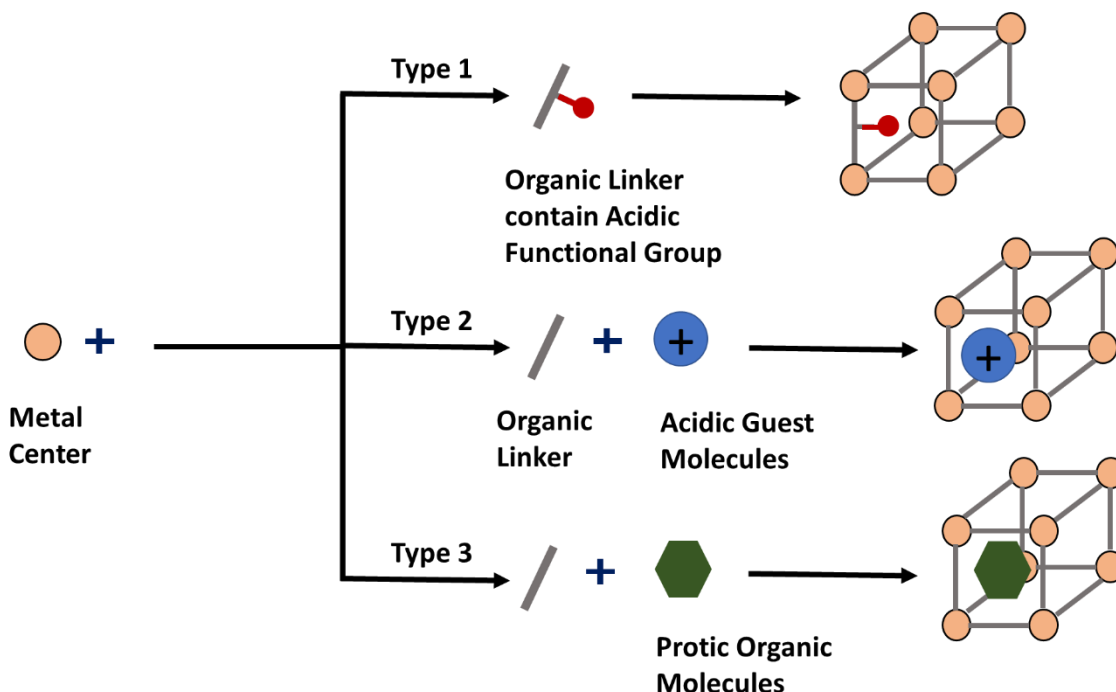


Figure 2.4: Schematic illustration of MOFs to regulate proton conductivity.

The fundamental aspect in proton conductivity is the ability of a compound to donate or accept a proton. The acid dissociation constant ( $pK_a$ )<sup>[63]</sup> describes the protonated and deprotonated forms of a compound at a given pH level and gives an indication of its equilibrium state.<sup>[64]</sup> In MOFs, the acidic functional groups play a key role in hydrophilicity and proton conductivity. Carboxylic acid (CA), phosphonic acid (PA), and sulfonic acid (SA) serve as functional groups. The  $pK_a$  values of these functional groups are as follows: CA (4.2)<sup>[65]</sup> < PA (2.0)<sup>[60]</sup> < SA (-0.7)<sup>[65]</sup>. The lowest value for SA implies that it has a high acidity and provides good proton sources. Each SA contains three oxygen atoms that can coordinate to metal ions in varying directions, thereby forming a 1D, 2D or 3D structure for a MOF. An alarming feature

of organo-sulfonates is their poor coordination with several metal ions, which makes them difficult to introduce into MOFs. Alternately, we can use it in conjunction with other functional groups, such as CA and PA, and use SA as a dangling acidic chain that participates in proton transfer. In the dangling SA chain, the three oxygen atoms can accept three protons, allowing them to form divergent hydrogen bonds to facilitate the proton transport.<sup>[66]</sup>

As part of its dissociation mechanism, PA releases one or two protons in a solution. Phosphonate-based ligands are capable of generating a wide range of metal phosphonates with diverse structural properties due to their versatility and strong coordination ability. In comparison to other types of MOFs or CPs, these MOFs have a high thermal stability. As far as water solubility is concerned, trivalent and tetravalent phosphonate MOFs are highly insoluble in water.<sup>[60]</sup>

Based on the pKa values, MOFs which contain CA-based ligands have a lower proton conductivity than MOFs containing PA- and SA-based ligands. However, CA-MOFs can be used for proton conduction applications due to their strong coordination, regular structure, and stable framework. In the framework, the oxygen atom and -OH group of carboxylate unit can form complex network of hydrogen bonds between themselves or with guest molecules. Furthermore, the uncoordinated group (-COOH) can donate protons and construct hydrogen bonding network.<sup>[62]</sup>

Practically, a MOF should possess thermal, chemical and water stability under the effect of applied conditions, such as temperature and humidity.

## 2.4 Proton Conductivity

The movement of charge in response to applied electric field is defined as electrical conductivity ( $\sigma$ ). When an external force such as potential ( $U$ ) is applied to a medium, an electric field is produced ( $\mathbf{E} = -\nabla U$ ). As a result, the current will flow, and the current density ( $\mathbf{J} = I \times A^{-1}$ ) through that medium will be equal to the total electric current ( $I$ ) flowing through the cross-section area ( $A$ ). It follows that  $\mathbf{J}$  and  $\mathbf{E}$  are directly proportional to one another, with a proportionality coefficient known as conductivity  $\sigma$  ( $\mathbf{J} = \sigma \mathbf{E}$ ). In case of constant applied potential difference, a static electric field is produced, and a charge ( $q$ ) experiences a force ( $\mathbf{F} = q \mathbf{E}$ ). Due to zero sum of forces exerted from all directions, the charge carrier begins to move in the electric field at a constant velocity ( $\mathbf{v} = \mu \mathbf{E}$ ), where  $\mu$  represents the mobility. If the number of charge particles  $n$  is moving through a unit volume, then the relation between current density and mobility is shown in equation 2.4.<sup>[67]</sup> In the above mathematical terms, the symbols in "bold" indicate that they are vector quantities.

$$\mathbf{J} = nq\mathbf{v} \quad (2.4)$$

In solid conductors, like metals and semiconductors, the electrons or holes are the charges that can move from a high potential to a low potential, and this is called electronic conductivity. In contrast, ionic conductivity refers to the movement of ions which, according to elementary science, is associated with liquid electrolyte solutions. Later, a study by Faraday showed that fluoride anions move within solid lead fluoride at high temperatures. This type of ionic conductivity in solids is useful in energy conversion devices and chemical sensors.

Conductivity of an ion is a function of charge, concentration of mobile charge, and mobility of the charge carrier. A potential difference is applied to cause the proton to move between two sites and thus generate a current.<sup>[68]</sup>

$$\sigma = nq\mu \quad (2.5)$$

Equation 2.5 states that proton conductivity can be improved by tuning the concentration and mobility of charge carriers while keeping the charge constant. It has been discussed in detail in one of the preceding sections how proton carriers can be introduced into MOFs to improve proton conductivity. Concerning to the mobility of proton from an energetic site, an adjacent energy gradient site should be available, providing an unobstructed pathway.

The most fundamental and substantial task in developing proton conducting materials is conductivity evaluation, and complex impedance spectroscopy is a well accepted basic tool to measure it. By using this method one can determine the resistance of a sample (such as single crystals or pelletized powders) over a wide frequency range.<sup>[55]</sup> Proton resistance can be measured in two different directions, known as in-plane and through-plane mode as labeled in Figure 2.5. For in-plane measurement, both electrodes make contact with the sample from the same side, while for through-plane measurement, the sample is sandwiched between two electrodes.<sup>[69]</sup> Both of these methodologies can calculate the proton conductivity from equations 2.6 and 2.7, where  $d$  is the distance or spacing between electrodes,  $t$  is the thickness of the sample,  $w$  is the width of the sample,  $A$  is the effective contact area of the electrodes, and  $R$  is the resistance of the sample.<sup>[70-73]</sup>

in-plane conductivity:

$$\sigma = \frac{d}{Rtw} \quad (2.6)$$

through-plane conductivity:

$$\sigma = \frac{t}{RA} \quad (2.7)$$

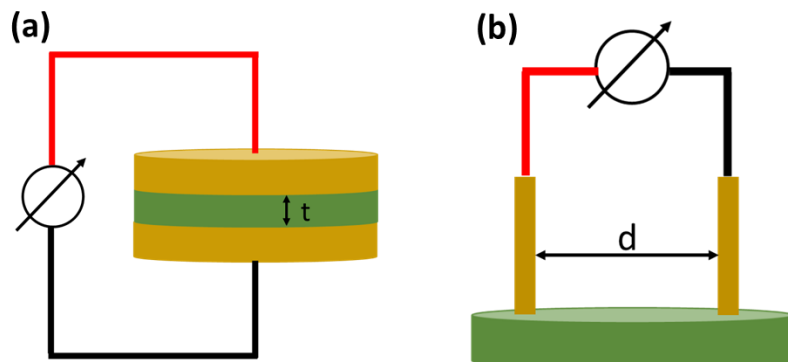


Figure 2.5: Schematic representation of impedance measurement methods a) through-plane and b) in-plane.

## 2.5 Activation Energy

Activation energy refers to the energy required for a proton to jump between two sites. In the absence of external electric fields, the proton is in its static state between equal energy sites. By applying an electric field, the energy profile is perturbed, and the proton donor sites become energetically higher than proton acceptor sites. This provides a driving force with

which a proton can travel in the direction of the electric field. This means that the jump frequency increases in the direction of the field rather than in the reverse direction.<sup>[74]</sup>

According to equations 2.8 and 2.9, the Nernst-Einstein equation relates ionic conductivity and mobility to diffusion coefficient ( $D$ ). These equations are derived using Fick's law and Boltzmann's law. In addition, the dependence of diffusion coefficient on temperature, according to the Arrhenius equation, provides another form of relation shown in equation 2.10, in which  $\sigma$  can be used to calculate the activation energy ( $E_A$ ).<sup>[6,67,68]</sup>

$$\sigma = \frac{nq^2D}{k_B T} \quad (2.8)$$

$$\frac{\mu}{q} = \frac{D}{k_B T} \quad (2.9)$$

The proton conduction mechanism can be studied based on the  $E_A$  value, which can be calculated from the Arrhenius equation shown in equation 2.10, where  $\sigma_0$  is the material-specific factor,  $k_B$  is the Boltzmann's constant, and  $T$  is the temperature of the system.

$$\sigma = \frac{\sigma_0}{k_B T} \exp\left[\frac{-E_A}{k_B T}\right] \quad (2.10)$$

A natural log is applied to both sides of equation 2.10 resulting in equation 2.11, which represents a linear equation. By plotting the experimental values of conductivities at several temperatures,  $\ln(\sigma T)$  versus temperature inverse ( $T^{-1}$ ), the Arrhenius plot is obtained. The slope ( $-E_A k_B^{-1} T^{-1}$ ) of linear regression is used to calculate  $E_A$ .

$$\ln[\sigma T] = \ln\left[\frac{\sigma_0}{k_B}\right] + \frac{1}{T} \left[\frac{-E_A}{k_B}\right] \quad (2.11)$$

In equation 2.12,  $D_0$  is Fick's law pre-exponential factor and  $\Delta S$  is the entropy of proton motion. The constant ( $D_0$ ) includes the mobile proton density, their jump frequency, path, and distance.

$$\sigma_0 = nq^2 D_0 \exp\left[\frac{\Delta S}{k_B}\right] \quad (2.12)$$

## 2.6 Proton Conduction Mechanisms

In MOFs and CPs, proton conduction may occur via one of the following two mechanisms: the Grotthu $\beta$  mechanism or the vehicle mechanism.<sup>[56,75,76]</sup> The Grotthu $\beta$  mechanism model was proposed by Theodore von Grotthu $\beta$  in 1806. He has discovered this mechanism while studying the proton transfer between water molecules. This model is characterized by high mobility, and activation energy in solid proton conducting materials between 0.1 eV and 0.4 eV,<sup>[52]</sup> while  $E_A$  values required to break the hydrogen bond in liquid water is 0.11 eV (2-3 kcal/mol).<sup>[75,77]</sup>

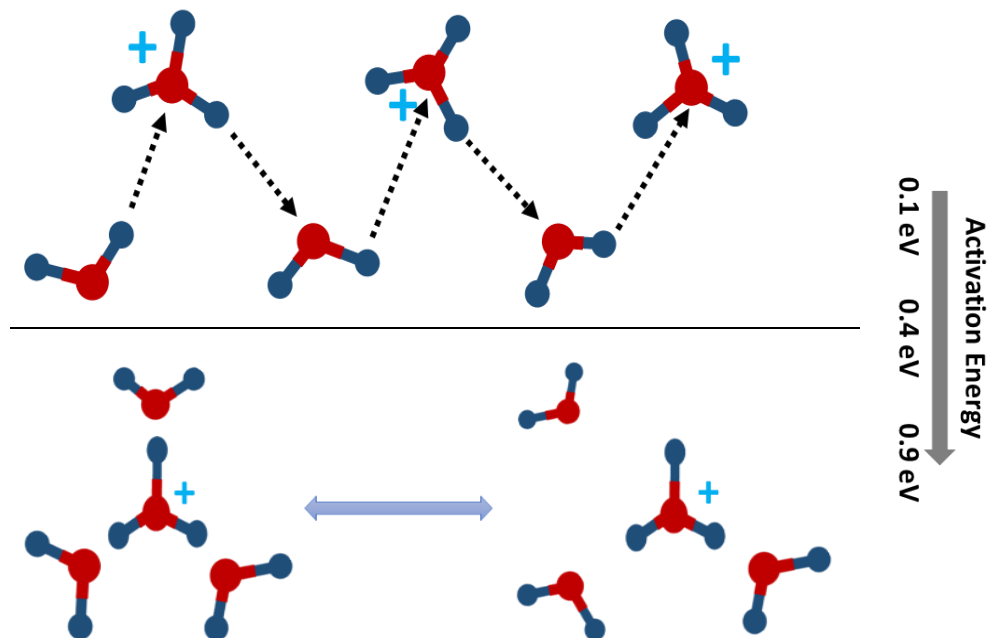


Figure 2.6: Schematic representation of the Grotthu $\beta$  Mechanism (top), in which protons transfer along hydrogen bonds, and the vehicle Mechanism (bottom), in which protons travel in solvated form, like  $\text{H}_3\text{O}^+$ .  
General color scheme: O: red, H: blue, H-Bonds: black dotted line arrow.

According to Grotthu $\beta$  mechanism, the proton transfer occurs via the on-off switch of hydrogen bonds between water molecules or other vacant adjacent sites available. It is also known as the hopping mechanism because protons jump from one available site to another available site. In contrast, Kreuer et al. proposed vehicle mechanism in 1982, which involves the diffusion of protonated species such as  $\text{H}_3\text{O}^+$ ,  $\text{NH}_4^+$ , etc. bonded to vehicles like  $\text{H}_2\text{O}$  and  $\text{NH}_3$ , for the proton conduction.<sup>[78]</sup> This mechanism is characterized by low proton mobility (due to slow diffusion process), and high  $E_A$  between 0.4 eV and 0.9 eV (caused by the migration of large ions).<sup>[52,79]</sup> A schematic diagram of both mechanisms is represented in Figure 2.6.

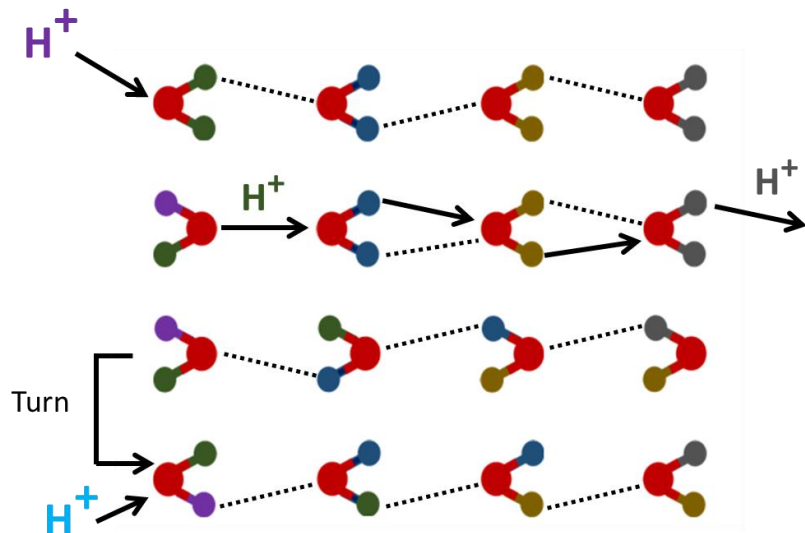


Figure 2.7: Schematic diagram of proton conduction via hydrogen bonds in bulk water. General color scheme: O: red, H: green (1<sup>st</sup> H<sub>2</sub>O molecule), H: blue (2<sup>nd</sup> H<sub>2</sub>O molecule), H: gold (3<sup>rd</sup> H<sub>2</sub>O molecule), H: gray (4<sup>th</sup> H<sub>2</sub>O molecule), H-Bonds: black dotted line.

Figure 2.7 demonstrates the basic principle of proton conduction in water molecules, described by Grotthuß. Consider a water chain that consists of four water molecules linked by hydrogen bonds. Protons can move from the first to the fourth molecule as a result of an electrochemical gradient. Once a proton reaches the oxygen atom of the first water molecule, it creates a covalent bond OH, and one of the protons that already has a covalent bond with that oxygen atom is shared with the next water molecule. In this manner, the proton follows the water wire, as can be seen in the first two rows of Figure 2.7. During this proton jumping phase, the dipole moment of the donor water molecule reverses. The total dipole moment of all the water molecules reverses as the proton leaves the fourth molecule of the chain. Figure 2.7 clearly illustrates this in the third row. In the last row, it is evident that all of the water molecules rotate back to original configuration when another proton is to be transferred in the same direction.<sup>[80]</sup>

## Chapter 3: Methodology: The Fundamentals and Analysis Approach of Impedance Spectroscopy

This chapter is divided into two sections: introduction and analysis of impedance spectra. The objective is to provide a qualitative and quantitative comprehension of impedance spectroscopy, including its fundamentals and a description of how the concerned parameters involved can be calculated.

### 3.1 Introduction

AC impedance spectroscopy (IS) is an electrochemical technique that has been employed since decades in a broad range of fields to investigate the properties of electrochemical systems, solid electrolytes, kinetics of corrosion, etc. IS is a sensitive and non-invasive in-situ technique which is a cornerstone to develop novel materials and improve their performance.<sup>[81,82]</sup> Therefore, it must be used with great caution along other methods to correlate the electrical properties with physico-chemical parameters. The system whose properties are unknown act as a “black box” and a question arises what it is. It can be interrogated by subjecting an input and measuring the output, as represented in Figure 3.1. Consider a case study where a sample is placed in a dark room. If an electrical current is measured as a response by applying light of specific wavelength, then the sample absorbs the photons and has photoactive properties and its kinetics can be further studied by modulating the light intensity. In the same manner, electric potential can be used as an input and resulting output current can be observed, where the modulation in electric potential will enable us to study charge storage and kinetics of those processes that transform the potential  $X(\omega)$  into current  $Y(\omega)$ . In such a case, the transfer function is a parameter which explains the relation between input and output and IS is a tool which is based on this concept.<sup>[83]</sup>

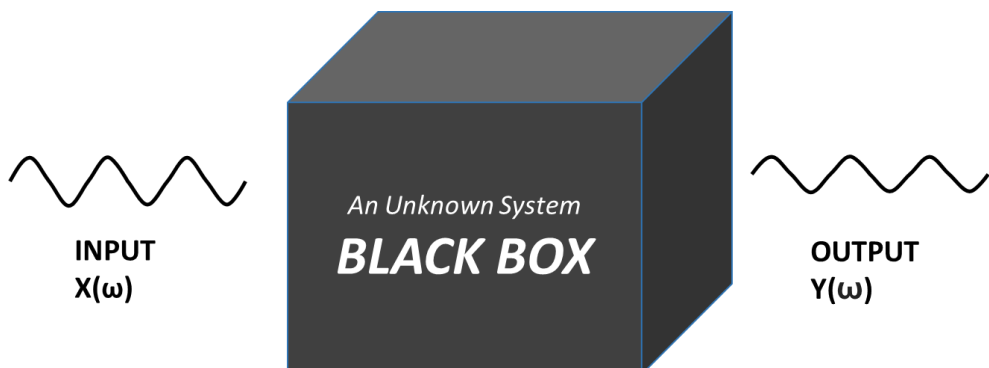


Figure 3.1: Schematic representation of black box subjected to a sinusoidal signal with frequency ( $\omega$ ).

Impedance measurements can be performed as a function of time or frequency. The physical phenomena can happen in different time and frequency domains. In an electrochemical system, diffusion is a slower process whose response is obtained in long time and it appears in low frequency domain. In contrast, charging of electrode-electrolyte interfaces is a rapid phenomenon which exhibits short time constants and high frequency behavior.<sup>[83,84]</sup>

### 3.2 Basics of Impedance

The property of an electrical circuit element which impedes the flow of current when periodically subjected to electrical perturbation is known as impedance ( $Z$ ). It is a complex number, *i.e.* it is comprised of real and imaginary parts. The real part corresponds to the resistance,  $Re(Z)$ , whereas the imaginary part associates to the reactance,  $Im(Z)$ . In response to incident alternating current (AC) frequency, resistance is a static parameter while reactance is a dynamic parameter. Whenever a capacitor or inductor is present in a circuit, reactance occurs. According to Ohm's law, at steady state the resistance ( $R$ ) of an element sourced by direct current (DC) can be calculated by equation 3.1, where  $U$  denotes the DC potential and  $I$  indicates the DC current.<sup>[85]</sup>

$$R = \frac{U}{I} \quad (3.1)$$

Conversely, the above mentioned resistance is referred to as impedance when being applied to an AC source. The Ohm's law for AC sources is expressed in equation 3.2, in which  $U(t)$  is the instantaneous potential, and  $I(t)$  is the instantaneous current. The term "instantaneous" implies that variables are dependent on time.<sup>[85]</sup>

$$Z = \frac{U(t)}{I(t)} \quad (3.2)$$

The excitation and response signals are defined by equations 3.3 and 3.4, respectively, where  $U_0$  represents the magnitude of applied voltage in volts,  $\omega$  denotes the angular frequency ( $\omega = 2\pi f$ ) in radians per second, and  $f$  designates the frequency in Herz. In a linear system,  $I(t)$  undergoes a phase-shift,  $\theta$ , as shown in Figure 3.2. Both the input potential and output current are sinusoidal at the same frequency, but are phase-shifted. Due to the fact that a resistor does not undergo a phase change, therefore,  $\theta$  is equal to zero. On the other hand, in a capacitor, the current leads the voltage by  $90^\circ$ , and in an inductor, the voltage leads the current by  $90^\circ$ .<sup>[86]</sup>

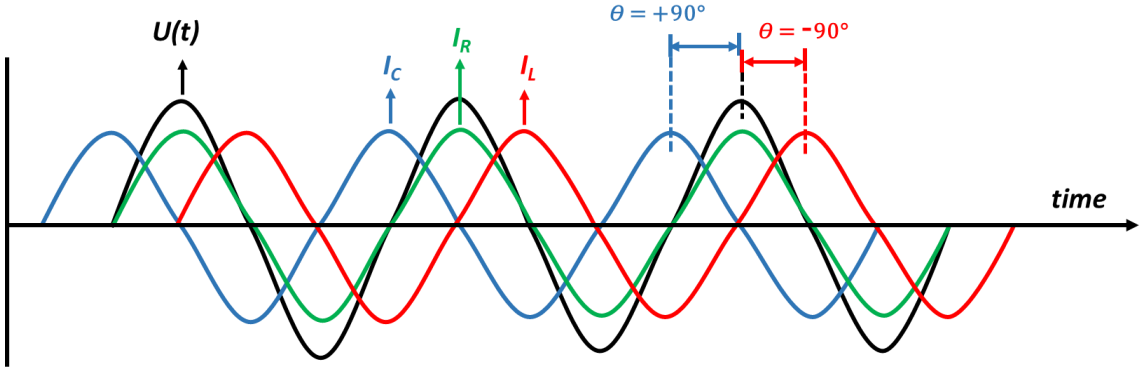


Figure 3.2: Phase diagram between response current  $I(t)$  and applied excitation potential  $U(t)$ . General color scheme of sinusoidal waves: black: applied potential, green: response current after passing through resistor ( $I_R$ ), blue: response current after passing through inductor ( $I_L$ ), red: response current after passing through capacitor ( $I_C$ ). The dotted lines display the peaks position.

$$U(t) = U_0 \sin(\omega t) \quad (3.3)$$

$$I(t) = I_0 \sin(\omega t - \theta) \quad (3.4)$$

Based on the definitions of voltage and current, impedance can be defined as:<sup>[87]</sup>

$$Z = \frac{U(t)}{I(t)} = \frac{U_0 \sin(\omega t)}{I_0 \sin(\omega t - \theta)} = Z_0 \frac{\sin(\omega t)}{\sin(\omega t - \theta)} \quad (3.5)$$

where  $Z_0$  is magnitude of impedance

Euler's law states that:<sup>[86]</sup>

$$e^{i\theta} = \cos\theta + i\sin\theta \quad (3.6)$$

where  $i = \sqrt{-1}$

$$Z = Z_0 \frac{\sin(\omega t)}{\sin(\omega t - \theta)} = Z_0 \frac{e^{i\omega t}}{e^{i(\omega t - \theta)}} = Z_0 e^{i\theta} = Z_0 [\cos\theta + i\sin\theta] \quad (3.7)$$

Therefore, impedance in the form of real and imaginary parts is:

$$Z = Z_0 \cos\theta + iZ_0 \sin\theta \quad (3.8)$$

$$Z = \operatorname{Re}(Z) + i\{\operatorname{Im}(Z)\} \quad (3.9)$$

and

$$Z_0 = [\{\operatorname{Re}(Z)\}^2 + \{\operatorname{Im}(Z)\}^2]^{\frac{1}{2}} \quad (3.10)$$

$$\theta = \tan^{-1} \frac{\operatorname{Im}(Z)}{\operatorname{Re}(Z)} \quad (3.11)$$

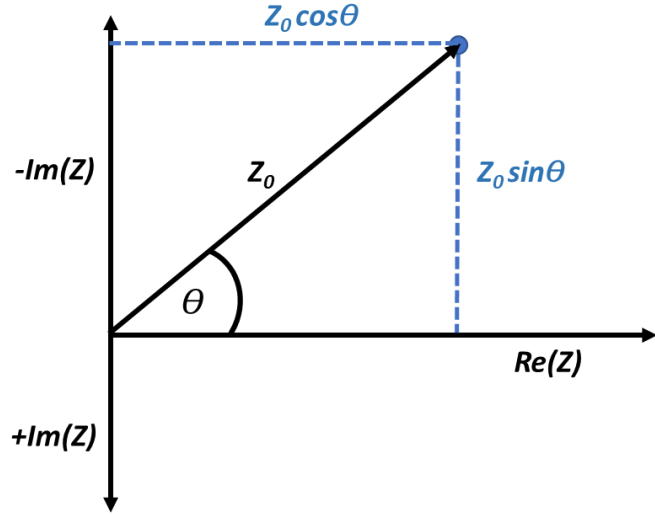


Figure 3.3: Complex plane representing a frequency dependent single data point of  $Z$ .

Impedance is a complex number that is represented in a two dimensional complex plane. In Figure 3.3, a data point of impedance is illustrated for a typical frequency of applied potential. By using equations 3.10 and 3.11, one can calculate the magnitude of impedance and phase angle for this point. A large number of experimental data points can be produced in a suitable frequency domain, because impedance varies with frequency.

### 3.3 Impedance of Ideal Circuit Elements

Electrical devices fall into two categories: real and ideal. Real devices are components of a real system that are measurable and constitute the hardware. Ideal devices are special circuit elements that have a precise and specific mathematical description. The performance of an ideal device can be simulated to approximate the real-world structure. For impedance, a model is developed based on simulated impedance to match the measured impedance of the real device. This model is referred as an equivalent circuit model (ECM) that mimics a real device and provides us an ideal electrical description. ECMs are constructed using combinations of three ideal, two-terminal circuit elements: resistor, capacitor, and inductor.<sup>[88]</sup> In an ideal resistor, current flow is opposed, while an ideal capacitor stores electrical energy, and an ideal inductor stores energy in magnetic field by opposing the change in current flow. A resistor has a real impedance independent of frequency, whereas an inductor and a capacitor have an imaginary impedance dependent on frequency.<sup>[81]</sup> The impedance of these elements is listed in Table 3.1.

Table 3.1: Ideal circuit elements with basic description and impedance.<sup>[81,89]</sup>

Element	Expression	Unit	Symbol	Impedance (Z)
Resistor	R	$\Omega$		$Z_R = R$
Capacitor	C	F		$Z_C = [i\omega C]^{-1}$
Inductor	L	H		$Z_R = i\omega L$

### 3.4 Impedance of Ideal Electrical Circuits

This research work did not observe any inductive behavior, therefore here we discuss the possible combinations of a capacitor and a resistor. R and C can be combined in series or parallel sequence and their impedance is described below.

#### 3.4.1 RC in Series Combination

In a serial order, the connection and complex plane plot are shown in Figure 3.4 (left). The observed vertical line can be obtained if charge transfer and diffusion limitations do not occur at electrode-electrolyte interface. The overall impedance of the circuit is denoted as "Z<sub>R-C</sub>" and written as:<sup>[86]</sup>

$$Z_{R-C} = R + \left[ \frac{1}{i\omega C} \right] \quad (3.12)$$

Multiply both sides by term " - [iωC]"

$$Z_{R-C} = R + \left[ \frac{1}{i\omega C} * \frac{-i\omega C}{-i\omega C} \right] \quad (3.13)$$

or

$$Z_{R-C} = R + \left[ \frac{-i\omega C}{(-i\omega C)^2} \right] \quad (3.14)$$

since  $i = \sqrt{-1}$ , then  $i^2 = -1$ , and

$$Z_{R-C} = R - i \left[ \frac{1}{\omega C} \right] \quad (3.15)$$

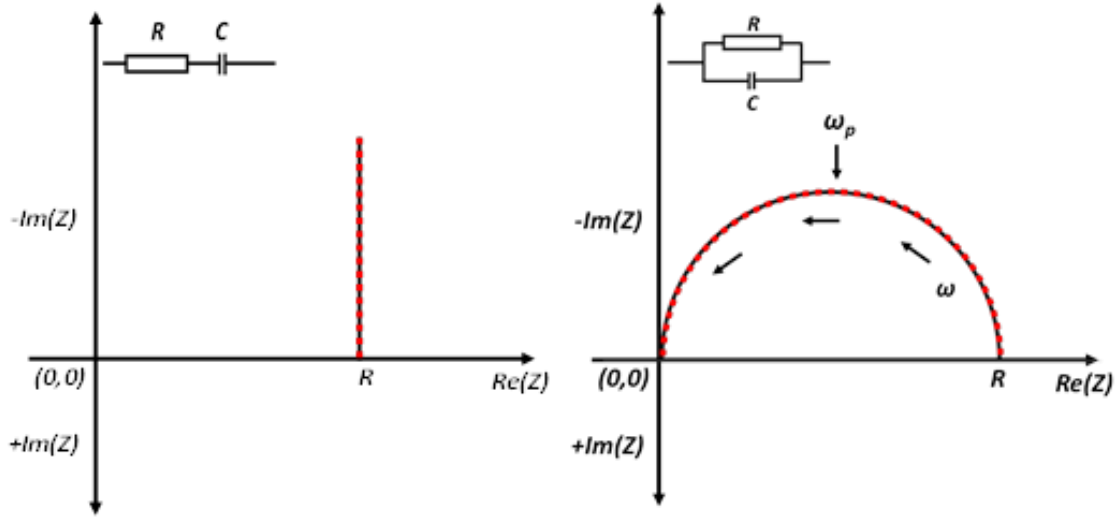


Figure 3.4: Graphical representation of RC circuits in complex plane: left) serial, right) parallel. The black solid vertical line and curve show the exemplary data points, and red dotted vertical line and curve depict fittings produced by ECM.

### 3.4.2 RC in Parallel Combination

In a parallel array, the connection and complex plane plot are shown in Figure 3.4 (right), where the diameter of the semicircle belongs to the resistance of the sample. The overall impedance is labeled by "Z<sub>R/C</sub>" and expressed as:<sup>[86]</sup>

$$\frac{1}{Z_{R/C}} = \frac{1}{R} + \frac{1}{[\frac{1}{i\omega C}]} \quad (3.16)$$

or

$$\frac{1}{Z_{R/C}} = \frac{1}{R} + i\omega C \quad (3.17)$$

or

$$Z_{R/C} = \left[ \frac{1}{R} + i\omega C \right]^{-1} \quad (3.18)$$

$$Z_{R/C} = \left[ \frac{1 + i\omega CR}{R} \right]^{-1} \quad (3.19)$$

$$Z_{R/C} = \frac{R}{1 + i\omega CR} \quad (3.20)$$

Multiply both sides by term "[1 - iωCR]"

$$Z_{R/C} = \frac{R}{1 + i\omega CR} * \frac{1 - i\omega CR}{1 - i\omega CR} \quad (3.21)$$

$$Z_{R/C} = \frac{R[1 - i\omega CR]}{[1]^2 - [i\omega CR]^2} \quad (3.22)$$

Then, we get

$$Z_{R/C} = \frac{R - i\omega CR^2}{1 + [\omega CR]^2} \quad (3.23)$$

Table 3.2: Phase angle, real and imaginary parts of impedance derived from series and parallel combination of  $R$  and  $C$ .

Circuit	$\text{Re}(Z)$	$\text{Im}(Z)$	$\tan\theta$
<b>RC</b>	$R$	$-\frac{1}{\omega C}$	$-\frac{1}{\omega RC}$
<b>R/C</b>	$\frac{R}{1 + [\omega CR]^2}$	$\frac{-\omega CR^2}{1 + [\omega CR]^2}$	$-\omega CR$

Table 3.2 displays the derived equations from both arrangements, where  $RC$  is equal to the time constant ( $\tau$ ).<sup>[86]</sup> The maxima of semicircle in Figure 3.4 labeled by  $\omega_p = 2\pi f_p$  is a peak frequency known as characteristic frequency, and at this data point,  $\frac{\delta[\text{Im}(Z)]}{\delta\omega} = 0$ . Both parameters  $\tau$  and  $\omega_p$  are inversely proportional to each other.<sup>[86]</sup> In Figure 3.5, various impedance plots and corresponding ECMS are laid out, that provide us the information about circuit topology, and parasitic values of circuit elements under ideal conditions. A process which has a distinct time constant, shows a clear semicircle in complex plane graph. Moreover, the two well-separated semicircles replicate the two distinct processes connected in series. The semicircles overlap when two different processes have the same time constant, therefore it is essential to distinguish them when modeling and fitting data.

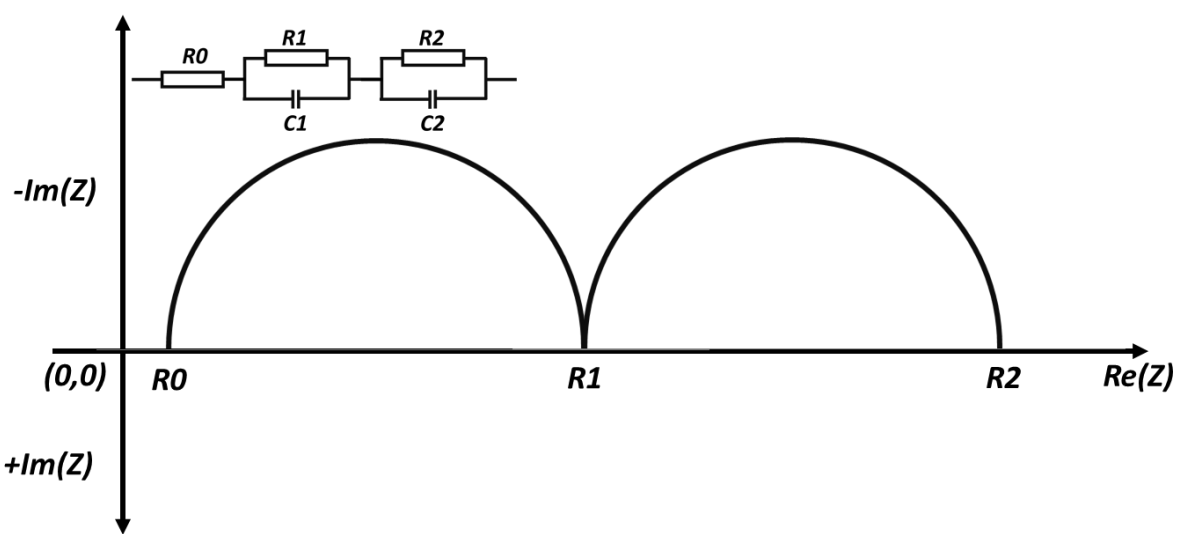
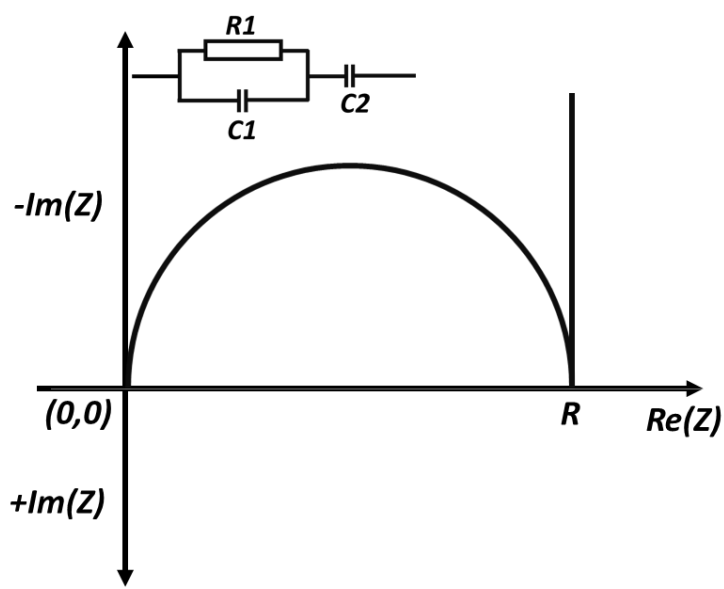
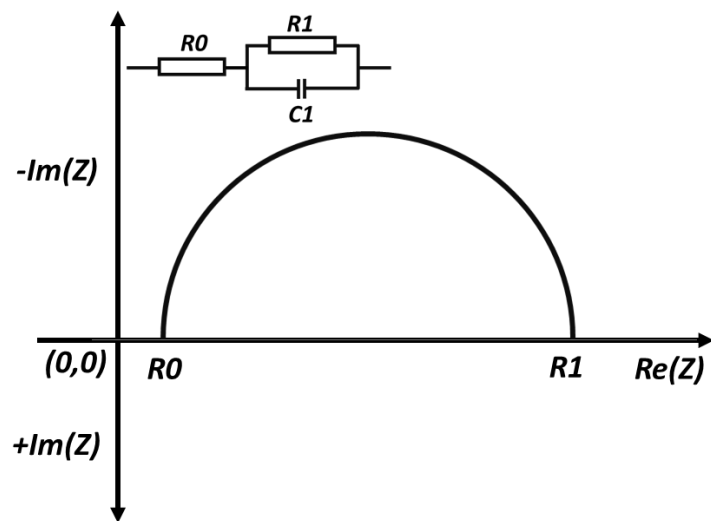


Figure 3.5: Typical  $RC$  circuit arrangements in complex planes and respective ECMS to fit the data.

### 3.5 Impedance of Real Systems

The building block of modeling the impedance data is a *RC* circuit, in which a semi-circle is characterized by a single time constant  $\tau$ , where the center of the circle lies on x-axis. However, the real physical samples usually deliver a distributed time constant due to non-uniform charge transfer, non-homogeneous reaction rate, electrode surface roughness, etc. In such a case, the center of circle is distorted, and located somewhere below the x-axis. In other words, a depressed semi-circle is obtained. A counterintuitive circuit element known as constant phase elements (*CPE*) has been identified in research on real systems and its impedance can be defined by equation 3.24:<sup>[86]</sup>

$$Z_{CPE} = \frac{1}{Q[i\omega]^n} \quad (3.24)$$

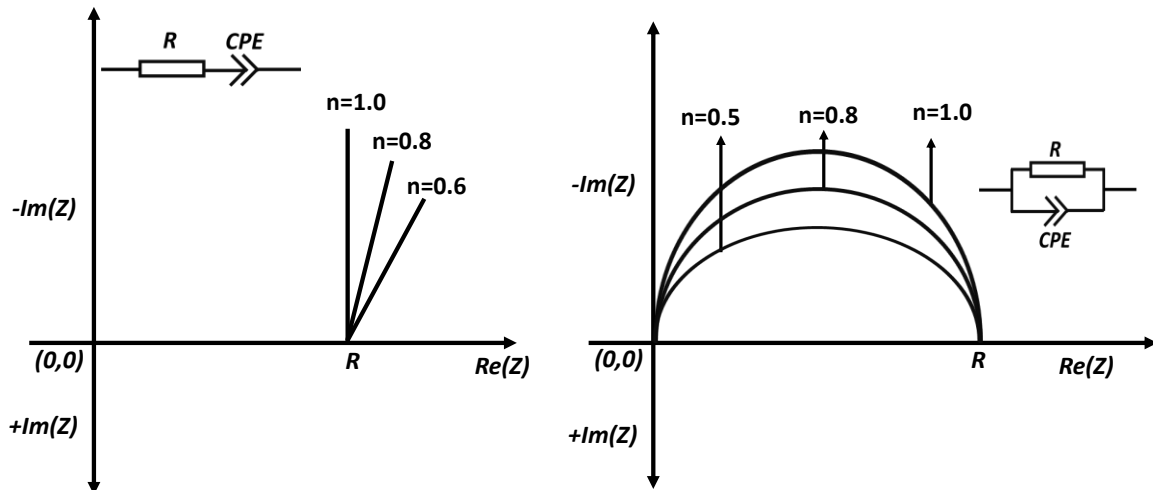


Figure 3.6: Graphical representation of change in impedance spectra with respect to exponent  $n$  in complex plane when: left)  $R$  and *CPE* are in series, right)  $R$  and *CPE* in parallel.

where  $n$  is the exponent, which describes the physical meaning of coefficient  $Q$  and characterizes the phase-shift. A depressed semicircle is obtained if  $n$  falls between the range of 0.5 to 1 (see Table 3.3 and Figure 3.6 for more information).

Table 3.3: Definition of coefficient  $Q$  based on  $n$ .<sup>[86]</sup>

$n$	$Q$
-1	(Inductance) $^{-1}$
0	(Resistance) $^{-1}$
0.5	(Warburg) $^{-1}$
1	Capacitance

Warburg element appears in the complex impedance plot at low frequencies with a linear increase in  $Z$  at  $\theta=45^\circ$ , which characterizes ionic diffusion and provides mass transfer information.<sup>[89]</sup>

### 3.6 Representation of Impedance Data

The experimental impedance data can be presented in a variety of ways. The first one is to construct a complex plane graph, which is a most widely used approach and illustrated in the previous sections. In this method, real and imaginary parts of impedance are plotted on x-axis and y-axis, respectively. This graphical representation is known as “Nyquist Plot” which is used when capacitive effects are dominating over inductive effects. Such a plot is useful to identify the conduction phenomenon happening inside the sample, which is recognized by a semicircle in the plot. In real systems, sometimes two or more semicircles are overlapped which makes the fitting process complex. Therefore, an alternative option is to analyze the impedance data by a “Bode Plot”, that exposes the dependence of impedance magnitude and phase angle on frequency.<sup>[90]</sup>

### 3.7 Relation between Impedance and Dielectric Spectroscopies

Immittance spectroscopy is a class of techniques with which the physical and chemical properties of the materials, interphases, and multijunction devices can be analyzed. Impedance, admittance, capacitance, and dielectric spectroscopies are the diagnostic tools which belong to this group. The properties of an unknown system can be determined by perturbing the system with applied potential, temperature, illumination, or environmental stress conditions.<sup>[89]</sup> The charge, electrode-electrolyte interface, and transport properties of electrolytic materials are extensively investigated using impedance spectroscopy.<sup>[91–93]</sup> In the through-plane measurement, the sample between electrodes mimics a capacitor with area  $A$  and thickness  $t$  of the sample. Impedance ( $Z$ ), permittivity ( $\epsilon$ ) and AC conductivity ( $\sigma$ ) are frequency dependent complex quantities, which are interrelated by:<sup>[93–96]</sup>

$$C_0 = \epsilon_0 \frac{A}{t} \quad (3.25)$$

$$\epsilon = Re(\epsilon) - iIm(\epsilon) \quad (3.26)$$

$$Z = Re(Z) + iIm(Z) = \frac{1}{i\omega\epsilon C_0} \quad (3.27)$$

$$Re(\epsilon) = -\frac{Im(Z)}{\omega C_0 [\{Re(Z)\}^2 + \{Im(Z)\}^2]} \quad (3.28)$$

$$Im(\epsilon) = \frac{Re(Z)}{\omega C_0 [\{Re(Z)\}^2 + \{Im(Z)\}^2]} \quad (3.29)$$

$$Re(\sigma) = \omega\epsilon_0 Im(\epsilon) \quad (3.30)$$

$$Im(\sigma) = \omega\epsilon_0 Re(\epsilon) \quad (3.31)$$

where  $C_0$  is the vacuum capacitance,  $\epsilon_0$  ( $8.85 \times 10^{-12} \text{ F/m}$ ) is the permittivity of free space.<sup>[95,97]</sup> It is apparent that permittivity is also an important factor to study along with impedance, which provides an alternative way to determine the conductivity. Thus, either equation 2.7 or equation 3.30 can be used to calculate proton conductivity.

## Chapter 4: Experimental Setup

This chapter briefly discusses the experimental setups for measuring the experimental impedance data; a more detailed description of the setups are not the focus of this study. Test stations are made up of three main components: impedance equipment, sample cell, and applied environment control.

A scheme for measuring the proton conductivity of single crystals is illustrated in Figure 4.1. In this case, humidity is controlled using a custom-built setup in which dry nitrogen is controlled by mass flow controllers (MFCs). To adjust the desired relative humidity, dry nitrogen gas was mixed with humidified nitrogen gas. Nitrogen was used here as a carrier gas. It was humidified by passing its partial stream through a deionized water reservoir. The mixing system was controlled by a LabVIEW program from National Instruments. The humidified gas was supplied to the sample cell at 50 ml/min to achieve the desired level of humidity.

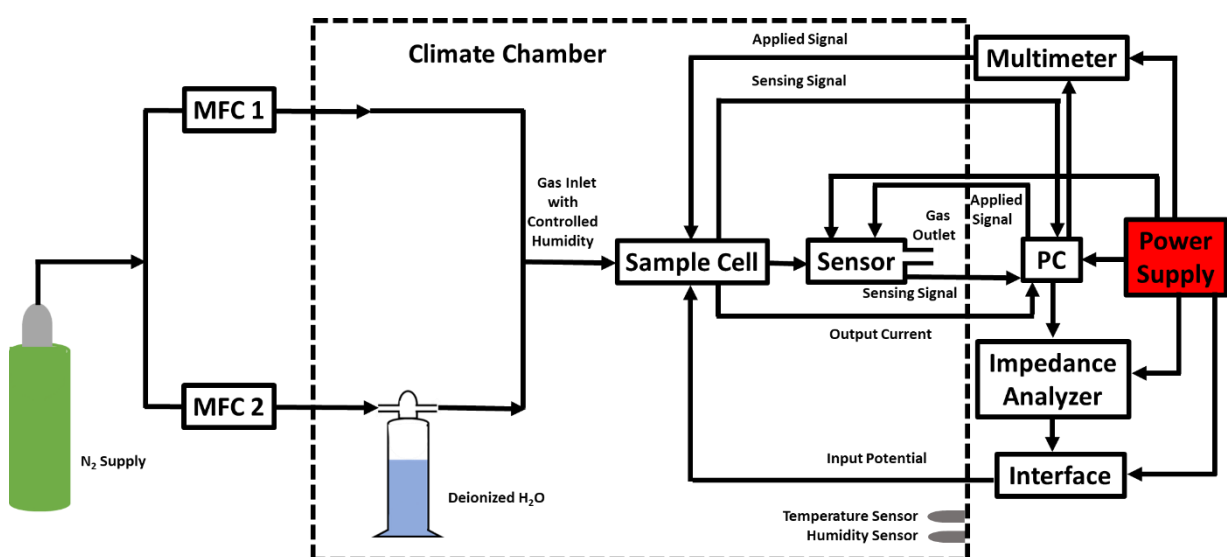


Figure 4.1: Schematic diagram of laboratory test bench for single crystal impedance measurement.

The impedance of single crystals was measured using a commercially available substrate (UST), which is 3x3 mm<sup>2</sup> in size and contains an array of interdigital electrodes (IDEs) mounted on an alumina substrate. IDEs were fabricated with approximately 20  $\mu\text{m}$  electrode width and 20  $\mu\text{m}$  finger spacing. This substrate was placed inside the Faraday cage to provide the shielding of samples from the environment. This is essential in case of sample that have high resistance which, in turn, produce very small current. In such a case, to measure the impedance at low frequency range is a

challenging part. The substrate has a  $10 \Omega$  Pt heating element that was also used to record the surface temperature during the measurement. This task was carried out using a digital multimeter (Model: 34972A from Keysight). Moreover, a card from Agilent (34902A, 16-Channel Reed Multiplexer) was integrated into the device. A scan rate of 1 scan/second/channel was used for the measurements, and the range of up to 100 ohms was defined. Finally, the heater resistance was determined by four-point measurements.

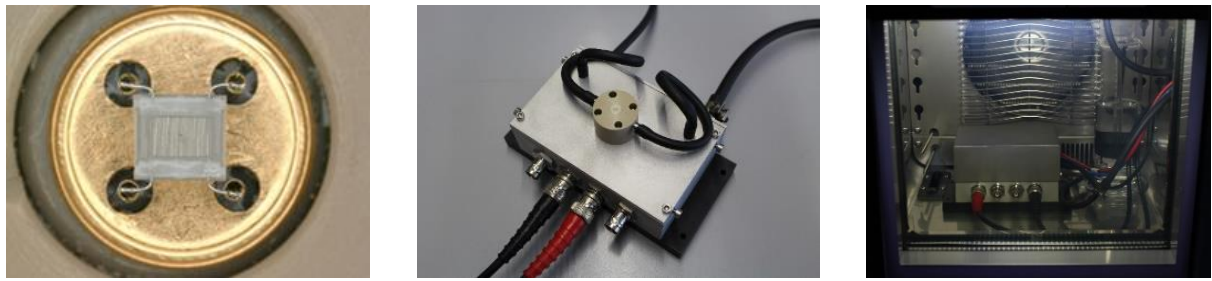


Figure 4.2: Substrate with interdigital electrodes for impedance measurements of single crystals (left); the measurement is carried out in a Faraday cage (middle) that is placed in a climate chamber with temperature and humidity control (right).

To maintain the desired temperature, the water reservoir and Faraday Cage were placed inside an ESPEC climate chamber (SH-242) as shown in Figure 4.2. As humidity was maintained by the setup described above, this chamber was not used here as a humidity chamber. As an additional measure to verify the setpoints of temperature and humidity, a sensor (SHT2x from Sensirion) was installed at the gas outlet of the cage.

Impedance analyzers were used to measure the resistance of the materials potentiostatically. For these measurements, the Solartron SI1260 impedance spectrometer with a combination of the Chelsea Dielectric Interface test interface (frequency: 10  $\mu$ Hz to 32 MHz, AC signal: 30 mV to 3 V), and the Alpha-A mainframe unit with the ZG4 extension test interface (frequency range: 3  $\mu$ Hz to 40 MHz, AC signal: 100  $\mu$ V to 3 V), were featured. Both spectrometers were operated in two-wire mode. A LabVIEW program for Solartron and WinDETA software for Alpha-A analyzer allowed to capture impedance information, data processing, and fully automatic test sequence.

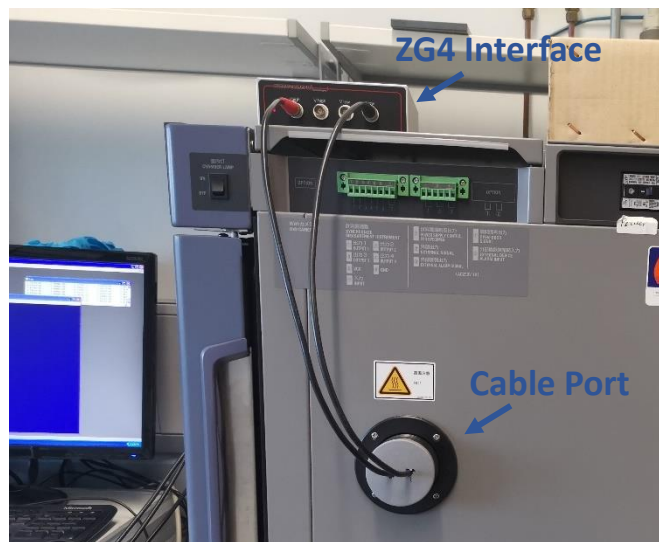
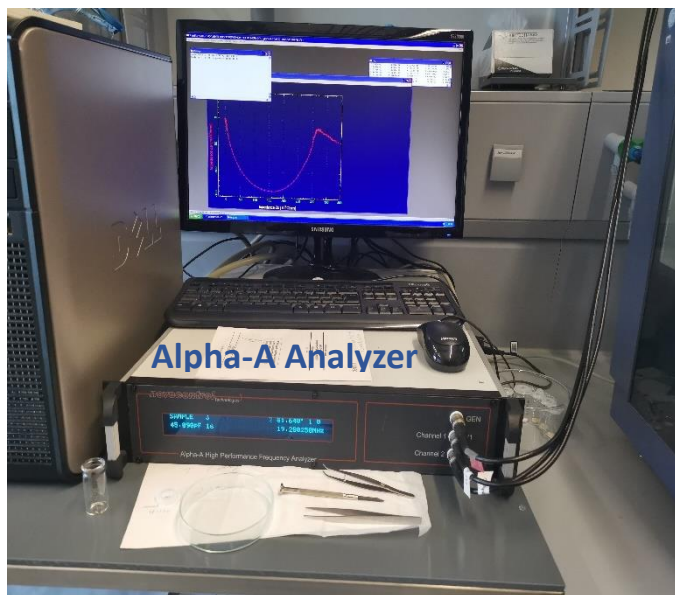


Figure 4.3: top) Solartron SI 1260 with Chelsea Interface, middle) Alpha-A Analyzer setup, and bottom) ZG4 Interface connection to cell placed inside climate chamber.

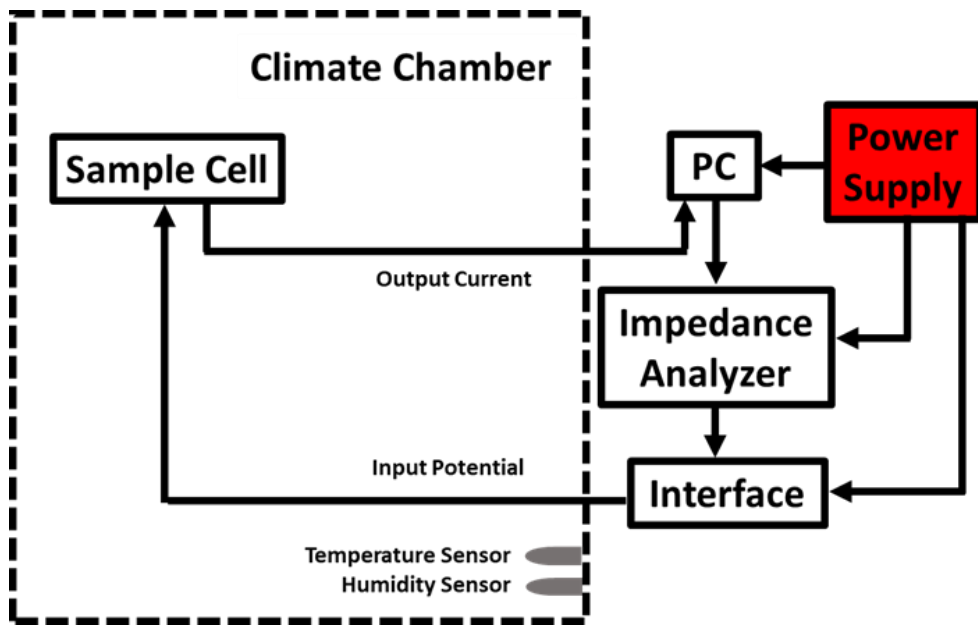


Figure 4.4: Schematic diagram of laboratory test bench for pressed pellets impedance measurement.

For the pressed pellet samples, through-plane measurements were performed with a different sample cell (BDS 1200 sample from Novocontrol). The mounting stage of cell was removed, and custom-built electrical connections were developed. The cell was then calibrated with the reference sample (100  $\Omega$  from Novocontrol), and the material was sandwiched between the two blocking gold-plated electrodes. In these measurements, both humidity and temperature were also controlled by ESPEC-242 climate chamber. Figure 4.4 exhibits the scheme of the setup, and Figure 4.5 shows the different views of sample cell.

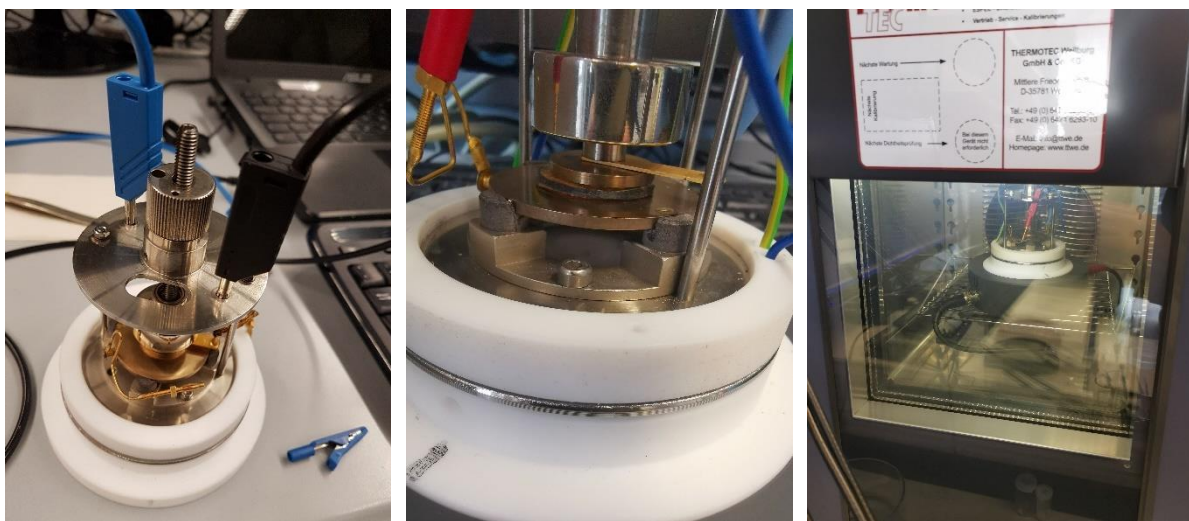


Figure 4.5: left) top-view of cell, middle) exemplary sample placed between the electrodes, and right) cell placed inside the climate chamber.

## Chapter 5: Publications

### 5.1 Proton Conduction in a Single Crystal of a Phosphonato-Sulfonate-Based Coordination Polymer: Mechanistic Insight

**Ali Javed**, Thorsten Wagner, Stephan Wöhlbrandt, Norbert Stock, Michael Tiemann

**DOI:** [10.1002/cphc.202000102](https://doi.org/10.1002/cphc.202000102)

#### 5.1.1 Outline and Outcome

This research was published as an open access article in the journal “*ChemPhysChem*” in 2020. The paper discusses the impedance spectroscopic studies of proton conductivity in a single-crystalline coordination polymer of composition  $[\text{Ba}(\text{H}_3\text{L})(\text{H}_2\text{O})]\cdot\text{H}_2\text{O}$  that consists of  $\text{Ba}^{2+}$  ions connected by organic phosphonatosulfonate linker molecules [ $\text{H}_5\text{L} = (\text{H}_2\text{O}_3\text{PCH}_2)_2\text{N}-\text{CH}_2\text{C}_6\text{H}_4\text{SO}_3\text{H}$ ]. The results were also presented at 31<sup>st</sup> German Zeolite Conference, held at TU Dresden in 2019.

This compound was synthesized and characterized by Stephan Wöhlbrandt within the framework of cooperation with Norbert Stock. He has also described the structure of a single crystal in his article “*Permanent porosity and role of sulfonate groups in coordination networks constructed from a new polyfunctional phosphonato-sulfonate linker molecule*”.<sup>[98]</sup> The single-crystal nature of the specimen used for impedance measurement was confirmed through light polarization microscope by Xia Wu from Thorsten Wagner group. The remaining tasks concerning to impedance spectroscopy were performed by the author of this thesis.

The single crystal structure analysis revealed that  $\text{Ba}^{2+}$  cation formed a mono-capped square antiprism with nine O atoms. The zigzag chain was generated by the edge sharing of  $\text{BaO}_9$ -polyhedra, which established a microporous 3D network by bridging with  $-\text{PO}_3\text{H}_2$  and  $-\text{SO}_3\text{H}$ . Within the framework, the phosphonic acid, the sulfonic acid, as well as the non-coordinated water molecules provided a platform for investigating proton conduction.<sup>[98]</sup>

The material crystallites in the form of elongated crystals. Therefore, a single plate-like crystal was placed on the top of interdigital electrodes (IDEs) array, and impedance was measured by varying the temperature, relative humidity, and, specifically, the orientation of the single crystal at applied electrode potential. Interestingly, proton conductivity tended to be

influenced by the orientation, implied anisotropic conduction channels in the crystal structure.

Moreover, low  $E_A$  ( $< 0.4$  eV) along the 1D channels indicated “proton hopping”.

## 5.1.2 Manuscript

# Proton Conduction in a Single Crystal of a Phosphonato-Sulfonate-Based Coordination Polymer: Mechanistic Insight

Ali Javed,<sup>[a]</sup> Thorsten Wagner,<sup>[a]</sup> Stephan Wöhlbrandt,<sup>[b]</sup> Norbert Stock,<sup>\*[b]</sup> and Michael Tiemann<sup>\*[a]</sup>

The proton conduction properties of a phosphonato-sulfonate-based coordination polymer are studied by impedance spectroscopy using a single crystal specimen. Two distinct conduction mechanisms are identified. Water-mediated conductance along the crystal surface occurs by mass transport, as evidenced by a high activation energy (0.54 eV). In addition, intrinsic conduction by proton 'hopping' through the interior of the crystal with

a low activation energy (0.31 eV) is observed. This latter conduction is anisotropic with respect to the crystal structure and seems to occur through a channel along the *c* axis of the orthorhombic crystal. Proton conduction is assumed to be mediated by sulfonate groups and non-coordinating water molecules that are part of the crystal structure.

## 1. Introduction

Ion-conducting materials have become one of the major topics in the science and technology of functional materials. They play a key role in fuel cells, which have become an integral part in modern and sustainable concepts of energy storage and conversion. For example, hydrogen ( $H_2$ ) fuel cells of the PEMFC type (proton-exchange membrane fuel cells) require a proton-conducting membrane as the electrolyte between anode and cathode. Perfluorosulfonic acid (PFSA) ionomers, such as Nafion<sup>TM</sup> (DuPont), are most commonly used for this purpose.<sup>[1–3]</sup> However, PFSA membranes exhibit some drawbacks. In addition to being rather expensive,<sup>[4]</sup> they require a delicate humidity control for reliable and efficient operation. They show high proton conductivity only in a hydrated state (up to 21 water molecules per sulfonic acid group<sup>[5]</sup>), which is achieved by humidification of the incoming gas streams. This entails a parasitic power loss, dilution of the gases, and the risk of 'flooding' in the system.<sup>[6]</sup> Also, operation temperatures are restricted to *ca.* 100 °C, while higher temperatures (up to 150 °C) would be beneficial for improved efficiency and less catalyst poisoning by carbon monoxide.<sup>[6]</sup>

For the reasons stated above, there is a quest for alternative proton-conducting materials with robust mechanical and thermal stability and reduced humidity dependency. For this matter,

metal-organic frameworks (MOFs) and other coordination polymers (CPs) have been identified as potential candidates.<sup>[7–11]</sup> However, humidity still turns out to be crucial for proton conduction in most materials. This raises some questions concerning the respective proton conduction mechanism in a given material. It needs to be elucidated whether water-mediated proton conduction really occurs through the crystal lattice, such as through channels that accommodate water molecules. Another, less favorable, possibility is that the conduction occurs predominantly along the outer surface of the grains, in which case the specific intrinsic properties of the material (porosity, tailored organic linkers, etc.) are more or less wasted. For polycrystalline materials (powders) the distinction between inherent proton conduction and surface conduction is difficult. However, when large enough single crystals are available, a single one of them can be used for proton conduction studies,<sup>[12–17]</sup> which minimizes the contribution of surface conduction and eliminates grain-grain boundary effects. This allows to obtain valuable information concerning proton conduction paths.

Here we present impedance studies of proton conductivity in a coordination polymer single crystal. The material consists of  $Ba^{2+}$  ions connected by organic phosphonato-sulfonate linker molecules and contains three acidic protons and two water molecules per formula unit.<sup>[18]</sup> It exhibits a moderate proton conductivity that is humidity-dependent. Its single-crystallinity makes it a suitable object of study for our purpose. The results indicate that proton conduction occurs both through the crystal lattice and along the grain surface.

## 2. Results and Discussion

The coordination polymer  $[Ba(H_3L)(H_2O)] \cdot H_2O$  was synthesized from barium chloride ( $BaCl_2 \cdot 2H_2O$ ) and (4-[[bis(phosphonomethyl) amino]methyl]benzene-sulfonic acid,  $H_3L$ ) under solvothermal reaction conditions employing a water/ethanol mixture as the solvent.<sup>[18]</sup> The linker molecule  $H_3L$  (Figure 1) was prepared

[a] A. Javed, Dr. T. Wagner, Prof. Dr. M. Tiemann  
Department of Chemistry, Paderborn University  
Warburger Str. 100, 33098 Paderborn (Germany)  
E-mail: michael.tiemann@upb.de

[b] S. Wöhlbrandt, Prof. Dr. N. Stock  
Institute of Inorganic Chemistry, University of Kiel  
24098 Kiel, Germany  
E-mail: stock@ac.uni-kiel.de

 Supporting information for this article is available on the WWW under  
<https://doi.org/10.1002/cphc.202000102>

 © 2020 The Authors. Published by Wiley-VCH Verlag GmbH & Co. KGaA. This is an open access article under the terms of the Creative Commons Attribution License, which permits use, distribution and reproduction in any medium, provided the original work is properly cited.

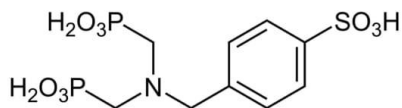


Figure 1. The linker molecule 4-((bis(phosphonomethyl)amino)methyl)benzenesulfonic acid ( $(H_2O_3PCH_2)_2N-CH_2-C_6H_4-SO_3H$ ,  $H_3L$ ).

by sulfonation and subsequent phosphonomethylation of benzylamine, as indicated in the Experimental section. Details about the syntheses are provided in reference [18]. The coordination polymer crystallizes in the orthorhombic space group  $Ama2$ , as shown in Figure 2. The asymmetric unit contains one barium ion, two oxygen atoms assigned to water, and two linker molecules at a special position. Ba is surrounded by nine oxygen atoms, resulting in a mono-capped square antiprism. The  $BaO_9$ -polyhedra are connected via edge-sharing into a chain along [001]. One linker molecule connects a total of six Ba ions by both  $(PO_3H^+)$ -groups as well as the  $(SO_3^-)$ -group, thus forming a microporous, three-dimensional network. Due to charge balance considerations, the linker is twofold deproto-

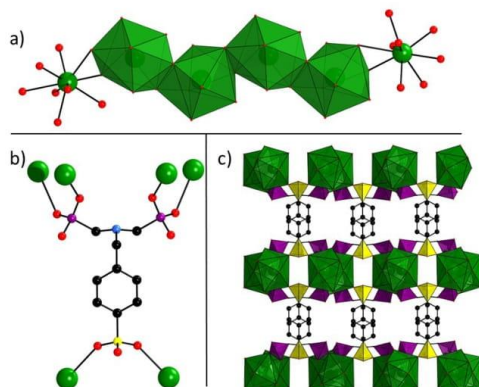


Figure 2. Detailed structural view at  $[Ba(H_3L)(H_2O)] \cdot H_2O$ . a)  $BaO_9$  polyhedra and chain along [001], b) coordination mode of the linker molecule, and c) network of  $[Ba(H_3SPP)(H_2O)] \cdot H_2O$ , view along [001] (Ba green, P magenta, S yellow, O red, C black). Hydrogen atoms omitted for clarity. Adapted from Ref. [18].

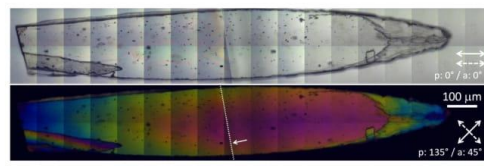


Figure 3. Transmission polarized light microscopic images (top: co-polarized, bottom: cross-polarized) of a single crystal. (Assembled from 36 single images; 36× objective lens. The small arrow indicates the edge of an underlying glass plate at the left-hand side.

nated. The three remaining acidic protons are located at the hydrogen phosphonate groups and the nitrogen atom, thus forming a zwitterion. Crystallographic and experimental details, extended structure discussion and comparison is provided in reference [18].

For the investigation of the proton conductivity, we have chosen a single crystal. Polarized light microscopic images confirm the single-crystalline nature of the specimen (Figure 3); its dimensions are  $1.50\text{ mm} \times 0.22\text{ mm}$ . The thickness of the plate-like crystal is  $ca.$   $14\text{ }\mu\text{m}$ , as determined by light microscopy. Characterization of the conductivity was done by impedance spectroscopy, which is the standard method for this purpose.<sup>[19]</sup> The crystal was placed on top of an electrode array, as shown in Figure 4 and described in the Experimental Section. The contact area between electrode array and crystal was calculated based on geometric considerations (see below), assuming a smooth and planar contact area (as verified by microscopy).

This method of contacting the crystal bears a significant advantage over commonly used methods that employ gold paste or other additives for contacting.<sup>[12–16]</sup> The crystal can be shifted and turned in its position which allows for stepless change of its orientation relative to the electrodes; hence, assessment of anisotropy in the proton conductivity is possible in a very straightforward way, as will be shown below.

Figure 5 shows a Nyquist plot (i.e. imaginary part vs. real part) of the impedance  $Z$  in the single crystal arranged in an orientation perpendicular to the electrodes (as shown in Figure 2) at a temperature of  $22^\circ\text{C}$  and relative humidity of 90%. The lower left part of the diagram corresponds to the high frequencies and exhibits a depressed semicircle-like behavior. An equivalent circuit comprising two resistors ( $R, R'$ ) and a constant-phase element (CPE) parallel to  $R$  was fitted to that high-frequency data region (between  $361.22\text{ Hz}$  and  $1\text{ MHz}$ ).  $R$  then represents the proton resistance (while  $R'$  is attributable to extrinsic resistances, such as the contact resistance). The proton conductivity  $\sigma$  is calculated by taking into account the geometric properties of the electrode array by Equation (1), where  $A$  is the contact area between the sample and the electrodes,  $n$  is the number of spacings between electrodes,  $D$  is the inter-electrode distance ( $20\text{ }\mu\text{m}$ ),  $d$  is the electrode width ( $20\text{ }\mu\text{m}$ ), and  $a$  is the width of the crystal:

$$\sigma = n \cdot [D/(R \cdot A)] = n \cdot [D/(R \cdot a \cdot d)] \quad (1)$$

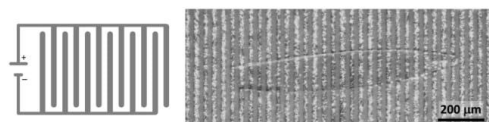


Figure 4. Schematic (left) of the electrode array used for contacting the single crystal and microscopic image (right) of the sample on top of the electrodes (the contours of the transparent crystal are visible).

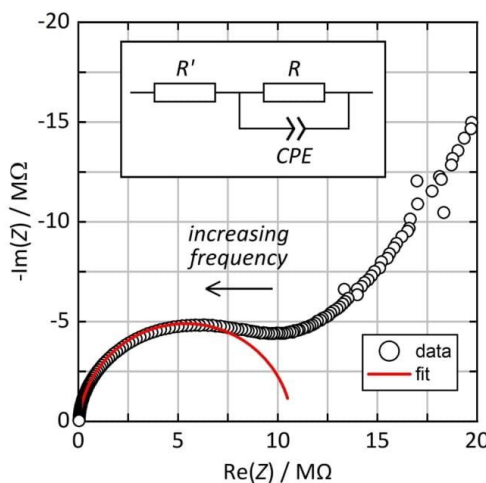


Figure 5. Nyquist plot of the impedance of the single crystal oriented perpendicular to the electrodes ( $22^{\circ}\text{C}$ , 90% r.h.) and equivalent circuit used for fitting ( $R, R'$ : resistors, CPE: constant phase element).

The proton conductivity is  $\sigma = 1.15 \cdot 10^{-4} \text{ S cm}^{-1}$  (at  $22^{\circ}\text{C}$  and 90% r.h.) for this crystal, which is a moderate value within the range typically observed in proton-conducting MOFs ( $10^{-3} \dots 10^{-5} \text{ S cm}^{-1}$ ). Measurements with three different crystals under the same conditions ( $1.14 \cdot 10^{-4} \text{ S cm}^{-1}$ ,  $1.40 \cdot 10^{-4} \text{ S cm}^{-1}$ ,  $1.15 \cdot 10^{-4} \text{ S cm}^{-1}$ ) resulted in a mean value of  $1.23 \cdot 10^{-4} \text{ S cm}^{-1}$  with a standard deviation of  $1.21 \cdot 10^{-5} \text{ S cm}^{-1}$ , which is approximately 10%. This will be considered as the approximate error to all data in the following. (Since each measurement requires an equilibration time of 12 hours, multiple measurements were avoided for reasons of time limitations, unless stated otherwise.)

We have then investigated the proton conductivity of a single crystal in variable orientation relative to the electrode structure under otherwise identical conditions (Figure 6). When the long crystal axis is in perpendicular position to the

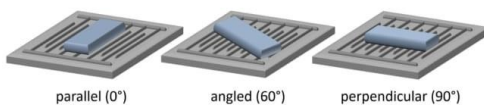


Figure 6. Schematic of a single crystal in variable orientation relative to the electrodes.

Table 1. Proton conductivities of a single crystal in variable orientation, as indicated by the schematic ( $22^{\circ}\text{C}$ , 90% r.h.).

Orientation	Proton conductivity $\sigma$ [ $\text{S cm}^{-1}$ ]
parallel ( $0^{\circ}$ )	$1.174 \cdot 10^{-5}$
angled ( $60^{\circ}$ )	$8.924 \cdot 10^{-5}$
perpendicular ( $90^{\circ}$ )	$1.142 \cdot 10^{-4}$

electrodes, the conductivity is greater than in parallel position by one order of magnitude (Table 1). This anisotropy allows two conclusions: (i) Proton conduction is an inherent property of the crystal, *i.e.* it occurs – at least partially – inside the crystal lattice, rather than exclusively at the outer surface (such as through surface-adsorbed water layers). In the latter case, the same conductivity would be expected for all orientations. (ii) Inherent proton conduction seems to occur preferentially in the direction along the long crystal axis. This second conclusion is further supported by the fact that the angular orientation ( $60^{\circ}$ ) leads to a conductivity value much closer to the perpendicular than to the parallel orientation; a conduction path along the long crystal axis can still contribute substantially in this orientation.

The data presented so far were obtained at a relative humidity of 90%. However, water turned out to have a strong impact on proton conduction. To test this impact in more detail, we have varied the relative humidity between 70% and 95% at a constant temperature of  $22^{\circ}\text{C}$ , as shown in Figure 7 (logarithmic scale). The conductivity increases approximately exponentially with the relative humidity, as frequently observed in proton-conducting coordination polymers or MOFs.<sup>[11]</sup> Figure 5 also confirms that the conductivity is generally higher for the crystal orientation perpendicular to the electrodes than for the parallel orientation.

Further, we have studied the impact of the temperature on the conduction properties. In theory, the proton conductivity  $\sigma$  is related to the temperature  $T$  by Equation (2),<sup>[9]</sup> where  $E_A$  is the activation energy,  $\sigma_0$  is a material-specific factor, and  $k_B$  is the Boltzmann constant:

$$\sigma = [\sigma_0 / (k_B T)] \cdot \exp[-E_A / (k_B T)] \quad (2)$$

Figure 8 shows the Arrhenius plots ( $\ln(T \cdot \sigma)$  vs.  $T^{-1}$ ) for a single crystal in both perpendicular and parallel orientation (at a constant relative humidity of 90%). Linear fits allow to calculate the activation energies (from the slopes,  $-E_A \cdot k_B$ ), which are clearly different for the two orientations. In the

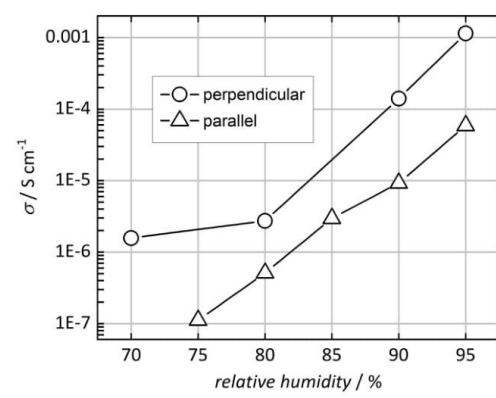
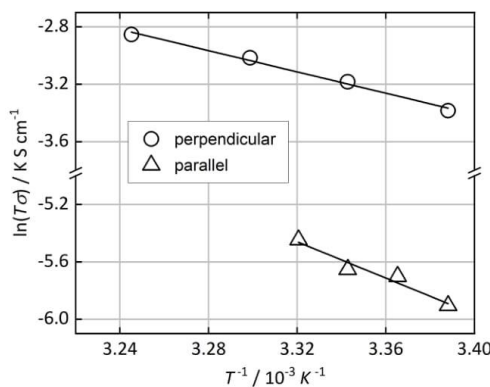


Figure 7. Proton conductivities of a single crystal in perpendicular and parallel orientation at variable relative humidity ( $22^{\circ}\text{C}$ ).



**Figure 8.** Arrhenius plots of the temperature-dependent proton conductivity of a single crystal in perpendicular and parallel orientation (r.h.=90%). The slopes of the linear fits allow to calculate the activation energies for the proton conduction (perpendicular: 0.31 eV; parallel: 0.54 eV).

perpendicular orientation a fairly low activation energy of  $E_A = 0.31$  eV is found, while for the parallel orientation the value is  $E_A = 0.54$  eV. A low value ( $< 0.4$  eV) suggests that the proton conduction occurs by a proton 'hopping' mechanism, such as between sulfonate groups and/or water molecules (similar to the Grotthuss mechanism in bulk water).<sup>[9]</sup> This is what we observe for the crystal orientation perpendicular to the electrodes. A high value ( $> 0.4$  eV), on the other hand, is typical of a mass transport-based conduction mechanism, *i.e.* by diffusion of ions, such as  $\text{H}_3\text{O}^+$ .<sup>[20]</sup> This seems to apply to the crystal orientation parallel to the electrodes.

The experimental findings can be summarized as follows: The  $[\text{Ba}(\text{H}_3\text{L})(\text{H}_2\text{O})]\cdot\text{H}_2\text{O}$  coordination polymer exhibits an altogether moderate proton conductivity. This conductivity is anisotropic with respect to the crystal axes. Along the long crystal axis (in perpendicular orientation to the electrodes) the conductivity is generally higher and marked by a low activation energy (0.31 eV) that indicates a conduction mechanism by proton 'hopping'. In the direction perpendicular to the long axis (parallel to the electrodes), the conductivity is lower and associated with a higher activation energy (0.54 eV), which suggests a conduction mechanism marked by mass transport. In both cases an increase in humidity results in higher conductivity. To explain these findings, we propose that two distinct proton conduction phenomena occur: (i) An inherent, anisotropic conductivity through the crystal (rather than its surfaces) exists in the direction of the long crystal axis. This conductivity occurs by proton 'hopping'. (ii) In addition, proton conduction also occurs at the crystal surfaces. This conductivity is isotropic and based on mass transport, apparently by surface-diffusion of adsorbed water molecules; it is observed for both orientations of the crystals, which is why the conductivity is always humidity-dependent.

To interpret the inherent (anisotropic) proton conduction mode, a closer look at the (orthorhombic) crystal structure of

the coordination polymer is useful. It exhibits two distinct types of channels in the direction along the  $c$  axis, as shown in Figure 9. The first type of channel is flanked by the phenylene groups (with the aromatic planes in perpendicular orientation to the channel axis) and by phosphonate groups. The width of this channel is too small as to accommodate water molecules; it will therefore not contribute to water-mediated proton conduction. The second type of channel is spanned by the  $\text{Ba}^{2+}$  cations and by sulfonate groups. It is reasonable to assume that proton conduction via proton 'hopping' occurs through this channel, in which case the crystallographic  $c$  axis likely corresponds to the long axis of the elongated single crystals. (Crystal structure determination revealed that the two axes that run parallel to the large faces of the plate-like crystals, are the  $a$  and  $c$  axes; however, they cannot be unambiguously distinguished here.) The channel contains a non-coordinating water molecule that is quite strongly localized, which is evidenced by its small anisotropic displacement parameters. This localization is caused by H bonds to the adjacent amino group N (N...O distance: 2.74 Å) and phosphonate groups (O...OP: 2.95 Å and 2.97 Å). This water molecule and the sulfonate groups may contribute to proton 'hopping' along the channel.

### 3. Conclusions

In summary, we have identified two distinct proton conduction mechanisms in the  $[\text{Ba}(\text{H}_3\text{L})(\text{H}_2\text{O})]\cdot\text{H}_2\text{O}$  ( $\text{H}_3\text{L}=\text{H}_2\text{O}_3\text{PCH}_2)_2\text{N}-\text{CH}_2-\text{C}_6\text{H}_4-\text{SO}_3\text{H}$ ) coordination polymer by measuring the impedance at variable temperature, relative humidity and crystal orientation. One proton conduction mode occurs at the crystal surface and is apparently dominated by

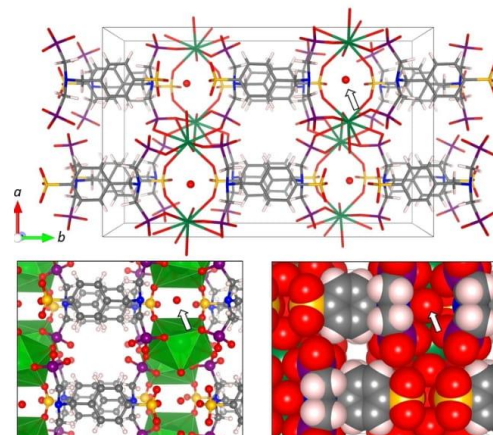


**Figure 9.** View along the  $c$  axis of the crystal structure (Ba green, P magenta, S yellow, O red, C grey, H white). Two types of channels in  $c$  direction are apparent especially in the stick (top) and ball-and-stick representation (bottom left). The arrow indicates the oxygen atom of the non-coordinating water molecule. The space-filling representation (bottom right) shows the small diameters of the channels.

mass transport in water adsorbate layers. The other mode is governed by a proton 'hopping' mechanism that takes place though the interior of the crystal; it is anisotropic with respect to the crystal structure and likely occurs through a sulfonate-lined and water-containing channel along the *c* axis of the crystal.

## Experimental Section

The linker molecule H<sub>5</sub>L was prepared as described in reference [18]. In short, benzylamine was para-sulfonated by reaction with concentrated sulfuric acid. Phosphonomethylation of the amino group was achieved with phosphonic acid and formaldehyde in half-concentrated hydrochloric acid (*c* = 5.2 mol L<sup>-1</sup>). For the synthesis of the coordination polymer [Ba(H<sub>5</sub>L)(H<sub>2</sub>O)]·H<sub>2</sub>O, the linker (6 mg, 16 µmol) was introduced into a 250 µl autoclave as a solid. Subsequently, 100 µl EtOH, 75 µl deionized water and 25 µl of a 1.28 mol/l solution of BaCl<sub>2</sub>·2H<sub>2</sub>O in deionized water were added in the given order. The reactor was closed and heated within 6 h to the reaction temperature of 150 °C. After 24 h the reactor was slowly cooled down to room temperature within 12 h. The crystals were collected via filtration and dried at ambient conditions. (Elemental analysis (%) – calculated: C 19.70, H 3.49, N 2.55, S 5.85; found: C 20.07, H 3.04, N 2.44, S 5.71.<sup>[18]</sup>)

Impedance spectra were measured by using a Solartron SI 1260 frequency response analyzer with a Chelsea 1296 Dielectric Interface. Data were recorded in the frequency range 10 Hz – 1 MHz with an input voltage amplitude of 0.1 V.<sup>[17]</sup> An alumina substrate with a 3 mm×3 mm interdigitated Pt electrode array and an electrode width and spacing of 20 µm each (UST GmbH, Germany) was used for contacting the sample. A single crystal was placed on top of the electrode array and shifted in position with the tip of a needle under a microscope. The device was placed inside a custom-built Faraday cage to shield the sample and improve the signal-to-noise-ratio. The whole setup was arranged in an Espec SH-242 climate chamber for temperature control. A constant gas stream (50 mL/min<sup>-1</sup>) with defined humidity was achieved by using a custom-built gas mixing equipment based on mass flow controllers. A dry N<sub>2</sub> stream (50 mL/min) was humidified by flowing through a washing bottle containing deionized water. Temperature and humidity of the gas stream were verified at the outlet of the cage by a Sensirion SHT2x sensor. The system was allowed to equilibrate for 12 hours after each change in temperature and/or humidity. The temperature of the substrate was further recorded by measuring the resistance of the Pt10 heater integrated in the alumina substrate, using an Agilent 34972 A digital multimeter. Impedance data were fitted by using ZView software. Crystal structure visualization in Figure 9 was made with VESTA software.<sup>[21]</sup>

## Acknowledgements

This work was funded by Deutsche Forschungsgemeinschaft (DFG, priority program SPP 1928).

**Keywords:** coordination polymer · fuel cell · impedance spectroscopy · proton conduction · single crystal

- [1] C. H. Park, C. H. Lee, M. D. Guiver, Y. M. Lee, *Prog. Polym. Sci.* **2011**, *36*, 1443–1498.
- [2] H. Zhang, P. K. Shen, *Chem. Soc. Rev.* **2012**, *41*, 2382–2394.
- [3] L. Zhang, S. R. Chae, Z. Hendren, J. S. Park, M. R. Wiesner, *Chem. Eng. J.* **2012**, *204–206*, 87–97.
- [4] R. S. L. Yee, R. A. Rozendal, K. Zhang, B. P. Ladewig, *Chem. Eng. Res. Des.* **2012**, *90*, 950–959.
- [5] T. A. Zawodzinski, C. Derouin, S. Radzinski, R. J. Sherman, V. T. Smith, T. E. Springer, S. Gottesfeld, *J. Electrochem. Soc.* **1993**, *140*, 1041–1047.
- [6] S. J. Hamrock, M. A. Yandrasits, *J. Macromol. Sci. Polym. Rev.* **2006**, *46*, 219–244.
- [7] T. Yamada, K. Otsubo, R. Makiura, H. Kitagawa, *Chem. Soc. Rev.* **2013**, *42*, 6655–6669.
- [8] M. Yoon, K. Suh, S. Natarajan, K. Kim, *Angew. Chem. Int. Ed.* **2013**, *52*, 2688–2700.
- [9] P. Ramaswamy, N. E. Wong, G. K. H. Shimizu, *Chem. Soc. Rev.* **2014**, *43*, 5913–5932.
- [10] S. Tominaka, A. K. Cheetham, *RSC Adv.* **2014**, *4*, 54382–54387.
- [11] A.-L. Li, Q. Gao, J. Xu, X.-H. Bu, *Coord. Chem. Rev.* **2017**, *344*, 54–82.
- [12] S. Tominaka, S. Henke, A. K. Cheetham, *CrystEngComm* **2013**, *15*, 9400–9407.
- [13] M. Yoon, K. Suh, H. Kim, Y. Kim, N. Selvapalam, K. Kim, *Angew. Chem. Int. Ed.* **2011**, *50*, 7870–7873.
- [14] D. Umeyama, S. Horike, M. Inukai, T. Itakura, S. Kitagawa, *J. Am. Chem. Soc.* **2012**, *134*, 12780–12785.
- [15] L. Qin, Y. Z. Yu, P. Q. Liao, W. Xue, Z. Zheng, X. M. Chen, Y. Z. Zheng, *Adv. Mater.* **2016**, *28*, 10772–10779.
- [16] R. Li, S. H. Wang, X. X. Chen, J. Lu, Z. H. Fu, Y. Li, G. Xu, F. K. Zheng, G. C. Guo, *Chem. Mater.* **2017**, *29*, 2321–2331.
- [17] H. Bunzen, A. Javed, D. Klawinski, A. Lamp, M. Grzywa, A. Kalyta-Mewes, M. Tiemann, H.-A. Krug von Nidda, T. Wagner, D. Volkmer, *ACS Appl. Nano Mater.* **2019**, *2*, 291–298.
- [18] S. Wöhlbrandt, A. Igleska, E. S. Grape, S. Øien-Ødegaard, A. K. Inge, N. Stock, *Dalton Trans.* **2020**, DOI: 10.1039/C9DT04571F.
- [19] S. M. Rezaei Niya, M. Hoofar, *J. Power Sources* **2013**, *240*, 281–293.
- [20] K. D. Kreuer, A. Rabenau, W. Weppner, *Angew. Chem. Int. Ed.* **1982**, *21*, 208–209.
- [21] K. Momma, F. Izumi, *J. Appl. Crystallogr.* **2011**, *44*, 1272–1276.

Manuscript received: February 9, 2020

Accepted manuscript online: February 11, 2020

Version of record online: February 24, 2020

**Proton Conduction in a Single Crystal of a Phosphonato-Sulfonate-Based Coordination Polymer: Mechanistic Insight**

Ali Javed, Thorsten Wagner, Stephan Wöhlbrandt, Norbert Stock,\* and Michael Tiemann\*<sup>©</sup>  
2020 The Authors. Published by Wiley-VCH Verlag GmbH & Co. KGaA. This is an open access article under the terms of the Creative Commons Attribution License, which permits use, distribution and reproduction in any medium, provided the original work is properly cited.

## Supporting Information

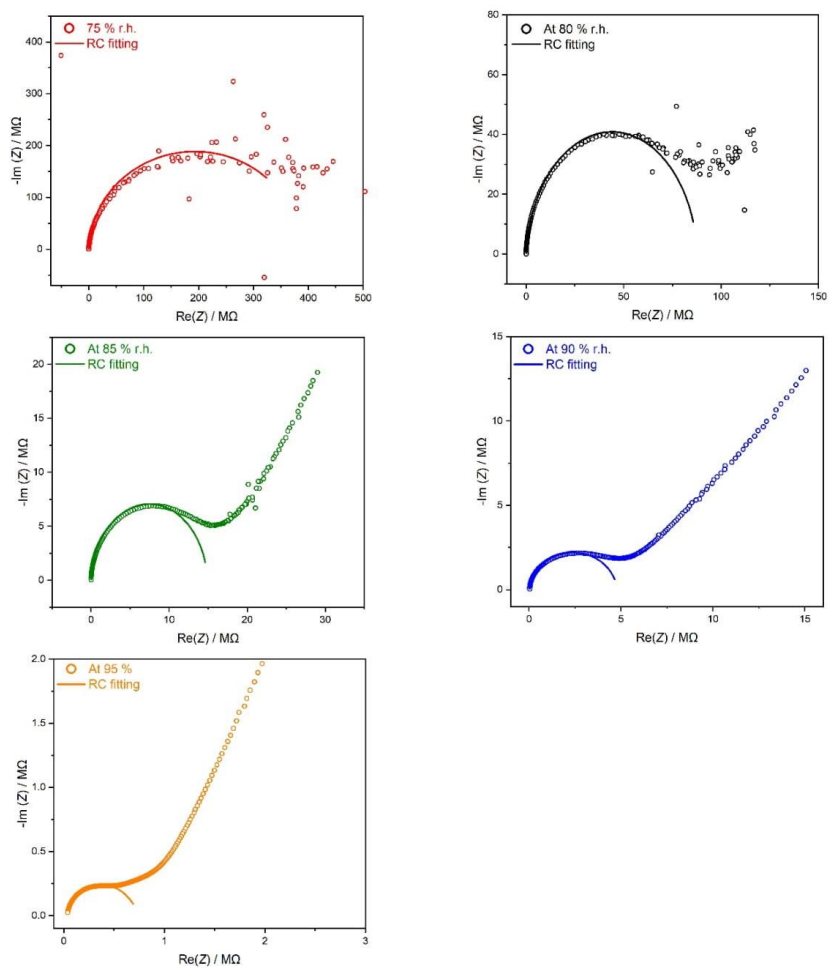


**Fig. S1.** Nyquist plots of single crystal oriented in parallel direction relative to interdigital electrodes at several setpoints of relative humidity (temperature 22 °C).

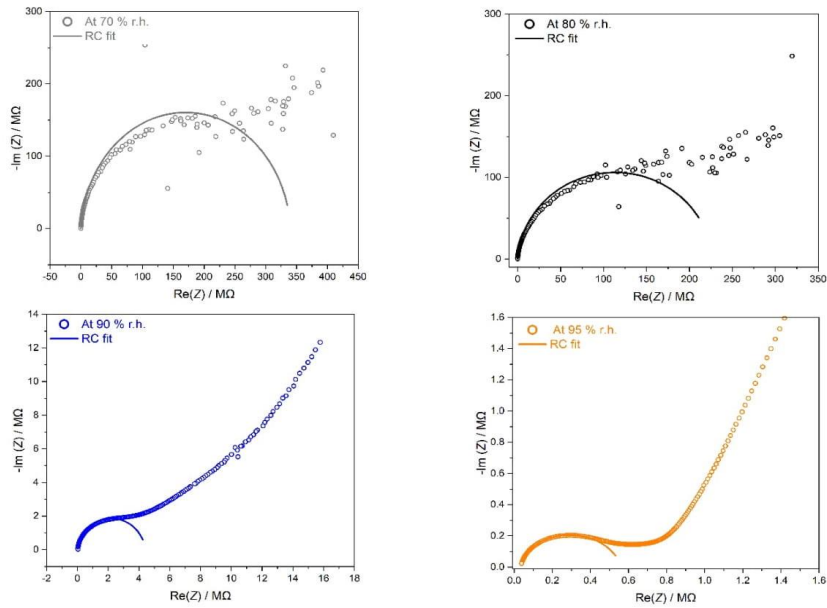


**Figure S2.** Nyquist plots of single crystal oriented in perpendicular direction relative to interdigital electrodes at various setpoints of relative humidity (temperature 22 °C).

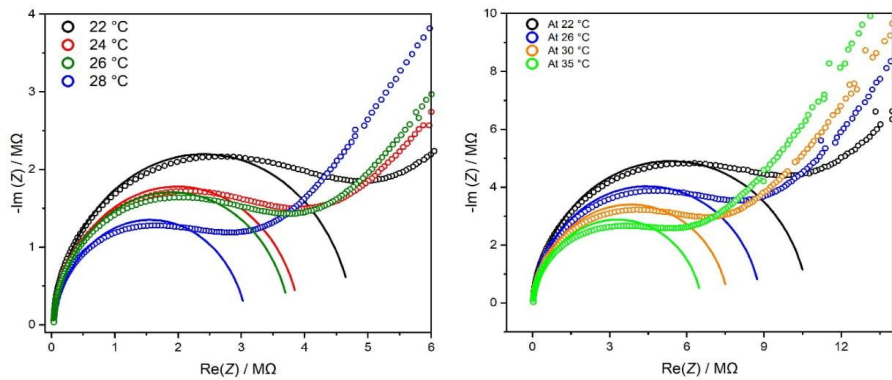


**Figure S3.** Nyquist plots of single crystal oriented in parallel (left) and perpendicular (right) direction relative to interdigital electrodes at variable temperature (relative humidity 90%).

### 5.1.3 Published Data Details

#### 5.1.3.1 Fittings Parameters and Proton Conductivity

Table 5.1.1. Summary of fittings produced using the equivalent circuit model for Ba-CP, and the calculated proton conductivities at distinct setpoints of relative humidity and temperature, and in particular at different orientations of crystals relative to IDE.

sample name	proton current direction	T [°C]	rh [%]	chi-sqr.	R' [Ω]	n	Q	R [Ω]	σ [S/cm]
Ba_1	≠	22	90	0.032	27023	0.91	1.22E-11	7.09E6	1.17E-5
	//	22	90	0.038	24823	0.89	1.54E-11	6.00E6	8.92E-5
	=	22	90	0.041	23979	0.88	1.69E-11	5.38E6	1.14E-4
Ba_2	=	22	70	0.084	32260	0.96	5.11E-12	3.44E8	1.56E-6
	=	22	80	0.057	31849	0.95	5.69E-12	2.26E8	2.73E-6
	=	22	90	0.037	23851	0.88	1.71E-11	4.41E6	1.40E-4
Ba_3	=	22	95	0.009	21136	0.82	5.04E-11	5.42E5	1.14E-3
	=	22	90	0.028	32564	0.94	7.04E-12	1.06E7	1.15E-4
	=	26	90	0.031	32027	0.94	7.56E-12	8.85E6	1.38E-4
Ba_4	=	30	90	0.035	30248	0.92	8.74E-12	7.59E6	1.61E-4
	=	35	90	0.043	28085	0.91	1.04E-11	6.56E6	1.87E-4
	≠	22	75	0.077	34008	0.97	4.45E-12	3.93E8	1.11E-7
Ba_4	≠	22	80	0.032	33679	0.97	4.69E-12	8.62E7	5.09E-7
	≠	22	85	0.022	33194	0.96	5.22E-12	1.48E7	2.95E-6
	≠	22	90	0.020	31890	0.95	6.81E-12	4.75E6	9.23E-6
	≠	22	95	0.020	27000	0.73	1.83E-10	7.48E5	5.87E-5
	≠	24	90	0.021	30690	0.94	7.76E-12	3.90E6	1.12E-5
Ba_4	≠	26	90	0.023	30507	0.93	8.06E-12	3.75E6	1.17E-5
	≠	28	90	0.027	27914	0.91	1.07E-11	3.06E6	1.43E-5

where, “=”: along c axis; “≠”: along orthogonal; “//”: along angular orientation (here 60°).

The parameters  $n$  and  $Q$  were generated using constant phase element CPE instead of using capacitor  $C$ . In software Z-View,  $n$  and  $Q$  are denoted by  $P$  and  $T$ , respectively.

## 5.2 Humidity-Mediated Anisotropic Proton Conductivity through the 1D Channels of Co-MOF-74

**Ali Javed**, Ina Strauss, Hana Bunzen, Jürgen Caro, Michael Tiemann

**DOI:** [10.3390/nano10071263](https://doi.org/10.3390/nano10071263)

### 5.2.1 Outline and Outcome

In 2020, this research was released as an open access publication in the journal "Nanomaterials". The article deals with proton conductivity in a single crystalline MOF known as Co-MOF-74. The compound is composed of Co(II) ions that are connected by 2,5-dioxido-1,4-benzenedicarboxylate linkers.<sup>[99]</sup> The findings were also presented at 32<sup>nd</sup> German Zeolite Conference, held online in 2021.

Dietzel et al. invented Co-MOF-74 in 2005,<sup>[99]</sup> and the material is also termed as CPO-27-Co. This compound was synthesized by Ina Strauss within collaboration with Jürgen Caro for this study. She employed characterization techniques such as XRD, SEM, IR spectra, and Raman spectrum to evaluate its structure and morphology. Hana Bunzen verified the hydrothermal stability up to 60 °C and 93 % relative humidity. The author of this thesis conducted the rest activities relating to impedance spectroscopy.

The crystal structure characterizes 3D network having honeycomb topology which is comprised of linear 1D micropores (1.1 nm). The micropores have a hexagonal cross-section and run parallel to the c-axis. Six oxygen atoms are coordinated to the Co(II) ion; five are coupled to the linker, and the sixth is exposed to the pore interior, where it is coordinated by the water molecule.<sup>[99]</sup> This readily accessible coordinating site gave us the opportunity to examine its proton conductivity.

Here, the crystals were smaller in size than those in Ba-CP. As a result, dealing with individual crystals and building electrical contact proved to be the most challenging. On the surface of the IDE array, a rod-like crystal was placed, in a Faraday cage positioned in a climate chamber, with humidity control by a custom-built gas mixing equipment using mass-flow controllers. The impedance was measured by varying the orientation of the crystal and relative humidity, as well as its temperature. As expected, high proton conductivity was observed at high value of humidity and along the c-axis. Moreover,  $E_A$  (< 0.4 eV) along c-axis suggested a proton conduction mechanism that is based on "proton hopping" in this case.

## 5.2.2 Manuscript



Article

# Humidity-Mediated Anisotropic Proton Conductivity through the 1D Channels of Co-MOF-74

Ali Javed <sup>1,\*</sup>, Ina Strauss <sup>2,\*</sup>, Hana Bunzen <sup>3</sup>, Jürgen Caro <sup>2</sup> and Michael Tiemann <sup>1</sup>

<sup>1</sup> Department of Chemistry, Paderborn University, 33098 Paderborn, Germany; michael.tiemann@upb.de

<sup>2</sup> Institute of Physical Chemistry and Electrochemistry, Leibniz University Hannover, 30167 Hannover, Germany; juergen.caro@pci.uni-hannover.de

<sup>3</sup> Institute of Physics, University of Augsburg, 86159 Augsburg, Germany; hana.bunzen@physik.uni-augsburg.de

\* Correspondence: ali.javed@uni-paderborn.de (A.J.); ina.strauss@pci.uni-hannover.de (I.S.)

Received: 19 May 2020; Accepted: 21 June 2020; Published: 28 June 2020



**Abstract:** Large Co-MOF-74 crystals of a few hundred micrometers were prepared by solvothermal synthesis, and their structure and morphology were characterized by scanning electron microscopy (SEM), IR, and Raman spectroscopy. The hydrothermal stability of the material up to 60 °C at 93% relative humidity was verified by temperature-dependent XRD. Proton conductivity was studied by impedance spectroscopy, using a single crystal. By varying the relative humidity (70–95%), temperature (21–60 °C), and orientation of the crystal relative to the electrical potential, it was found that proton conduction occurs predominantly through the linear, unidirectional (1D) micropore channels of Co-MOF-74, and that water molecules inside the channels are responsible for the proton mobility by a Grotthuss-type mechanism.

**Keywords:** metal-organic framework; Co-MOF-74; single crystal; impedance spectroscopy; proton conductivity; anisotropy; fuel cell

## 1. Introduction

The predicted increase of the world's energy consumption until 2050 is expected to be almost 50%, due to a higher industrial output, e.g., in the food or metal production sector, which comes with economic growth and an increasing world population [1]. Therefore, there is a rising demand for more efficient and sustainable energy conversion approaches. In this context, fuel cells, which allow the direct conversion of chemical energy into electrical energy, have been studied within the last few decades [2–8]. The most frequent type of fuel cells is the proton-exchange membrane fuel cell (PEMFC), in which protons are transported from the anode to the cathode through a proton-permeable membrane. The latter is usually made of Nafion, a sulfonated fluoropolymer, or of ionic polymers, which all suffer from high cost and only moderately efficient performance [9,10]. A promising approach to improve fuel cells is the incorporation of proton-conducting crystalline porous materials, such as metal-organic frameworks (MOFs) or coordination polymers, to replace amorphous polymers [11–15]. MOFs are hybrid inorganic–organic compounds, which have been vastly explored for more than two decades. Due to their modular design at the molecular level, a large number of MOFs (close to 70,000 already in 2017 [16]) exist nowadays; they can be further tailored by post-synthetic modification [17]. Their structural characteristics, such as high porosity, large specific surface area, controllable pore size, and well-defined channel systems, open doors to many potential fields of application [18–22].

Co-MOF-74, also known as CPO-27-Co, consist of Co(II) ions that are connected by 2,5-dioxido-1,4-benzenedicarboxylate linkers (Co<sub>2</sub>(dobdc)) [23,24]. The crystal structure (trigonal space group 148, *R*-3) is marked by linear micropores (1.1 nm) with a hexagonal cross section that

runs parallel to the  $c$  axis of the crystals, as verified by sorption uptake studies with in-situ IR microscopy detection [25] (see Figure 1). The Co(II) ion is penta-coordinated by the linkers, and its sixth coordination site is exposed to the interior of the pore channels, usually coordinated by a water molecule. These structural features make Co-MOF-74 a highly interesting system with respect to host–guest interaction, e.g., for catalysis [26], gas adsorption [27,28], or gas sensing [29]. Moreover, water-mediated proton conduction is possible through the channels [30]. Here, we present a fundamental study on the proton conductivity of Co-MOF-74 for potential future utilization in proton-exchange fuel cell membranes. By applying impedance spectroscopy to a single crystal specimen, we investigate the anisotropy of proton conductance, as well as the impact of relative humidity.

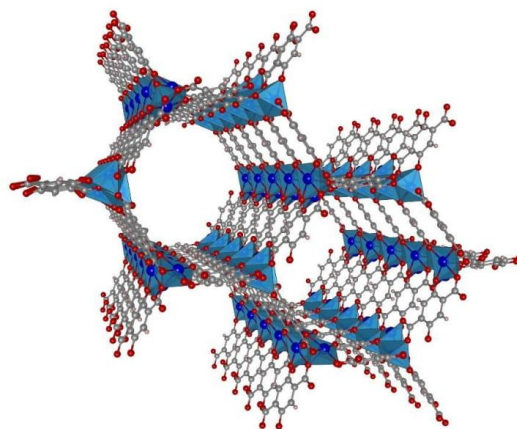


**Figure 1.** Crystal structure representation of Co-MOF-74 (Co—blue, C—grey, O—red); view along the crystallographic  $c$  axis. The structure is shown for the solvent-free state, i.e., the Co centers are penta-coordinated; under ambient conditions (humid air), the sixth coordination sites will be occupied by water ligands. (Crystal structure data taken from ref. [23], CCDC 270293; drawing made with VESTA software [31]).

## 2. Materials and Methods

Co-MOF-74 crystals were prepared according to a slightly modified procedure previously published by one of our labs [29]. A total of 750 mg cobalt nitrate hexahydrate ( $\text{Co}(\text{NO}_3)_2 \cdot 6\text{H}_2\text{O}$ , 99% Sigma-Aldrich, Taufkirchen, Germany) was dissolved in a 60 mL mixture of EtOH, DMF and  $\text{H}_2\text{O}$  (1:1:1); afterwards, 144 mg 2,5-dihydroxy-terephthalic acid (DHBCD, 98% Sigma-Aldrich, Taufkirchen, Germany) was added. The suspension was ultrasonicated until the solids were dissolved completely, and subsequently heated to 131 °C for 24 h in a 60 mL Teflon-lined autoclave (Parr Instruments, Frankfurt, Germany). After cooling down to room temperature, the resulting crystals were washed and solvent-exchanged with MeOH. Then, the crystals were dried under reduced pressure and activated under vacuum at 160 °C overnight.

Scanning electron microscopy (SEM) images were obtained with a JEOL JSM-6700F NT microscope at 2 kV acceleration voltage and an emission current of 10  $\mu\text{A}$ . IR spectra of a powder sample were measured with an Agilent Technologies Cary 630 FTIR spectrometer. Raman spectroscopy of single crystals was performed with a Bruker Senterra Raman spectrometer, and a laser excitation wavelength of 532 nm. Temperature-dependent X-ray powder diffraction (XRPD) data at relative humidity of 93% were recorded on a Panalytical Empyrean diffractometer, equipped with a CHC plus+ chamber in a transmittance Bragg–Brentano geometry, employing Cu-radiation. The patterns were recorded in a temperature range of 20–60 °C in 5 °C steps (each followed by a 15 min isothermal step), in the 5–50°  $2\theta$  range.

Impedance measurements were carried out with a Solartron SI 1260 Impedance/Gain-Phase Analyzer and a Novocontrol Alpha-A Analyzer. An experimental setup, as described previously by one of our labs, was used [32]. In short, one individual single Co-MOF-74 crystal was placed on an array of interdigitated Pt electrodes (20  $\mu\text{m}$  electrode width and spacing; UST GmbH, Geratal, Germany) inside a custom-built Faraday cage that was placed in an Espec SH-242 climate chamber. The contact area between the crystal and the electrodes was estimated by confocal laser microscopy (Olympus LEXT OLS 3100, Hamburg, Germany), as shown in the Supplementary Materials section (Figure S1). The humidity was controlled by streaming dry  $\text{N}_2$  through a washing bottle containing deionized water using mass flow controllers. Temperature and humidity of the gas stream were verified by a Sensirion SHT2x sensor. The system was allowed to equilibrate for 12 h after each change in temperature and/or humidity.

### 3. Results and Discussion

The Co-MOF-74 crystals were characterized by SEM, Raman, and IR spectroscopy. Figure 2a shows the SEM image of an exemplary Co-MOF-74 crystal with a representative length of 550  $\mu\text{m}$  and a width around 100  $\mu\text{m}$ . The Raman spectrum (Figure 2b) is in good accordance with previously published MOF-74 Raman data [28]. The peak at 572  $\text{cm}^{-1}$  corresponds to the benzene ring vibration (ring deformation mode), the peak at 818  $\text{cm}^{-1}$  can be assigned to the C-H bending in the benzene ring, the peak at 1281  $\text{cm}^{-1}$  correlates with the C=O stretching, and the O-C-O stretching of the carboxylate group of the organic linker is situated at 1417  $\text{cm}^{-1}$  [33]. Figure 2c shows the IR spectrum, with characteristic peaks at 1401  $\text{cm}^{-1}$  and 1546  $\text{cm}^{-1}$ , corresponding to the symmetric and asymmetric  $\nu(\text{COO})$  stretching of the carboxylic acid group [34]. The measurement was performed under humid air; therefore, the IR spectrum shows a broad band between 2700  $\text{cm}^{-1}$  and 3600  $\text{cm}^{-1}$ , which can be assigned to adsorbed water.

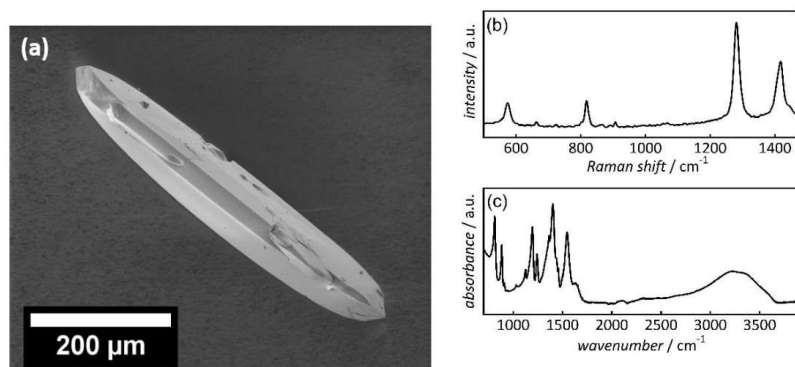


**Figure 2.** (a) Scanning electron microscopic (SEM) image of a Co-MOF-74 crystal (ca. 0.6 mm length); (b) Raman spectrum; (c) IR spectrum.

Hydrothermal stability is one of basic prerequisites regarding potential application of Co-MOF-74 as a proton-conducting material at elevated temperature and under humid conditions. Therefore, we carried out a temperature-resolved powder XRD analysis at a relative humidity of 93%. Figure 3 shows that the material is stable under the tested conditions. We did not observe any changes in the peak positions over the studied temperature range of 20–60  $^{\circ}\text{C}$ . The diffraction patterns are consistent with literature data [25,35]. Some minor changes in the intensity of the first diffraction peak at 6.7 $^{\circ}$  can be attributed to the different solvent content (here water) occupancy inside the pores, as also reported for other MOFs [36,37].

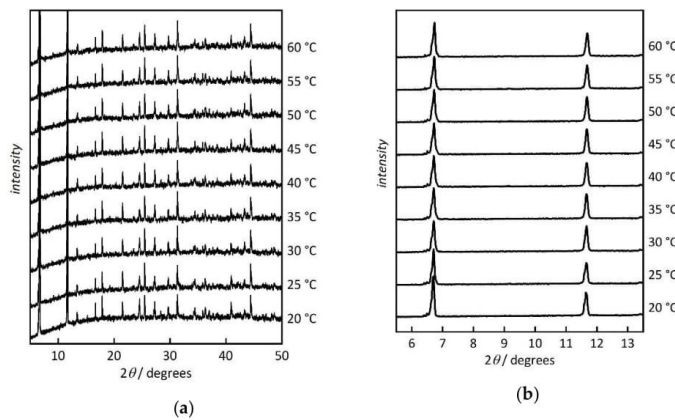


**Figure 3.** Temperature-resolved powder XRD patterns of Co-MOF-74 (at 93% relative humidity). (a) Data range ( $2\theta$ ) from  $5^\circ$  to  $50^\circ$ ; (b) most intense reflections (110 at  $6.5^\circ$ , 300 at  $11.6^\circ$ ). Data are shifted vertically for clarity.

The proton conductance of Co-MOF-74 was studied by AC impedance analysis. The real part of the complex impedance  $Z$  corresponds to the resistance  $R$ , i.e., the reciprocal conductance. The availability of large single crystals made it possible to investigate the material in form of one single crystal, instead of a powder. This eliminates potential difficulties that arise from grain boundary effects or from the impact of surface-adsorbed water in bulk powder or pressed pellets. Most importantly, single-crystal specimens also offer an opportunity to study the anisotropy of proton conductance [30,32,38–41]. Prior to measurement, the material was dried and activated at  $160^\circ\text{C}$ , to remove adsorbed molecules from the micropores. A color change from red to black is observed upon activation. This effect is reversible; subsequent exposure to air at room temperature (with ambient humidity) turns the color back to red. This observation is attributed to de-coordination/coordination of water ligands to cobalt at the ‘open’ coordination site exposed to the interior of the pores [25].

A single crystal was placed on top of an electrode array, as described in the experimental section. It is notable that this method of establishing electrical contact avoids the use of any conductive pastes. Figure 4 shows example Nyquist plots of the impedance  $Z$  (i.e., imaginary part,  $-\text{Im}(Z)$  vs. real part,  $\text{Re}(Z)$ ; frequency range from 10 Hz to 1 MHz, applied potential of 0.1 V) of a Co-MOF-74 single crystal at a temperature of  $25^\circ\text{C}$  and relative humidity of 92%. The crystal with an elongated shape was placed in two distinct orientations relative to the electrodes, perpendicular and parallel. Hence, the proton resistance  $R$  was measured both along the direction of the crystallographic  $c$  axis (blue) and in an orthogonal direction  $a$  axis (red). The Nyquist plots exhibit depressed semi-arcs in the high frequency range that can be modeled by a circuit equivalent consisting of a resistor and a parallel constant phase element, as depicted in the inset of Figure 4. The fit parameters, as well as plots of both the real and imaginary parts vs. the frequency, are shown in the Supporting Information section (Table S2 and Figure S3). Even if the proton conductivity turns out not to reach the values of Nafion [9,10], the data still reveal some interesting findings. A relatively high proton conductivity of  $\sigma = 123 \mu\text{S cm}^{-1}$  (calculated by Equation (S1), Supplementary Materials section) is observed along the  $c$  axis, which corresponds to the direction of the micropore channels in MOF-74 [23]. By comparison, the conductivity in the orthogonal direction is only  $\sigma = 11.7 \mu\text{S cm}^{-1}$ . This is a clear indication that the mobility of the protons is substantially higher along the micropore axis than in the orthogonal direction. Figure 5 shows a plot of the (real part of) the conductivity  $\sigma'$  versus the frequency  $\omega$ . The graphs each exhibit a plateau region (near-zero slope in log-log representation) in the frequency region up to ca. 10 kHz. This (nearly) frequency-independent region marks the material-intrinsic conductivity,

often referred to as 'dc conductivity'. The respective plateau values of  $\sigma'$  (ca.  $100 \mu\text{S cm}^{-1}$  along the pore channel axis, ca.  $10 \mu\text{S cm}^{-1}$  in orthogonal direction) correspond to the  $\sigma$  values calculated from Equation (S1).

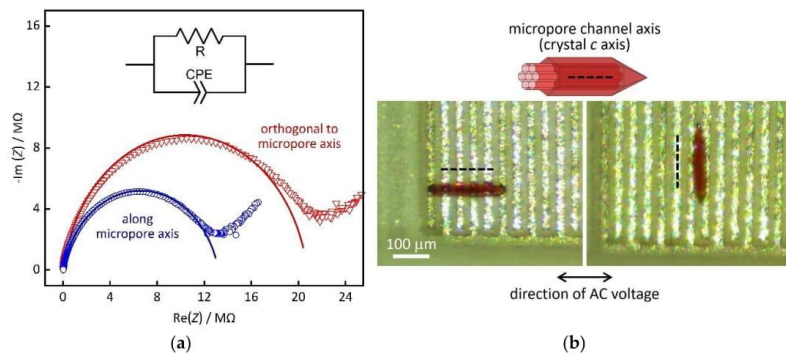


**Figure 4.** (a) Example impedance spectra (Nyquist plots) of a single Co-MOF-74 crystal in two different orientations relative to the contacting electrodes ( $25^\circ\text{C}$ , 92% r.h.). Measured data are plotted as scattered points; the lines represent fits by the circuit equivalent shown in the inset. (b) Photographs of the crystal on top of the interdigitated electrode structure. (Pt electrodes appear as white lines on the green substrate background) and schematic of pore channel orientation.

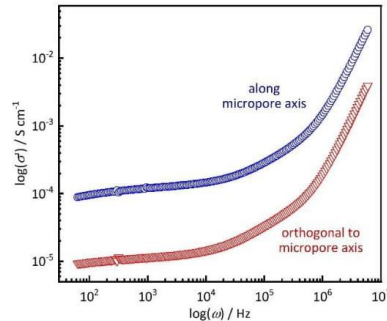


**Figure 5.** Real part of the conductivity ( $\sigma'$ ) as a function of frequency ( $\omega$ ) for the same data as in Figure 4.

In addition to proton mobility, the protonic conductivity also depends on the number of mobile protons. Since water molecules turn out to be responsible for the proton conduction mechanism (as will be shown below), we varied the relative humidity (r.h.) between 70% and 95%, at  $21^\circ\text{C}$  and  $30^\circ\text{C}$  (along the *c* axis). Figure 6 shows a clear impact of humidity; an exponential increase in conductivity (linear increase at logarithmic scale) is observed up to 90% r.h. (data shown in Table S2, Supplementary Materials section). The very strong increase at 95% r.h. is likely attributable to the formation of a continuous liquid water phase, either inside or outside the pores (bulk water condensation). This effect would be tantamount to 'short-circuiting' the sample and, therefore, pose a significant risk to the investigation of intrinsic proton conduction in the MOF material. To avoid such a distortion of the measured data, we used a maximum relative humidity of 90% for all other measurements in this study. (A generally higher conductivity is observed at  $30^\circ\text{C}$  than at  $21^\circ\text{C}$ . The impact of the temperature will be discussed in more detail below.) These findings confirm that the presence of water in the micropores of Co-MOF-74 facilitates protonic conductivity, as frequently observed in MOF materials [30,38,40].

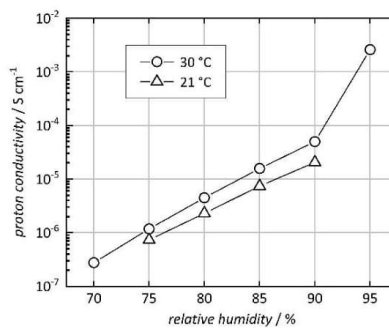


**Figure 6.** Proton conductivity of a Co-MOF-74 single crystal along the crystallographic *c* axis at 21 °C and 30 °C. (Lines connecting the data points are drawn as a guide to the eye.).

To elucidate the mechanism of proton conduction in more detail, we varied the temperature at a constant relative humidity of 90% (data shown in Table S3, Supplementary Materials section). This offers an opportunity to determine the activation energy  $E_A$  for the proton conduction. The conductivity  $\sigma$  is related to the temperature  $T$  by

$$\sigma = \frac{\sigma_0}{k_B T} \exp \left[ \frac{-E_A}{k_B T} \right] \quad (1)$$

where  $\sigma_0$  is a material-specific factor and  $k_B$  is the Boltzmann constant [13]. A linear regression of  $\ln(T\sigma)$  vs.  $T^{-1}$  (Arrhenius plot) delivers  $E_A$  (from the linear slope), as shown in Figure 7. From the data in the temperature range between 21 °C and 30 °C, an activation energy of  $E_A = 0.37$  eV is obtained for the proton conduction in the direction along the micropore axis (*c* axis), while a higher value of  $E_A = 0.87$  eV is found for the orthogonal direction. Further data were measured in the *c* direction between 30 °C and 60 °C, resulting in  $E_A = 0.32$  eV, although, for these measurements, a different crystal was used. These findings strongly suggest that proton conduction in the direction along the micropore axis occurs by a Grotthuss-type mechanism, involving water molecules inside the micropore channels; this is typically associated with activation energies below ca. 0.4 eV [13,42]. In the orthogonal direction, the higher value of  $E_A$  indicates a different mechanism, most likely the diffusion of  $\text{H}_3\text{O}^+$  ions. We assume that such diffusion occurs through surface sorbate layers at the crystal surface, rather than inside the crystal.

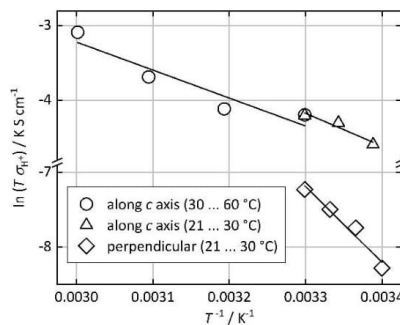


**Figure 7.** Arrhenius plots of the temperature-dependent proton conductivity of Co-MOF-74 single crystals along the crystallographic *c* axis and in the orthogonal direction (90% r.h.). The lines show the linear regression.

#### 4. Conclusions

In summary, we have measured the proton conductivity in Co-MOF-74 single crystals and found a strong anisotropy. High conductivity ( $123 \mu\text{S cm}^{-1}$  at  $25^\circ\text{C}$ ) with a low activation energy (0.32 eV) is observed along the direction of the micropore axis (crystallographic *c* axis). In the orthogonal direction, lower conductivity ( $11.7 \mu\text{S cm}^{-1}$ ) and a high activation energy (0.87 eV) are measured. The proton conductivity is strongly humidity-dependent. These findings suggest that proton conduction occurs predominantly through the micropore channels and that water molecules in the channels provide a proton-conducting path by a Grotthuss-type mechanism.

**Supplementary Materials:** The following are available online at <http://www.mdpi.com/2079-4991/10/7/1263/s1>, Figure S1: Microscopic images; Figure S2: Powder XRD diagram; Figure S3: Data vs. frequency; Table S1: Dimensions of single crystals; Table S2: Fit results; Table S3: All measured data; Equation (S1): Calculation of proton conductivity

**Author Contributions:** A.J. and I.S. developed the conceptual strategies. A.J. conceived the electrochemical setup and measured/evaluated the impedance data, I.S. carried out the synthesis and performed/evaluated the SEM, IR, Raman studies, H.B. performed/evaluated the temperature-resolved XRD study. All authors (A.J., I.S., H.B., J.C., M.T.) evaluated the data and wrote the manuscript. All authors have read and agreed to the published version of the manuscript.

**Funding:** This research was funded by *Deutsche Forschungsgemeinschaft (DFG)* within the priority program 1928: Coordination Networks: Building Blocks for Functional Systems, COORNETS.

**Acknowledgments:** We thank Alexander Reitz for providing confocal laser microscopic images and Alexander Mundstock for fruitful and supportive discussion. I.S. thanks the *Graduierten Akademie* of the Leibniz University Hannover for financial support.

**Conflicts of Interest:** The authors declare no conflict of interest.

#### References

- U.S. Energy Information Administration. *International Energy Outlook 2019 (IEO2019)*; U.S. Energy Information Administration: Washington, DC, USA, 2019; pp. 17–32.
- Fabbri, E.; Pergolesi, D.; Traversa, E. Materials challenges toward proton-conducting oxide fuel cells: A critical review. *Chem. Soc. Rev.* **2010**, *39*, 4355–4369. [\[CrossRef\]](#)
- Wachsman, E.D.; Lee, K.T. Lowering the Temperature of Solid Oxide Fuel Cells. *Science* **2011**, *334*, 935–939. [\[CrossRef\]](#) [\[PubMed\]](#)
- Kravtsberg, A.; Ein-Eli, Y. Review of Advanced Materials for Proton Exchange Membrane Fuel Cells. *Energy Fuels* **2014**, *28*, 7303–7330. [\[CrossRef\]](#)
- Gao, Z.; Mogni, L.V.; Miller, E.C.; Railsback, J.G.; Barnett, S.A. A Perspective on Low-Temperature Solid Oxide Fuel Cells. *Energy Environ. Sci.* **2016**, *9*, 1602–1644. [\[CrossRef\]](#)
- Majlan, E.H.; Rohendi, D.; Dauda, W.R.W.; Husaini, T.; Haque, M.A. Electrode for proton exchange membrane fuel cells: A review. *Renew. Sust. Energ. Rev.* **2018**, *89*, 117–134. [\[CrossRef\]](#)
- Breitwieser, M.; Klingele, M.; Vierrath, S.; Zengerle, R.; Thiele, S. Tailoring the Membrane-Electrode Interface in PEM Fuel Cells: A Review and Perspective on Novel Engineering Approaches. *Adv. Energy Mater.* **2018**, *8*, 1701257. [\[CrossRef\]](#)
- Meyer, Q.; Zeng, Y.; Zhao, C. In Situ and Operando Characterization of Proton Exchange Membrane Fuel Cells. *Adv. Mater.* **2019**, *31*, 1901900. [\[CrossRef\]](#)
- Yee, R.S.L.; Rozendal, R.A.; Zhang, K.; Ladewig, B.P. Cost effective cation exchange membranes: A review. *Chem. Eng. Res.* **2012**, *90*, 950–959. [\[CrossRef\]](#)
- Hamrock, S.J.; Yandrasits, M.A. Proton Exchange Membranes for Fuel Cell Applications. *J. Macromol. Sci. Part C Polym. Rev.* **2006**, *46*, 219–244. [\[CrossRef\]](#)
- Shimizu, G.K.H.; Taylor, J.M.; Kim, S. Proton Conduction with Metal-Organic Frameworks. *Science* **2013**, *341*, 354–355. [\[CrossRef\]](#)
- Yamada, T.; Otsubo, K.; Makiura, R.; Kitagawa, H. Designer coordination polymers: Dimensional crossover architectures and proton conduction. *Chem. Soc. Rev.* **2013**, *42*, 6655–6669. [\[CrossRef\]](#) [\[PubMed\]](#)
- Ramaswamy, P.; Wong, N.E.; Shimizu, G.K.H. MOFs as proton conductors—Challenges and opportunities. *Chem. Soc. Rev.* **2014**, *43*, 5913–5932. [\[CrossRef\]](#) [\[PubMed\]](#)

14. Tominaka, S.; Cheetham, A.K. Intrinsic and extrinsic proton conductivity in metal-organic frameworks. *RSC Adv.* **2014**, *4*, 54382–54387. [\[CrossRef\]](#)
15. Nagarkar, S.S.; Unni, S.M.; Sharma, A.; Kurungot, S.; Ghosh, S.K. Two-in-One: Inherent Anhydrous and Water-Assisted High Proton Conduction in a 3D Metal-Organic Framework. *Angew. Chem. Int. Ed.* **2014**, *53*, 2638–2642. [\[CrossRef\]](#)
16. Moghadam, P.Z.; Li, A.; Wiggin, S.B.; Tao, A.; Maloney, A.G.P.; Wood, P.A.; Ward, S.C.; Fairen-Jimenez, D. Development of a Cambridge Structural Database Subset: A Collection of Metal-Organic Frameworks for Past, Present, and Future. *Chem. Mater.* **2017**, *29*, 2618–2625. [\[CrossRef\]](#)
17. Yin, Z.; Wan, S.; Yang, J.; Kurmoo, M.; Zeng, M.-H. Recent advances in post-synthetic modification of metal-organic frameworks: New types and tandem reactions. *Coord. Chem. Rev.* **2019**, *378*, 500–512. [\[CrossRef\]](#)
18. Kitagawa, S.; Kitaura, R.; Noro, S. Functional porous coordination polymers. *Angew. Chem. Int. Ed.* **2004**, *43*, 2334–2375. [\[CrossRef\]](#) [\[PubMed\]](#)
19. Ferey, G. Hybrid porous solids: Past, present, future. *Chem. Soc. Rev.* **2008**, *37*, 191–214. [\[CrossRef\]](#)
20. Tranchemontagne, D.J.; Mendoza-Cortés, J.L.; O’Keeffe, M.; Yaghi, O.M. Secondary building units, nets and bonding in the chemistry of metal-organic frameworks. *Chem. Soc. Rev.* **2009**, *38*, 1257–1283. [\[CrossRef\]](#)
21. Czaja, A.U.; Trukhan, N.; Müller, U. Industrial applications of metal-organic frameworks. *Chem. Soc. Rev.* **2009**, *38*, 1284–1293. [\[CrossRef\]](#)
22. Furukawa, H.; Cordova, K.E.; O’Keeffe, M.; Yaghi, O.M. The Chemistry and Applications of Metal-Organic Frameworks. *Science* **2013**, *341*, 1230444. [\[CrossRef\]](#) [\[PubMed\]](#)
23. Dietzel, P.D.C.; Morita, Y.; Blom, R.; Fjellvåg, H. An In Situ High-Temperature Single-Crystal Investigation of a Dehydrated Metal-Organic Framework Compound and Field-Induced Magnetization of One-Dimensional Metal-Oxygen Chains. *Angew. Chem. Int. Ed.* **2005**, *44*, 6354–6358. [\[CrossRef\]](#) [\[PubMed\]](#)
24. Rosi, N.L.; Kim, J.; Eddaoudi, M.; Chen, B.; O’Keeffe, M.; Yaghi, O.M. Rod Packings and Metal-Organic Frameworks Constructed from Rod-Shaped Secondary Building Units. *J. Am. Chem. Soc.* **2005**, *127*, 1504–1518. [\[CrossRef\]](#)
25. Chmelik, C.; Mundstock, A.; Dietzel, P.D.C.; Caro, J. Idiosyncrasies of  $\text{Co}_2(\text{dhtp})$ : In situ-annealing by methanol. *Microporous Mesoporous Mater.* **2014**, *183*, 117–123. [\[CrossRef\]](#)
26. Valvekens, P.; Vandichel, M.; Waroquier, M.; Van Speybroeck, V.; De Vos, D. Metal-dioxidoterephthalate MOFs of the MOF-74 type: Microporous basic catalysts with well-defined active sites. *J. Catal.* **2014**, *317*, 1–10. [\[CrossRef\]](#)
27. Dietzel, P.D.C.; Besikiotis, V.; Blom, R. Application of metal-organic frameworks with coordinatively unsaturated metal sites in storage and separation of methane and carbon dioxide. *J. Mater. Chem.* **2009**, *19*, 7362–7370. [\[CrossRef\]](#)
28. Strauss, I.; Mundstock, A.; Hinrichs, D.; Himstedt, R.; Knebel, A.; Reinhardt, C.; Dorfs, D.; Caro, J. The Interaction of Guest Molecules with Co-MOF-74: A Vis/NIR and Raman Approach. *Angew. Chemie Int. Ed.* **2018**, *57*, 7434–7439. [\[CrossRef\]](#) [\[PubMed\]](#)
29. Strauss, I.; Mundstock, A.; Treger, M.; Lange, K.; Hwang, S.; Chmelik, C.; Rusch, P.; Bigall, N.C.; Pichler, T.; Shiozawa, H.; et al. Metal-Organic Framework Co-MOF-74-Based Host–Guest Composites for Resistive Gas Sensing. *ACS Appl. Mater. Interfaces* **2019**, *11*, 14175–14181. [\[CrossRef\]](#)
30. Hwang, S.; Lee, E.J.; Song, D.; Jeong, N.C. High Proton Mobility with High Directionality in Isolated Channels of MOF-74. *ACS Appl. Mater. Interfaces* **2018**, *10*, 35354–35360. [\[CrossRef\]](#)
31. Momma, K.; Izumi, F. VESTA 3 for three-dimensional visualization of crystal, volumetric and morphology data. *J. Appl. Crystallogr.* **2011**, *44*, 1272–1276. [\[CrossRef\]](#)
32. Javed, A.; Wagner, T.; Wöhlbrandt, S.; Stock, N.; Tiemann, M. Proton Conduction in a Single Crystal of a Phosphonato-Sulfonate-Based Coordination Polymer: Mechanistic Insight. *ChemPhysChem* **2020**, *21*, 605–609. [\[CrossRef\]](#) [\[PubMed\]](#)
33. Bonino, F.; Chavan, S.; Vitillo, J.G.; Groppo, E.; Agostini, G.; Lamberti, C.; Dietzel, P.D.C.; Prestipino, C.; Bordiga, S. Local Structure of CPO-27-Ni Metallorganic Framework upon Dehydration and Coordination of NO. *Chem. Mater.* **2008**, *20*, 4957–4968. [\[CrossRef\]](#)
34. Zhao, Z.; Zuhra, Z.; Qin, L.; Zhou, Y.; Zhang, L.; Tang, F.; Mu, C. Confinement of microporous MOF-74(Ni) within mesoporous  $\gamma\text{-Al}_2\text{O}_3$  beads for excellent ultra-deep and selective adsorptive desulfurization performance. *Fuel Process. Technol.* **2018**, *176*, 276–282. [\[CrossRef\]](#)

35. Dietzel, P.D.C.; Johnsen, R.E.; Blom, R.; Fjellvåg, H. Structural Changes and Coordinatively Unsaturated Metal Atoms on Dehydration of Honeycomb Analogous Microporous Metal–Organic Frameworks. *Chem. Eur. J.* **2008**, *14*, 2389–2397. [[CrossRef](#)] [[PubMed](#)]
36. Canivet, J.; Fateeva, A.; Guo, Y.; Coasne, B.; Farrusseng, D. Water adsorption in MOFs: Fundamentals and applications. *Chem. Soc. Rev.* **2014**, *43*, 5594–5617. [[CrossRef](#)]
37. Øien-Ødegaard, S.; Shearer, G.C.; Wragg, D.S.; Lillerud, K.P. Pitfalls in metal–organic framework crystallography: Towards more accurate crystal structures. *Chem. Soc. Rev.* **2017**, *46*, 4867–4876. [[CrossRef](#)]
38. Yoon, M.; Suh, K.; Kim, H.; Kim, Y.; Selvapalam, N.; Kim, K. High and Highly Anisotropic Proton Conductivity in Organic Molecular Porous Materials. *Angew. Chem. Int. Ed.* **2011**, *50*, 7870–7873. [[CrossRef](#)]
39. Tominaka, S.; Henke, S.; Cheetham, A.K. Coordination polymers of alkali metal trithiocyanurates: Structure determinations and ionic conductivity measurements using single crystals. *Cryst. Eng. Comm.* **2013**, *15*, 9400–9407. [[CrossRef](#)]
40. Li, R.; Wang, S.H.; Chen, X.X.; Lu, J.; Fu, Z.H.; Li, Y.; Xu, G.; Zheng, F.K.; Guo, G.C. Highly Anisotropic and Water Molecule-Dependent Proton Conductivity in a 2D Homochiral Copper(II) Metal-Organic Framework. *Chem. Mater.* **2017**, *29*, 2321–2331. [[CrossRef](#)]
41. Bunzen, H.; Javed, A.; Klawinski, D.; Lamp, A.; Grzywa, M.; Kalytta-Mewes, A.; Tiemann, M.; von Nidda, H.-A.K.; Wagner, T.; Volkmer, D. Anisotropic Water-Mediated Proton Conductivity in Large Iron(II) Metal–Organic Framework Single Crystals for Proton-Exchange Membrane Fuel Cells. *ACS Appl. Nano Mater.* **2019**, *2*, 291–298. [[CrossRef](#)]
42. Kreuer, K.-D. Proton Conductivity: Materials and Applications. *Chem. Mater.* **1996**, *8*, 610–641. [[CrossRef](#)]



© 2020 by the authors. Licensee MDPI, Basel, Switzerland. This article is an open access article distributed under the terms and conditions of the Creative Commons Attribution (CC BY) license (<http://creativecommons.org/licenses/by/4.0/>).

# Humidity-mediated Anisotropic Proton Conductivity through the 1D Channels of Co-MOF-74

## Supplementary Material

Ali Javed <sup>1</sup>, Ina Strauss <sup>2</sup>, Hana Bunzen <sup>3</sup>, Jürgen Caro <sup>2</sup>, and Michael Tiemann <sup>1</sup>

<sup>1</sup> Department of Chemistry, Paderborn University, 33098 Paderborn, Germany

<sup>2</sup> Institute of Physical Chemistry and Electrochemistry, Leibniz University Hannover, 30167 Hannover, Germany

<sup>3</sup> Institute of Physics, University of Augsburg, 86159 Augsburg, Germany

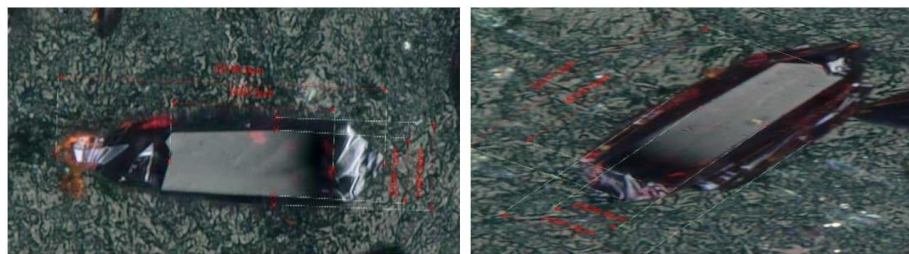


**Figure S1.** Microscopic images of two Co-MOF-74 crystals for the evaluation of the contact area in equation S1.

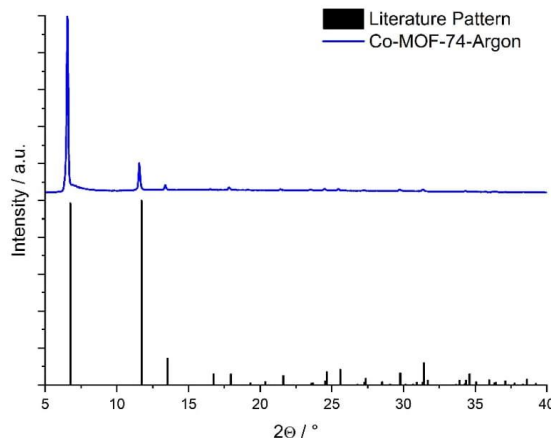


**Figure S2.** Experimental and simulated powder XRD pattern of Co-MOF-74 [1].

[1] Strauss, I.; Mundstock, A.; Hinrichs, D.; Himstedt, R.; Knebel, A.; Reinhardt, C.; Dorfs, D.; Caro, J. *Angew. Chemie Int. Ed.* **2018**, *57*, 7434–7439.

**Table S1.** Dimensions of Co-MOF-74 single crystals and contact lengths/widths with underlying flat substrate, determined from Figure S1. The values are used as correcting factors for the assessment of the contact area in equation S1.

crystal #	length	contact length	width	contact width
1	45.6 $\mu\text{m}$	34.1 $\mu\text{m}$ (74.8%)	190.9 $\mu\text{m}$	95 $\mu\text{m}$ (49.8%)
2	141.2 $\mu\text{m}$	105.0 $\mu\text{m}$ (74.8%)	57 $\mu\text{m}$	26 $\mu\text{m}$ (45.6%)

**Equation S1.** Calculation of the proton conductivity  $\sigma$  from the measured proton resistance  $R$  and the contact area with the Pt electrodes ( $A$ : contact area between sample and the Pt electrode array;  $n$ : number of spacings between electrodes,  $D$ : inter-electrode distance (20  $\mu\text{m}$ ),  $d$ : electrode width (20  $\mu\text{m}$ ),  $a$ : width of crystal) [2].

$$\sigma = n \cdot (D / (R \cdot A)) = n \cdot (D / (R \cdot a \cdot d)) \quad (\text{S1})$$

**Table S2.** Fit results for the spectra in Figure 4.

	along micropore axis	orthogonal to axis
$\chi^2$	0.015	0.014
CPE- $T$	$1.8753 \times 10^{-11}$	$1.4715 \times 10^{-11}$
CPE- $P$	0.88579	0.89969
$R / \Omega$	$1.278 \times 10^7$	$2.072 \times 10^7$

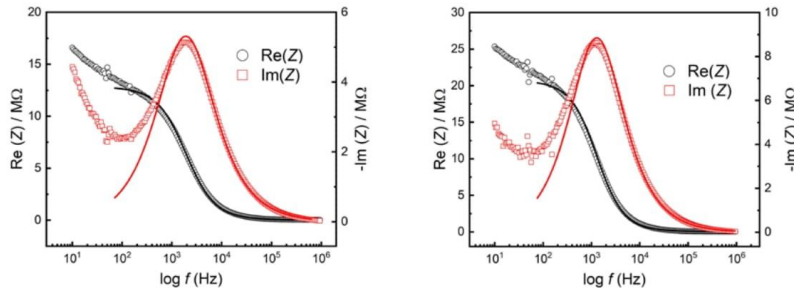


**Figure S3.** Real and imaginary parts of the impedance *vs.* frequency of a single Co-MOF-74 crystal in two different orientations relative to the contacting electrodes (25 °C, 92% r.h.): along (left) and orthogonal (right) to the micropore axis.

**Table S3.** All measured proton conductivity values of Co-MOF-74 crystals under variable conditions.

sample name	proton current direction	T / °C	r.h. / %	proton conductivity $\sigma / \mu\text{S cm}^{-1}$
Co-74_1	=	25	92	123
	≠	25	92	11.7
Co-74_2	=	21	75	0.732
	=	21	80	2.29
	=	21	85	7.38
	=	21	90	20.4
Co-74_3	=	22	90	34.4
	=	26	90	45.5
	=	30	90	49.6
Co-74_4	≠	21	90	0.862
	≠	24	90	1.46
	≠	27	90	1.85
	≠	30	90	2.40
Co-74_5	=	30	70	0.27
	=	30	75	1.18
	=	30	80	4.48
	=	30	85	15.7
	=	30	90	49.8
	(=)	(30)	(95)	(2590) <sup>2</sup>
	=	40	90	52.3
	=	50	90	77.7
	=	60	90	137

<sup>1</sup> "=": along *c* axis; "≠": orthogonal    <sup>2</sup> (presumed bulk water condensation)

## 5.2.3 Published Data Details

### 5.2.3.1 Fittings Parameters

Table 5.2.1. Description of the fittings produced using the equivalent circuit model for Co-MOF-74, at different setpoints of relative humidity and temperature, specifically for crystal orientation with respect to IDE.

sample name	proton current direction	T [°C]	rh [%]	chi-sqr.	n	Q	R [Ω]
Co-74_1	=	25	95	0.015	0.88	1.87E-11	1.27E7
	≠	25	95	0.014	0.89	1.47E-11	2.07E7
	=	21	75	0.070	0.95	5.79E-12	1.62E9
Co-74_2	=	21	80	0.072	0.86	6.75E-12	5.18E8
	=	21	85	0.077	0.86	9.14E-12	1.60E8
	=	21	90	0.064	0.86	1.33E-11	5.80E7
Co-74_3	=	22	90	0.081	0.95	6.44E-12	1.16E7
	=	26	90	0.091	0.95	6.37E-12	8.64E5
	=	30	90	0.081	0.94	7.65E-12	7.93E5
Co-74_4	≠	21	90	0.018	0.93	8.03E-12	4.18E7
	≠	24	90	0.019	0.92	1.07E-11	2.46E7
	≠	27	90	0.019	0.91	1.15E-11	1.94E7
Co-74_5	≠	30	90	0.021	0.91	1.28E-11	1.50E7
	=	30	70	0.030	0.98	3.67E-12	7.65E9
	=	30	75	0.067	0.98	3.92E-12	1.78E9
	=	30	80	0.044	0.98	4.14E-12	4.62E8
	=	30	85	0.029	0.97	4.14E-12	1.33E8
	=	30	90	0.022	0.96	5.18E-12	4.21E7
	=	30	95	0.013	0.80	7.97E-11	8.09E5
	=	40	90	0.019	0.93	8.12E-12	4.03E7
	=	50	90	0.015	0.92	1.08E-11	2.71E7
	=	60	90	0.017	0.91	1.28E-11	1.52E7

where, “=”: along c axis; “≠”: along orthogonal

The parameters  $n$  and  $Q$  were generated by using constant phase elements CPE. Z-View software identifies  $n$  and  $Q$  with  $P$  and  $T$ , respectively.

### 5.2.3.2 Nyquist Plots

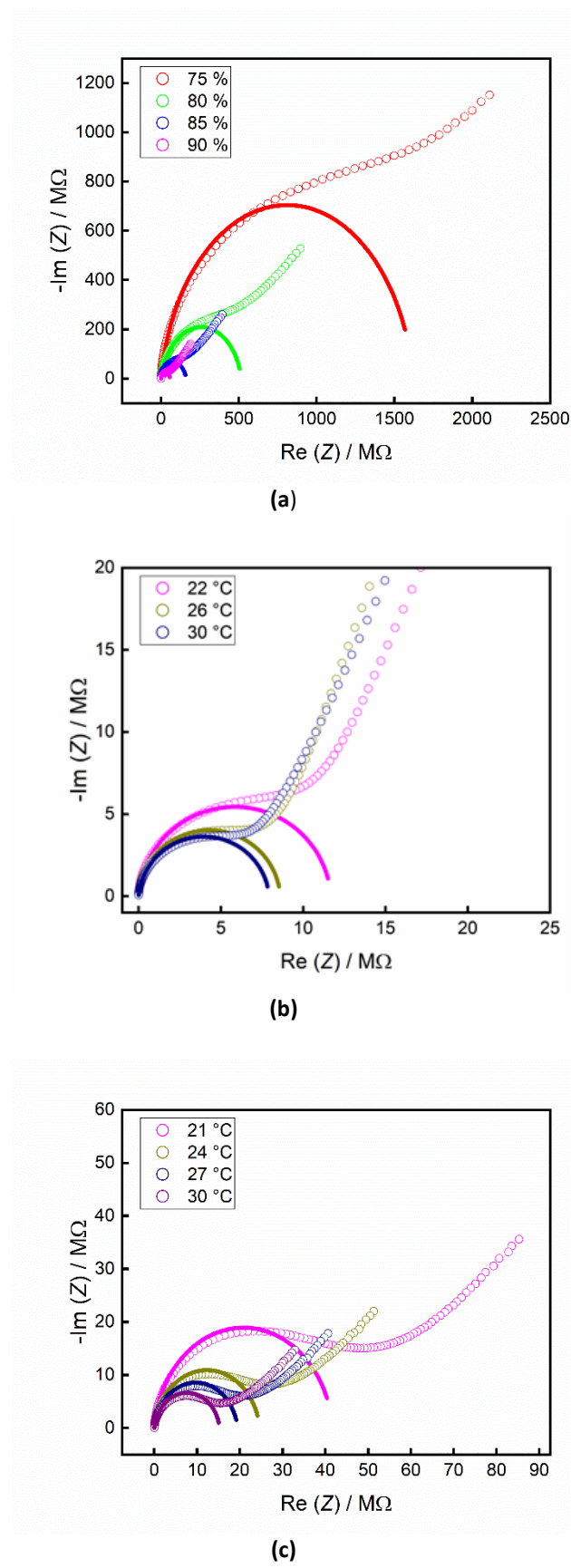
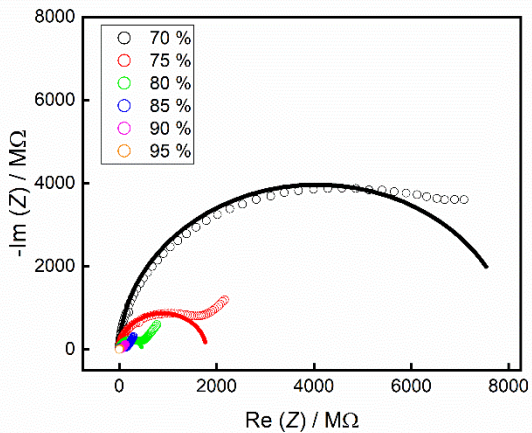
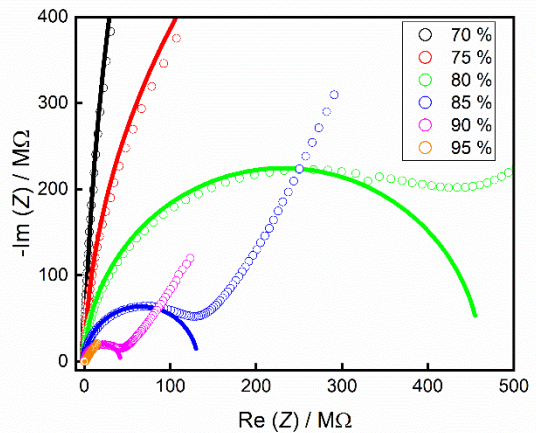


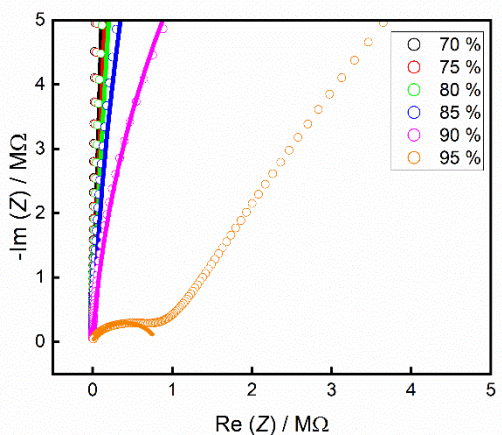
Figure 5.2.1. Nyquist plots for single crystal Co-MOF-74 samples (a) Co-74\_2: along c-axis at 21 °C and 70 % ... 90 % rh (b) Co-74\_3: along c-axis at 90 % rh and 22 °C ... 30 °C temperature (c) Co-74\_4: along orthogonal direction at 90 % rh and 21 °C ... 30 °C temperature.



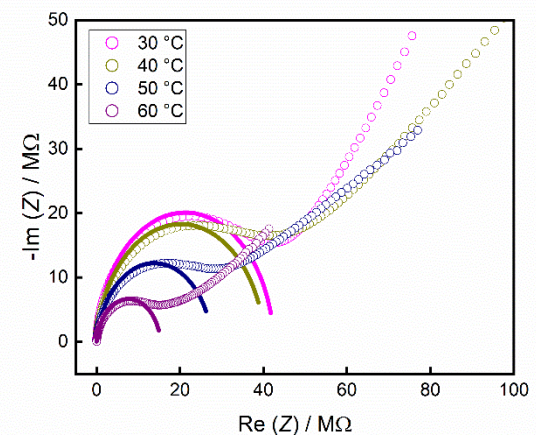
(a)



(b)



(c)



(d)

Figure 5.2.2. Nyquist plots for single crystal Co-MOF-74 sample, Co-74\_5 along c-axis (a) at 30 °C and 70 % ... 95 % rh (b) zoom-in view of (a), and (c) zoom-in view of (b), and (d) at 90 % rh and 30 °C ... 60 °C temperature.

## 5.3 The Role of Sulfonate Groups and Hydrogen Bonding in the Proton Conductivity of Two Coordination Networks

**Ali Javed**, Felix Steinke, Stephan Wöhlbrandt, Hana Bunzen, Nobert Stock, and Michael Tiemann

**DOI:** [10.3762/bjnano.13.36](https://doi.org/10.3762/bjnano.13.36)

### 5.3.1 Outline and Outcome

Recently, this article was published in an open access journal "Beilstein Journal of Nanotechnology". In hunt for novel crystalline materials, this study demonstrates the proton conductivity of two coordination networks which differ in their metal centers, such as Mg and Pb, and use the same linker molecule as that used in studying Ba-CP. Felix Steinke followed the procedure published by Stephan to synthesize and characterize both compounds.<sup>[98]</sup> Hana Bunzen verified the hydrothermal stability up to 50 °C at 90 % relative humidity. The author of this thesis accomplished the remaining activities associated to impedance measurements.

The crystal structure analysis of  $[\text{Mg}(\text{H}_2\text{O})_2(\text{H}_3\text{L})]\cdot\text{H}_2\text{O}$  (**Mg-CP**) uncovered the layered structure in which inside the interlayer spacing, the uncoordinated sulfonate group of the linker is pointed which offers high degree of hydrogen bonding. In contrast, this sulfonic acid group is coordinated to  $\text{Pb}^{+2}$  ions in  $[\text{Pb}_2(\text{HL})]\cdot\text{H}_2\text{O}$  (**Pb-MOF**), which exhibited 3D-framework structure. This is due to lower linker connectivity of Mg-CP as compared to Pb-MOF. Moreover, the permanent porosity ( $2 \times 4 \text{ \AA}$ ) of Pb-MOF made it first porous phosphonato-sulfonate based MOF. Another feature of this found by vapor sorption measurement was the reversible uptake of water.<sup>[98]</sup> Using these structural differences as a basis, the proton conductivity of both compounds was examined in this study.

The samples were obtained as very small colorless crystals. Therefore, the single crystal investigation was hampered, and through-plane impedance measurements were performed with pressed pellets. Both samples featured water-mediated proton conductivity, with Mg-CP having two orders of magnitude higher conductivity than Pb-MOF. Surprisingly, a grain-boundary effect was noticed with Mg-CP that was eliminated by the thermal activation treatment. Furthermore, reversible water uptake was observed in Pb-MOF. Concerning to  $E_A$  before and after thermal activation, Mg-CP expressed the "proton hopping" based on non-

coordinated sulfonate group between the layers. However, results from Pb-MOF identified no long-range hydrogen bonding since no free sulfonate sites were present.

### 5.3.2 Manuscript



## The role of sulfonate groups and hydrogen bonding in the proton conductivity of two coordination networks

Ali Javed<sup>1</sup>, Felix Steinke<sup>2</sup>, Stephan Wöhlbrandt<sup>2</sup>, Hana Bunzen<sup>3</sup>, Norbert Stock<sup>2</sup> and Michael Tiemann<sup>\*1</sup>

### Full Research Paper

### Open Access

#### Address:

<sup>1</sup>Department of Chemistry, Paderborn University, 33098 Paderborn, Germany, <sup>2</sup>Institute of Inorganic Chemistry, Christian-Albrecht University, Kiel, Germany and <sup>3</sup>Institute of Physics, University of Augsburg, 86159 Augsburg, Germany

#### Email:

Michael Tiemann<sup>\*</sup> - michael.tiemann@upb.de

#### \* Corresponding author

#### Keywords:

coordination network; coordination polymer; impedance spectroscopy; metal-organic framework; proton conductivity

*Beilstein J. Nanotechnol.* **2022**, *13*, 437–443.  
<https://doi.org/10.3762/bjnano.13.36>

Received: 18 January 2022

Accepted: 27 April 2022

Published: 04 May 2022

Associate Editor: P. Leiderer

© 2022 Javed et al.; licensee Beilstein-Institut.  
License and terms: see end of document.

### Abstract

The proton conductivity of two coordination networks,  $[\text{Mg}(\text{H}_2\text{O})_2(\text{H}_3\text{L})]\cdot\text{H}_2\text{O}$  and  $[\text{Pb}_2(\text{HL})]\cdot\text{H}_2\text{O}$  ( $\text{H}_3\text{L} = (\text{H}_2\text{O}_3\text{PCH}_2)_2\text{NCH}_2\text{C}_6\text{H}_4\text{SO}_3\text{H}$ ), is investigated by AC impedance spectroscopy. Both materials contain the same phosphonato-sulfonate linker molecule, but have clearly different crystal structures, which has a strong effect on proton conductivity. In the Mg-based coordination network, dangling sulfonate groups are part of an extended hydrogen bonding network, facilitating a “proton hopping” with low activation energy; the material shows a moderate proton conductivity. In the Pb-based metal-organic framework, in contrast, no extended hydrogen bonding occurs, as the sulfonate groups coordinate to  $\text{Pb}^{2+}$ , without forming hydrogen bonds; the proton conductivity is much lower in this material.

### Introduction

Recent achievements in the synthesis of advanced functional materials with tailored, structure-related physical properties have stimulated the development of new concepts and devices for energy storage [1,2] and energy conversion [3,4]. Among these, proton-conducting solid materials show significant potential in the development of novel membranes for proton exchange membrane (PEM) fuel cells, PEM electrolyzers, and for humidity sensors [5-7]. The goal is to overcome the restric-

tions of state-of-the-art proton-conducting membrane materials such as Nafion. Despite its high proton conductivity of ca.  $0.1 \text{ S}\cdot\text{cm}^{-1}$  at  $80^\circ\text{C}$  and 98% relative humidity (r.h.), Nafion exhibits some shortcomings, including high cost, sophisticated manufacturing processes, and stringent operating conditions [8]. Therefore, a variety of new functional network materials are currently being discussed as potential alternatives. These include coordination polymers (CPs), covalent organic frame-

works (COFs), polyoxometalates (POMs), hydrogen-bonded organic frameworks (HOFs), and mesoporous organosilica materials (MPOs) [3,9–11]. In particular, proton-conducting coordination polymers (CPs), such as (porous) metal-organic frameworks (MOFs) and (non-porous, yet cross-linked) coordination networks [12], may offer alternatives to Nafion because of their structural controllability and high crystallinity [13].

The quest to develop new proton-conducting network materials is associated with the requirement to understand conduction mechanisms and to identify the necessary characteristics of the crystal structures of the materials [14]. This will offer new options to design structures with appropriate functionalities, such as (i) by introducing or replacing functional groups of the bridging ligands, for example,  $-\text{OH}$ ,  $-\text{COOH}$ ,  $-\text{PO}_3\text{H}_2$  or  $-\text{SO}_3\text{H}$ , (ii) by filling pores or channels with acidic guest molecules, such as oxonium ions, organic or inorganic acids, or ammonium cations, or (iii) by ligand substitution to increase the mobility of proton carriers [13–16]. Here we report an investigation of proton conductivity in two coordination networks that contain the same phosphonato-sulfonate linker, but different metal nodes, namely  $\text{Pb}^{2+}$  and  $\text{Mg}^{2+}$  [17]. The materials exhibit different crystal structures, and both show a certain, though moderate, proton conductivity that is strongly humidity- and temperature-dependent. We discuss how differences in the conduction behavior may be related to the respective structural properties.

## Results and Discussion

The compounds  $[\text{Mg}(\text{H}_2\text{O})_2(\text{H}_3\text{L})]\text{H}_2\text{O}$  and  $[\text{Pb}_2(\text{HL})]\text{H}_2\text{O}$  were synthesized using the linker molecule  $\text{H}_3\text{L}$  (see Supporting Information File 1, Figure S1) and magnesium chloride hexahydrate ( $\text{MgCl}_2 \cdot 6\text{H}_2\text{O}$ ) or lead acetate hydrate ( $(\text{Pb}(\text{OAc})_3 \cdot \text{H}_2\text{O}$ ), respectively, under solvothermal reaction conditions, employing mixtures of water and ethanol as solvent.

In the case of  $[\text{Mg}(\text{H}_2\text{O})_2(\text{H}_3\text{L})]\text{H}_2\text{O}$ , sodium hydroxide was used as an additive [13]. Crystallographic and experimental details, as well as an extended structure characterization and discussion is provided in [17]. In brief, both compounds crystallize in the same monoclinic space group ( $P2_1/c$ , Nr. 14) but exhibit fundamentally different crystal structures (Figure 1).  $[\text{Mg}(\text{H}_2\text{O})_2(\text{H}_3\text{L})]\text{H}_2\text{O}$  is a 2D coordination network ( $\text{I}^2\text{O}^0$ ) network following the classification by Cheetham et al. [18], with a 2D inorganic building unit consisting of corner-sharing  $\text{CPO}_3$  and  $\text{MgO}_6$  polyhedra. Each  $\text{Mg}^{2+}$  ion is surround by four different phosphonate groups and two aqua ligands, with the phosphonate groups bridging two metal ions, resulting in the formation of layers. This way, each phosphonate group is coordinating with two oxygen atoms, while the third one is protonated. The  $-\text{C}_6\text{H}_4\text{SO}_3$  group points into the interlayer space. A network of hydrogen bonds between the sulfonate residues and coordinated water molecules as well as crystal water interconnect the layers into a three-dimensional network consisting of interlocked layers. In contrast, in the structure of  $[\text{Pb}_2(\text{HL})]\text{H}_2\text{O}$ , each sulfonate group is coordinating to several  $\text{Pb}^{2+}$  ions. A 2D inorganic building unit is observed and the coordination of the sulfonate groups results in the formation of a 3D coordination network ( $\text{I}^2\text{O}^1$ ) exhibiting ultramicropores ( $2 \times 4 \text{ \AA}$ ) [17]. Therefore, in contrast to the magnesium-based compound,  $[\text{Pb}_2(\text{HL})]\text{H}_2\text{O}$  can be denoted as a metal-organic framework [12]. It is noteworthy that solely H bonds with adsorbed water molecules are found. Crystallographic and experimental details, as well as an extended structure discussion is provided in [17].

The proton conductivity of  $[\text{Mg}(\text{H}_2\text{O})_2(\text{H}_3\text{L})]\text{H}_2\text{O}$  (in the following: Mg-CP) and  $[\text{Pb}_2(\text{HL})]\text{H}_2\text{O}$  (in the following: Pb-MOF) was investigated by AC impedance analysis [19,20]. For this purpose, the materials were pressed into pellets and placed between plate electrodes without further auxiliary

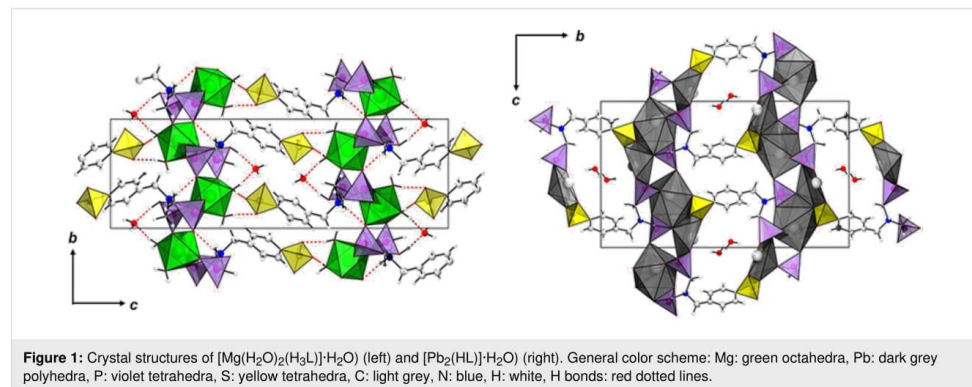


**Figure 1:** Crystal structures of  $[\text{Mg}(\text{H}_2\text{O})_2(\text{H}_3\text{L})]\text{H}_2\text{O}$  (left) and  $[\text{Pb}_2(\text{HL})]\text{H}_2\text{O}$  (right). General color scheme: Mg: green octahedra, Pb: dark grey polyhedra, P: violet tetrahedra, S: yellow tetrahedra, C: light grey, N: blue, H: white, H bonds: red dotted lines.

measures, such as the usage of conductive paste. A potential of 0.1 V was chosen for the entire study, after making sure that lower or higher potentials do not affect the measurements in any significant way (see Supporting Information File 1, Figure S2). Figure 2 shows the Nyquist plots of the impedance spectra (i.e., imaginary vs real part of the impedance  $Z$ ) for both materials at 22 °C and 90% r.h., before and after thermal activation. The term “thermal activation” here stands for exposure to 80 °C at ambient pressure for 24 h in dry air. This process is supposed to remove surface-adsorbed water, such as residues from the synthesis process or from exposure to humid conditions. Powder X-ray diffraction confirmed that this process does not affect the crystallinity of the two materials, and no phase transformation was observed (see Supporting Information File 1, Figure S3 and Figure S4). The Nyquist plots show depressed semicircles in the high-frequency region (i.e., region of low  $\text{Re}(Z)$ ) that allow for the determination of the proton conductance by fitting an appropriate equivalent circuit model. Here, the model consists of a resistor and a parallel constant phase element (Supporting Infor-

mation File 1, Figure S5a). However, in case of the non-activated Mg-CP sample, a second pair of resistor and parallel constant phase element, serial to the first pair (Supporting Information File 1, Figure S5b), was found to be necessary, as will be discussed below. The proton conductivity  $\sigma$  is then calculated from the resistance  $R$  by accounting for the thickness  $L$  and contact area  $A$  of the sample pellet between the two electrodes ( $\sigma = R^{-1} \cdot L \cdot A^{-1}$ ) [21]. The results are shown in Table 1. Further conductivity values at 22 °C are plotted in Figure 3 for r.h. values between 70% and 90%. A strong impact of humidity is observed for both materials; obviously, proton conduction is strongly mediated by water, as frequently observed for similar materials [22,23].

The Pb-MOF sample shows an overall very low proton conductivity. The value increases from  $4.9 \times 10^{-10} \text{ S} \cdot \text{cm}^{-1}$  at 70% r.h. to  $2.0 \times 10^{-8} \text{ S} \cdot \text{cm}^{-1}$  at 90% r.h. (non-activated sample, 22 °C). Activation only leads to a very slight change in conductivity ( $9.9 \times 10^{-9} \text{ S} \cdot \text{cm}^{-1}$  at 90% r.h., see Table 1). These findings

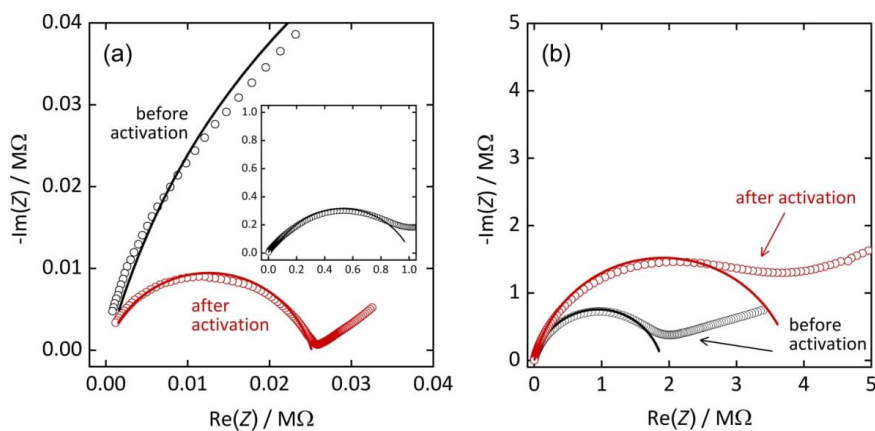


**Figure 2:** Nyquist plots (imaginary vs real part of impedance  $Z$ ) of (a)  $[\text{Mg}(\text{H}_2\text{O})_2(\text{H}_3\text{L})]\cdot\text{H}_2\text{O}$  and (b)  $[\text{Pb}_2(\text{HL})]\cdot\text{H}_2\text{O}$ , before and after thermal activation. Measurements were conducted at 22 °C and 90% r.h.; lines represent the fit results from using the equivalent circuits described in the text.

**Table 1:** Proton conductivity of  $[\text{Mg}(\text{H}_2\text{O})_2(\text{H}_3\text{L})]\cdot\text{H}_2\text{O}$  (Mg-CP) and  $[\text{Pb}_2(\text{HL})]\cdot\text{H}_2\text{O}$  (Pb-MOF), before and after thermal activation.

	before thermal activation	after thermal activation	
	$\sigma / \text{S} \cdot \text{cm}^{-1}$	$E_A / \text{eV}$	$\sigma / \text{S} \cdot \text{cm}^{-1}$
Pb-MOF	$2.0 \times 10^{-8}$	$0.17 \pm 0.02$	$9.9 \times 10^{-9}$
Mg-CP	$3.0 \times 10^{-6}$ ( $1.40 \times 10^{-7}$ ) <sup>a</sup>	$0.40 \pm 0.05$ ( $0.64 \pm 0.01$ ) <sup>a</sup>	$3.6 \times 10^{-6}$

<sup>a</sup>The second values correspond to the conduction mode that is irreversibly erased by thermal activation.

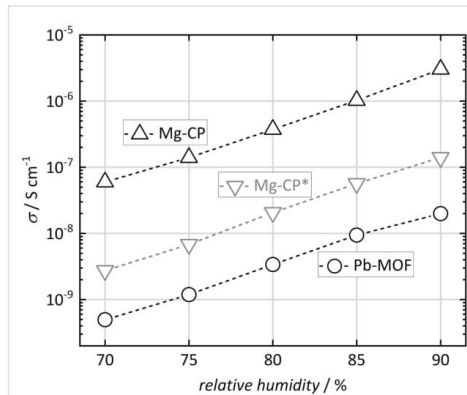


**Figure 3:** Proton conductivity (dashed lines as a guide to the eye) of  $[\text{Mg}(\text{H}_2\text{O})_2(\text{H}_3\text{L})]\text{H}_2\text{O}$  (Mg-CP) and  $[\text{Pb}_2(\text{HL})]\text{H}_2\text{O}$  (Pb-MOF) at variable relative humidity (22 °C, before thermal activation). \*The lower values for Mg-CP (gray) correspond to the conduction mode that is irreversibly erased by thermal activation.

suggest that proton mobility is mostly governed by the (reversible) uptake of water, either inside or outside the pores of Pb-MOF.

The Mg-CP sample shows a more interesting behavior. Its conductivity lies in the range between  $6 \times 10^{-8}$  S·cm<sup>-1</sup> (70% r.h.) and  $3 \times 10^{-6}$  S·cm<sup>-1</sup> (90% r.h.), which are still only low values, but approximately two orders of magnitude higher than those of Pb-MOF. (A brief survey of proton conductivity values in other coordination networks containing sulfonate groups, extracted from literature, is shown in Supporting Information File 1, Table S1) For the non-activated Mg-CP sample, it turns out that a satisfying fit of the Nyquist plot data is

obtained by using a modified equivalent circuit model, as mentioned above. A second semicircle, superimposing the first one, needs to be accounted for, though this is hardly distinguishable by the naked eye. This finding suggests that, in this case, proton conduction occurs by two distinct processes. The second one is irreversibly erased by thermal activation; the additional semicircle is no longer observed and, hence, the standard equivalent circuit model can be applied once the sample has been activated. This is further illustrated in Figure 4, which shows the Bode plots (i.e., impedance  $Z$  and phase angle  $\Phi$  vs frequency  $f$ ) of the measurements from Figure 2. For the non-activated Mg-CP sample, the phase angle shows two distinct features, namely a maximum at ca. 10<sup>2</sup> Hz and a shoulder at ca. 10<sup>5</sup> Hz, corresponding to two distinguishable conduction modes. After thermal activation, only a single broad maximum in the region from 10<sup>3</sup> to 10<sup>4</sup> Hz remains. The phase angle for the Pb-MOF sample shows only one maximum (at ca. 10<sup>2</sup> Hz) both before and after activation. We conclude that the second conductance mode in the non-activated Mg-CP material may be caused by interparticle water adsorbate layers that are successfully and irreversibly removed by activation. These findings are quite helpful, as they allow us to conversely conclude that the remaining mode of proton conductance is probably not caused by such adsorbate layers, but more likely occurs within the crystalline material, as will be elaborated in more detail below. (We did not observe any semicircular behavior in the absence of humidity, neither before nor after thermal activation, from which we conclude that other phenomena, such as relaxation of electric dipoles, do not significantly contribute to the charge mobility.)

Another way to depict the conductivity is to plot the real part of conductivity  $\text{Re}(\sigma)$  vs frequency  $f$  [20], as shown in Figure 5. All samples show reasonably constant values in the frequency

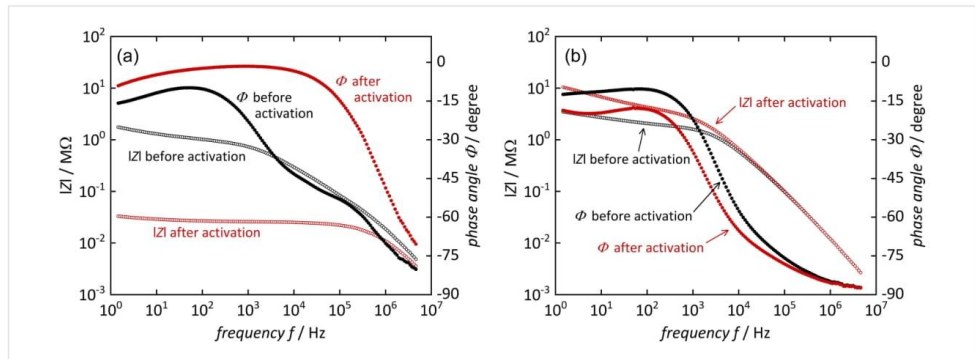


**Figure 4:** Bode plots (absolute value of impedance  $Z$  and phase angle  $\Phi$  vs frequency  $f$ ) of (a)  $[\text{Mg}(\text{H}_2\text{O})_2(\text{H}_3\text{L})]\text{H}_2\text{O}$  and (b)  $[\text{Pb}_2(\text{HL})]\text{H}_2\text{O}$ , before and after thermal activation. Measurements were conducted at 22 °C and 90% r.h.

ranges that correspond to the maximum phase angles from Figure 4. These values are consistent with the conductivity values in Table 1.

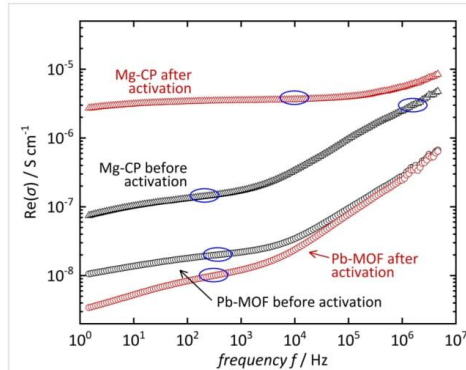


**Figure 5:** Real parts of the conductivity values of  $[\text{Mg}(\text{H}_2\text{O})_2(\text{H}_3\text{L})]\text{H}_2\text{O}$  and  $[\text{Pb}_2(\text{HL})]\text{H}_2\text{O}$  obtained by conversion of impedance into permittivity (22 °C, 90% r.h.). Highlighted regions (blue) correspond to the values obtained from the Nyquist plots (see Table 1).

Finally, we measured the proton conductivity at different temperatures between 22 and 35 °C (at 90% r.h.), as shown in Figure 6a. As expected, both materials show an increase in conductivity with increasing temperature; this applies to samples both before and after thermal activation. The relation between conductivity and temperature can be used to estimate the activation energy  $E_A$  of proton mobility by using the Arrhenius equation (Equation 1), where  $\sigma_0$  is a material-specific factor and  $k_B$  is Boltzmann's constant [22–24]:

Figure 6b exhibits the Arrhenius plots, that is,  $\ln(T\sigma)$  vs  $T^{-1}$ . The activation energy is obtained from the slope ( $-E_A/k_B$ ) of the linear regression; the resulting values are shown in Table 1. For the activated samples, low values ( $\leq 0.4$  eV) are observed, which indicates that proton conduction occurs predominantly by a “hopping” mechanism, that is, by formation and simultaneous cleavage of covalent bonds and hydrogen bonds between adjacent molecules, without mass transport [25]. For bulk liquid water, this is known as the Grotthuß mechanism, with reported activation energy values of 0.10–0.11 eV [26,27]. In the materials studied here, proton hopping can occur between  $\text{H}_2\text{O}/\text{H}_3\text{O}^+$  and/or deprotonated/protonated sulfonate groups ( $-\text{SO}_3^-/-\text{SO}_3\text{H}$ ) within the crystals. Spatial confinement may hinder proton hopping to some extent, which is why activation energies larger than in bulk liquid water are frequently observed in such materials (up to 0.4 eV) [25]. In contrast, when proton conduction occurs by mass transport (i.e., by cation diffusion of, e.g.,  $\text{H}_3\text{O}^+$ ), activation energies higher than 0.4 eV are expected [28]. This mechanism seems to dominate the additional conduction mode in the non-activated Mg-CP sample, where an activation energy of 0.64 eV is observed. This is consistent with our above assumption that this additional conduction occurs within interparticle water adsorbate layers; these liquid-like layers may facilitate molecular diffusion to some extent.

To explain the differences in proton conductivity between the (activated) Mg-CP and Pb-MOF materials, the respective crystal structures need to be considered regarding the chemical

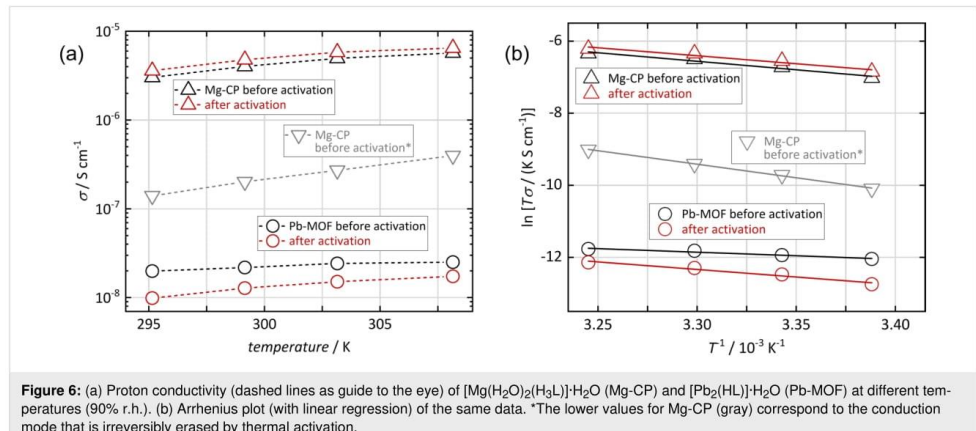


**Figure 6:** (a) Proton conductivity (dashed lines as guide to the eye) of  $[\text{Mg}(\text{H}_2\text{O})_2(\text{H}_3\text{L})]\text{H}_2\text{O}$  (Mg-CP) and  $[\text{Pb}_2(\text{HL})]\text{H}_2\text{O}$  (Pb-MOF) at different temperatures (90% r.h.). (b) Arrhenius plot (with linear regression) of the same data. \*The lower values for Mg-CP (gray) correspond to the conduction mode that is irreversibly erased by thermal activation.

environment of the sulfonate groups and the hydrogen bonding networks of coordinating and non-coordinating water molecules. The Mg-CP network shows a clearly higher proton conductivity than Pb-MOF. As stated above, the sulfonate groups do not coordinate to  $Mg^{2+}$ , but point into the interlayer regions of the layered structure, forming hydrogen bonds, both with coordinating (two per formula unit) and non-coordinating (one per formula unit) water molecules. This extensive hydrogen bonding network offers good conditions for proton hopping from one partner ( $H_3O^+$ ,  $-SO_3H$ ) to another. In the case of the Pb-MOF material, in contrast, no such hydrogen bonding network is present. The sulfonate groups coordinate to  $Pb^{2+}$ , and no hydrogen bonds other than between pairs of non-coordinating water molecules are observed, which explains that long-range proton hopping cannot occur to any significant extent in this network.

## Conclusion

The two coordination networks  $[Mg(H_2O)_2(H_3L)] \cdot H_2O$  (Mg-CP) and  $[Pb_2(HL)] \cdot H_2O$  (Pb-MOF) exhibit significantly different crystal structures, although they contain the same linker molecule,  $(H_2O_3PCH_2)_2-NCH_2-C_6H_4-SO_3H$  (H5L). Mg-CP shows a clearly higher (though altogether low) proton conductivity than Pb-MOF (by two orders of magnitude), which can be explained by said differences in crystal structure. In Mg-CP the sulfonate group does not coordinate to  $Mg^{2+}$  but is available for being part of an extended hydrogen bonding network that also includes coordinating and non-coordinating water molecules. This hydrogen bonding network seems to offer good conditions for a proton “hopping” mechanism, as confirmed by the low activation energy of the proton conductance. In Pb-MOF, on the other hand, no extended hydrogen bonding occurs, as the sulfonate groups coordinate to  $Pb^{2+}$ , without forming hydrogen bonds.

## Experimental

The linker molecule  $(H_2O_3PCH_2)_2-NCH_2-C_6H_4-SO_3H$  (H5L, see Supporting Information File 1, Figure S1) was prepared following a published route [17]. Benzylamine was sulfonated by reaction with oleum in a first step, followed by phosphonomethylation of the amino group using phosphonic acid, formaldehyde, and hydrochloric acid. The synthesis of the compounds  $[Mg(H_2O)_2(H_3L)] \cdot H_2O$  and  $[Pb_2(HL)] \cdot H_2O$  was achieved following published procedures [17]. For  $[Mg(H_2O)_2(H_3L)] \cdot H_2O$ , an aqueous solution of  $MgCl_2$  (6 mmol, 1218 mg in 2 mL  $H_2O$ ) was added to a mixture of the linker molecule (564 mg, 1.5 mmol), 1.5 mL of an aqueous solution of  $NaOH$  ( $c = 2$  mol/L), 6.5 mL water, and 10 mL ethanol in a 30 mL Teflon insert, which was placed into a steel autoclave. For  $[Pb_2(HL)] \cdot H_2O$ ,  $Pb(OAc)_3$  (0.5 mmol, 189 mg in 2 mL  $H_2O$ ) was added to a mixture of the linker molecule

(188 mg, 0.5 mmol), 8 mL water and 10 mL ethanol in a 30 mL Teflon insert, which was placed into a steel autoclave. Both reactors were closed and heated within 6 h to the reaction temperature of 150 °C. After 24 h, the reactors were slowly cooled down to room temperature within 12 h. The compounds were collected via filtration, dried under ambient conditions, and identified by powder X-ray diffraction.  $[Mg(H_2O)_2(H_3L)] \cdot H_2O$  was obtained as colorless needles (240 mg, 36%) and  $[Pb_2(HL)] \cdot H_2O$  as small colorless crystals (152 mg, 38%).

PXRD data at a relative humidity of 90% were recorded on a Panalytical Empyrean diffractometer equipped with a CHC plus+ chamber in a transmittance Bragg–Brentano geometry employing Cu radiation. The patterns were recorded at a temperature of 25 °C before and after the activation of sample at 80 °C and 10% relative humidity. For impedance spectroscopy, samples of the materials were pressed into cylindrical pellets using a weight of 10 t. The pellets had thicknesses of ca. 1.8 mm ( $[Mg(H_2O)_2(H_3L)] \cdot H_2O$ ) and ca. 0.5 mm ( $[Pb_2(HL)] \cdot H_2O$ ), respectively; their external surface area was ca. 130 mm<sup>2</sup>. Impedance measurements were carried out using a Novocontrol broadband dielectric spectrometer (Alpha-A High Performance Frequency Analyzer). The samples were mounted between two Novocontrol BDS1200 based blocking gold-plated electrodes, and two-wire mode measurements were made, as described in earlier studies [21,29]. The impedance data was recorded in the frequency range from 1 Hz to 4.61 MHz at an applied voltage of 0.1 V. Temperature and humidity were controlled by an Espec SH-242 climate chamber. Prior to each measurement, samples were allowed to equilibrate for 24 h.

## Supporting Information

### Supporting Information File 1

Supplementary data.

[<https://www.beilstein-journals.org/bjnano/content/supporting/2190-4286-13-36-S1.pdf>]

## Funding

This research was funded by Deutsche Forschungsgemeinschaft (DFG) within the priority program 1928: Coordination Networks: Building Blocks for Functional Systems, COORNets.

## ORCID® iDs

Ali Javed - <https://orcid.org/0000-0002-9947-0904>

Hana Bunzen - <https://orcid.org/0000-0003-1824-0291>

Michael Tiemann - <https://orcid.org/0000-0003-1711-2722>

## References

- Yan, Y.; Chen, G.; She, P.; Zhong, G.; Yan, W.; Guan, B. Y.; Yamauchi, Y. *Adv. Mater. (Weinheim, Ger.)* **2020**, *32*, 2004654. doi:10.1002/adma.202004654
- Du, M.; Li, Q.; Zhao, Y.; Liu, C.-S.; Pang, H. *Coord. Chem. Rev.* **2020**, *416*, 213341. doi:10.1016/j.ccr.2020.213341
- Meng, X.; Wang, H.-N.; Song, S.-Y.; Zhang, H.-J. *Chem. Soc. Rev.* **2017**, *46*, 464–480. doi:10.1039/c6cs00528d
- Breitwieser, M.; Klingele, M.; Vierrath, S.; Zengerle, R.; Thiele, S. *Adv. Energy Mater.* **2018**, *8*, 1701257. doi:10.1002/aenm.201701257
- Wei, M.-J.; Fu, J.-Q.; Wang, Y.-D.; Zhang, Y.; Zang, H.-Y.; Shao, K.-Z.; Li, Y.-G.; Su, Z.-M. *CrystEngComm* **2017**, *19*, 7050–7056. doi:10.1039/c7ce01589e
- Xie, X.-X.; Yang, Y.-C.; Dou, B.-H.; Li, Z.-F.; Li, G. *Coord. Chem. Rev.* **2020**, *403*, 213100. doi:10.1016/j.ccr.2019.213100
- Liu, R.; Wang, D.-Y.; Shi, J.-R.; Li, G. *Coord. Chem. Rev.* **2021**, *431*, 213747. doi:10.1016/j.ccr.2020.213747
- Hamrock, S. J.; Yandrasits, M. A. *Polym. Rev. (Philadelphia, PA, U. S.)* **2006**, *46*, 219–244. doi:10.1080/15583720600796474
- Kang, D. W.; Kang, M.; Hong, C. S. J. *Mater. Chem. A* **2020**, *8*, 7474–7494. doi:10.1039/d0ta01733g
- Jhariat, P.; Kumari, P.; Panda, T. *CrystEngComm* **2020**, *22*, 6425–6443. doi:10.1039/d0ce00902d
- Fang, M.; Montoro, C.; Semsarilar, M. *Membranes* **2020**, *10*, 107. doi:10.3390/membranes10050107
- Batten, S. R.; Champness, N. R.; Chen, X.-M.; Garcia-Martinez, J.; Kitagawa, S.; Öhrström, L.; O’Keeffe, M.; Paik Suh, M.; Reedijk, J. *Pure Appl. Chem.* **2013**, *85*, 1715–1724. doi:10.1351/pac-rec-12-11-20
- Li, W.-H.; Deng, W.-H.; Wang, G.-E.; Xu, G. *EnergyChem* **2020**, *2*, 100029. doi:10.1016/j.enchem.2020.100029
- Kolokolov, D. I.; Lim, D.-W.; Kitagawa, H. *Chem. Rec.* **2020**, *20*, 1297–1313. doi:10.1002/tcr.202000072
- Bao, S.-S.; Shimizu, G. K. H.; Zheng, L.-M. *Coord. Chem. Rev.* **2019**, *378*, 577–594. doi:10.1016/j.ccr.2017.11.029
- Zhou, C.-C.; Yan, H.; Liu, H.-T.; Li, R.-Y.; Lu, J.; Wang, S.-N.; Li, Y.-W. *New J. Chem.* **2020**, *44*, 17821–17830. doi:10.1039/d0nj04179c
- Wöhlbrandt, S.; Iglesias, A.; Svensson Grape, E.; Øien-Ødegaard, S.; Ken Inge, A.; Stock, N. *Dalton Trans.* **2020**, *49*, 2724–2733. doi:10.1039/c9dt04571f
- Cheetham, A. K.; Rao, C. N. R.; Feller, R. K. *Chem. Commun.* **2006**, 4780–4785. doi:10.1039/b610264f
- Sorrentino, A.; Sundmacher, K.; Vidakovic-Koch, T. *Energies (Basel, Switz.)* **2020**, *13*, 5825. doi:10.3390/en13215825
- Escorihuela, J.; Narducci, R.; Compañ, V.; Costantino, F. *Adv. Mater. Interfaces* **2018**, *6*, 1801146. doi:10.1002/admi.201801146
- Wortmann, M.; Frese, N.; Mamun, A.; Trabelsi, M.; Keil, W.; Büker, B.; Javed, A.; Tiemann, M.; Moritzer, E.; Ehrmann, A.; Hüttner, A.; Schmidt, C.; Götzhäuser, A.; Hüsgen, B.; Sabantina, L. *Nanomaterials* **2020**, *10*, 1210. doi:10.3390/nano10061210
- Javed, A.; Strauss, I.; Bunzen, H.; Caro, J.; Tiemann, M. *Nanomaterials* **2020**, *10*, 1263. doi:10.3390/nano10071263
- Javed, A.; Wagner, T.; Wöhlbrandt, S.; Stock, N.; Tiemann, M. *ChemPhysChem* **2020**, *21*, 605–609. doi:10.1002/cphc.202000102
- Ramaswamy, P.; Wong, N. E.; Shimizu, G. K. H. *Chem. Soc. Rev.* **2014**, *43*, 5913–5932. doi:10.1039/c4cs00093e
- Yoon, M.; Suh, K.; Natarajan, S.; Kim, K. *Angew. Chem., Int. Ed.* **2013**, *52*, 2688–2700. doi:10.1002/anie.201206410
- Loewenstein, A.; Szoke, A. *J. Am. Chem. Soc.* **1962**, *84*, 1151–1154. doi:10.1021/ja00866a018
- Luz, Z.; Meiboom, S. *J. Am. Chem. Soc.* **1964**, *86*, 4768–4769. doi:10.1021/ja01076a008
- Kreuer, K.-D.; Rabenau, A.; Weppner, W. *Angew. Chem., Int. Ed. Engl.* **1982**, *21*, 208–209. doi:10.1002/anie.198202082
- Steinke, F.; Javed, A.; Wöhlbrandt, S.; Tiemann, M.; Stock, N. *Dalton Trans.* **2021**, *50*, 13572–13579. doi:10.1039/d1dt02610k

## License and Terms

This is an open access article licensed under the terms of the Beilstein-Institut Open Access License Agreement (<https://www.beilstein-journals.org/bjnano/terms>), which is identical to the Creative Commons Attribution 4.0 International License

(<https://creativecommons.org/licenses/by/4.0/>). The reuse of material under this license requires that the author(s), source and license are credited. Third-party material in this article could be subject to other licenses (typically indicated in the credit line), and in this case, users are required to obtain permission from the license holder to reuse the material.

The definitive version of this article is the electronic one which can be found at:

<https://doi.org/10.3762/bjnano.13.36>



## Supporting Information

for

### **The role of sulfonate groups and hydrogen bonding in the proton conductivity of two coordination networks**

Ali Javed, Felix Steinke, Stephan Wöhlbrandt, Hana Bunzen, Norbert Stock  
and Michael Tiemann

*Beilstein J. Nanotechnol.* **2022**, 13, 437–443. doi:10.3762/bjnano.13.36

## Supplementary data

License and Terms: This is a supporting information file under the terms of the Creative Commons Attribution License (<https://creativecommons.org/licenses/by/4.0>). Please note that the reuse, redistribution and reproduction in particular requires that the author(s) and source are credited and that individual graphics may be subject to special legal provisions.  
The license is subject to the *Beilstein Journal of Nanotechnology* terms and conditions: (<https://www.beilstein-journals.org/bjnano/terms>)

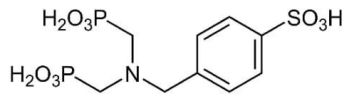


**Figure S1:** Linker molecule  $(H_2O_3PCH_2)_2-NCH_2-C_6H_4-SO_3H$  ( $H_5L$ )

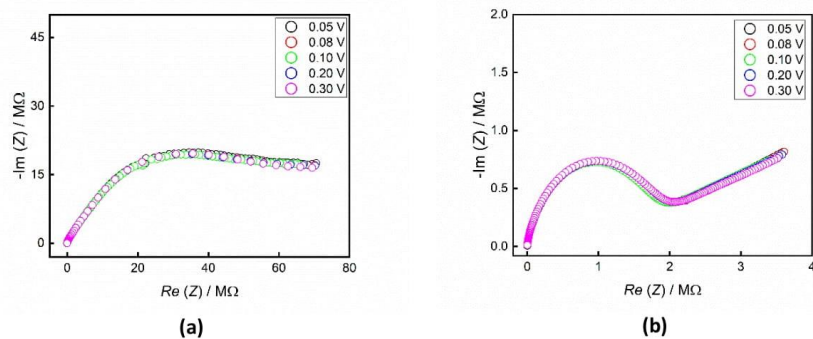


**Figure S2:** Exemplary Nyquist plots at various applied potentials for (a)  $[Mg(H_2O)_2(H_3L)] \cdot H_2O$  ( $22^\circ C$ , 70% r.h.) and (b)  $[Pb_2(HL)] \cdot H_2O$  ( $22^\circ C$ , 90% r.h.).

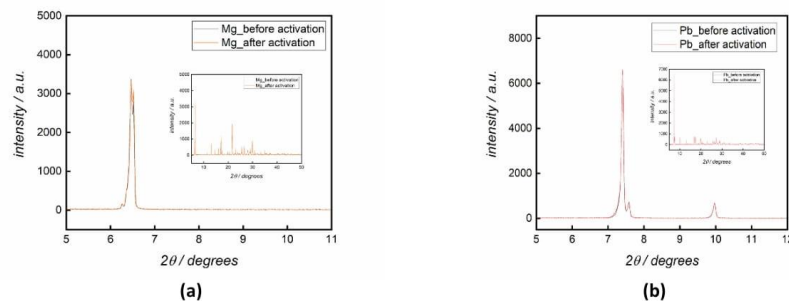


**Figure S3:** Powder XRD patterns of (a)  $[Mg(H_2O)_2(H_3L)] \cdot H_2O$  and (b)  $[Pb_2(HL)] \cdot H_2O$ . All measurements were performed at  $25^\circ C$  and 90% relative humidity (r.h.). No significant change is observed after activation of the samples (i.e., exposure to  $80^\circ C$  for 24 h).

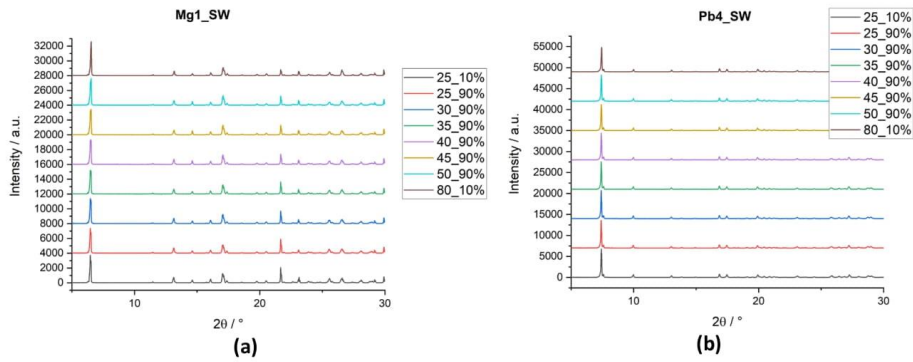


**Figure S4:** Powder XRD patterns of (a)  $[\text{Mg}(\text{H}_2\text{O})_2(\text{H}_3\text{L})]\cdot\text{H}_2\text{O}$  and (b)  $[\text{Pb}_2(\text{HL})]\cdot\text{H}_2\text{O}$  at variable temperature and humidity.

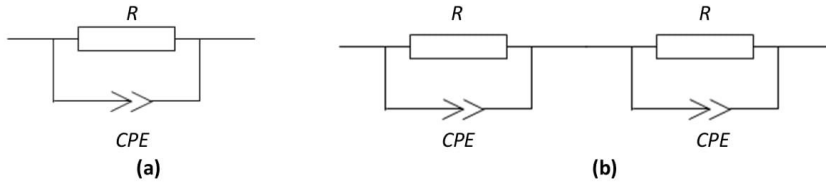


**Figure S5:** Equivalent circuit models used: (a) Activated  $[\text{Mg}(\text{H}_2\text{O})_2(\text{H}_3\text{L})]\cdot\text{H}_2\text{O}$  and for activated/non-activated  $[\text{Pb}_2(\text{HL})]\cdot\text{H}_2\text{O}$ , (b) non-activated  $[\text{Mg}(\text{H}_2\text{O})_2(\text{H}_3\text{L})]\cdot\text{H}_2\text{O}$ .

**Table S1:** Some proton-conducting coordination networks containing sulfonate groups [1,2]

sample name	conditions	$\sigma$ (S/cm)	$E_A$ (eV)
$\{[\text{Zn}(\text{bpeH})(5\text{-sip})(\text{H}_2\text{O})]\cdot(\text{H}_2\text{O})\}_n$	65 °C, 95% r.h.	$2.5 \times 10^{-6}$	0.54
$\{[\text{Cu}(\text{pyz})(5\text{-Hsip})(\text{H}_2\text{O})_2\}(\text{H}_2\text{O})_2\}_n$	65 °C, 95% r.h.	$3.5 \times 10^{-5}$	0.35
$\{[\text{Cu}(\text{bpee})_{0.5}(5\text{-sip})(\text{H}_2\text{O})_2\}(\text{H}_2\text{O})_4(\text{bpeeH}_2)_{0.5}\}_n$	65 °C, 95% r.h.	$9.9 \times 10^{-8}$	0.40
$\{[\text{Cu}(\text{bpy})(5\text{-Hsip})(\text{H}_2\text{O})]\cdot(\text{H}_2\text{O})_2\}_n$	65 °C, 95% r.h.	$5.8 \times 10^{-6}$	0.43
$\{[\text{Cu}(\text{bpy})_2(5\text{-H}_2\text{sip})_2]\cdot(\text{H}_2\text{O})_6\}_n$	65 °C, 95% r.h.	$1.4 \times 10^{-6}$	0.45
$\{[\text{Cu}_2(\text{sba})_2(\text{bpg})_2(\text{H}_2\text{O})\}_5\text{H}_2\text{O}\}_n$	80 °C, 95% r.h.	$9.4 \times 10^{-3}$	0.64
$\text{Cu}_4(5\text{-sip})_2(\text{OH})_2(\text{DMF})_2$	95 °C, 95% r.h.	$7.4 \times 10^{-4}$	1.32
$\text{UiO-66}(\text{SO}_3\text{H})_2$	80 °C, 90% r.h.	$8.4 \times 10^{-2}$	0.32
MIL-101-SO <sub>3</sub> H	70 °C, 90% r.h.	$4.3 \times 10^{-5}$	0.27

## References

1. Liu, R.; Wang, D.-Y.; Shi, J.-R.; Li, G. *Coord. Chem. Rev.* **2021**, *431*, 213747. doi:10.1016/j.ccr.2020.213747
2. Lim, D.-W.; Kitagawa, H. *Chem. Rev.* **2020**, *120*, 8416. doi:10.1021/acs.chemrev.9b00842

### 5.3.3 Published Data Details

#### 5.3.3.1 Fittings Parameters and Proton Conductivity

Table 5.3.1. An overview of fittings produced using equivalent circuit models for compounds Mg-CP and Pb-MOF, as well as calculations of proton conductivities at multiple temperatures and relative humidity setpoints.

sample name	T [°C]	rh [%]	chi-sqr.	n	Q	R [Ω]	σ [S/cm]	(n)*	(Q)*	(R)* [Ω]	(σ)* [S/cm]
Mg-CP (before activation)	22	70	0.019	0.94	2.63E-11	2.27E6	6.00E-8	0.83	1.89E-10	4.95E7	2.73E-9
		75	0.014	0.94	3.03E-11	9.69E5	1.39E-7	0.81	2.48E-10	1.98E7	6.81E-9
		80	0.008	0.93	3.71E-11	3.63E5	3.73E-7	0.80	3.19E-10	6.56E6	2.06E-8
		85	0.005	0.92	4.51E-11	1.32E5	1.02E-6	0.77	4.99E-10	2.39E6	5.66E-8
		90	0.005	0.94	4.80E-11	4.48E4	3.00E-6	0.73	1.01E-9	9.68E5	1.40E-7
		26	90	0.004	0.94	4.71E-11	3.37E4	4.02E-6	0.72	1.11E-9	6.71E5
Mg-CP (after activation)	26	90	0.004	0.96	3.87E-11	2.73E4	4.95E-6	0.73	1.07E-9	5.00E5	2.70E-7
	30	90	0.003	0.98	2.72E-11	2.37E4	5.71E-6	0.74	8.6E-10	3.42E5	3.96E-7
	35	90	0.002	0.81	2.50E-10	1.55E4	6.49E-6	-	-	-	-
	22	90	0.005	0.82	1.55E-10	3.72E4	3.60E-6	-	-	-	-
Pb-MOF (before activation)	26	90	0.004	0.82	1.93E-10	2.51E4	4.78E-6	-	-	-	-
	30	90	0.004	0.82	2.40E-10	1.88E4	5.80E-6	-	-	-	-
	35	90	0.002	0.81	2.50E-10	1.55E4	6.49E-6	-	-	-	-
	22	80	0.128	0.80	1.30E-10	7.61E7	4.94E-10	-	-	-	-
		75	0.236	0.78	2.58E-10	3.17E7	1.18E-9	-	-	-	-
		85	0.015	0.86	9.80E-11	3.98E6	9.44E-9	-	-	-	-
Pb-MOF (after activation)	26	90	0.010	0.85	1.22E-10	1.72E6	2.18E-8	-	-	-	-
	30	90	0.010	0.90	1.33E-10	1.55E6	2.42E-8	-	-	-	-
	35	90	0.011	0.84	1.39E-10	1.50E6	2.51E-8	-	-	-	-
	22	90	0.015	0.85	1.12E-10	3.81E6	9.90E-9	-	-	-	-
	26	90	0.012	0.85	1.17E-10	2.94E6	1.27E-8	-	-	-	-
	30	90	0.010	0.85	1.17E-10	2.49E6	1.50E-8	-	-	-	-
Pb-MOF (before activation)	35	90	0.015	0.86	1.04E-10	2.17E6	1.73E-8	-	-	-	-

where,  $(R)^*$  corresponds to resistance and  $(\sigma)^*$  denotes the computed proton conductivity of second conduction mode that was appeared at low frequency region solely for Mg-CP, which was erased irreversibly by thermal activation.

### 5.3.3.2 Nyquist Plots for Mg-CP

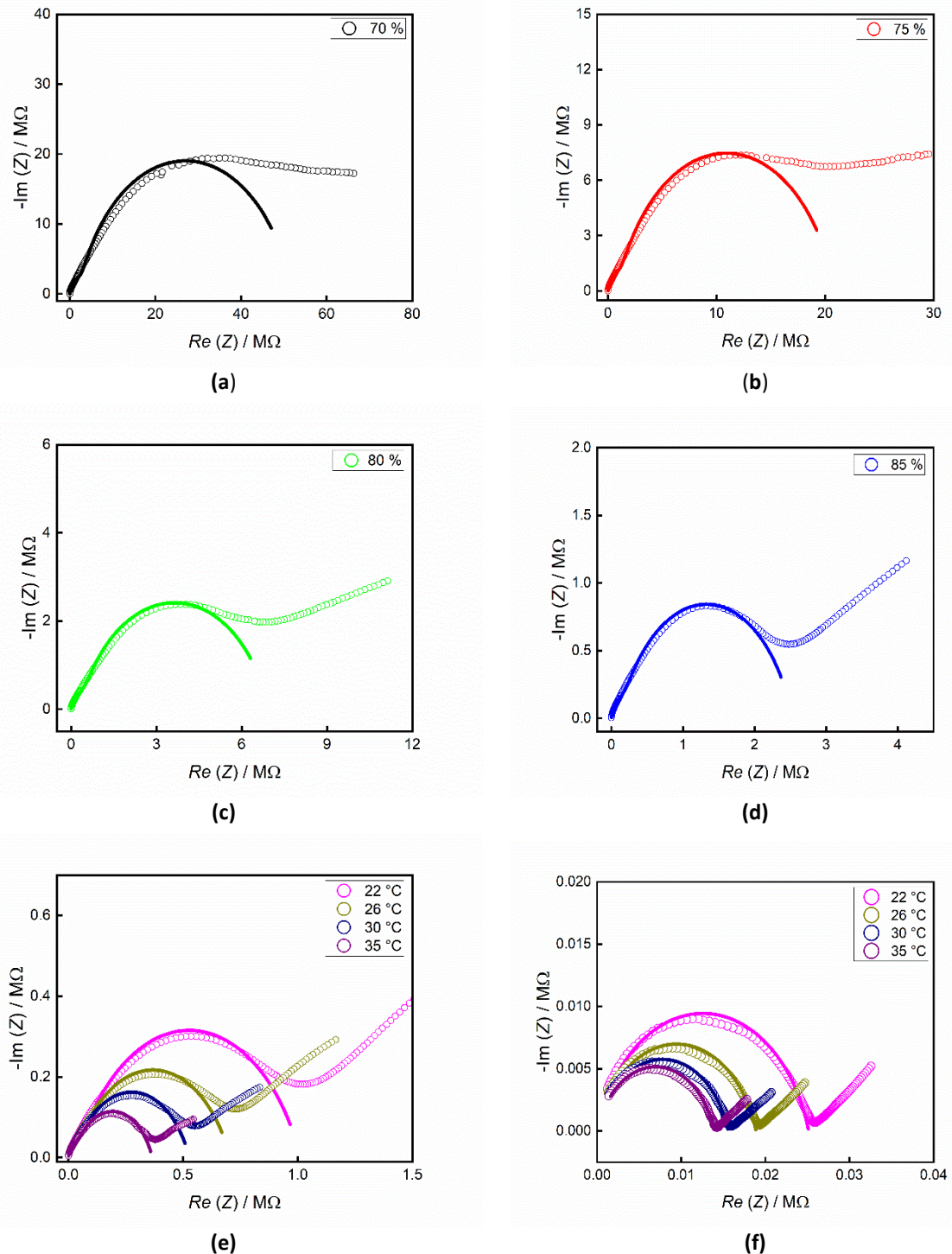
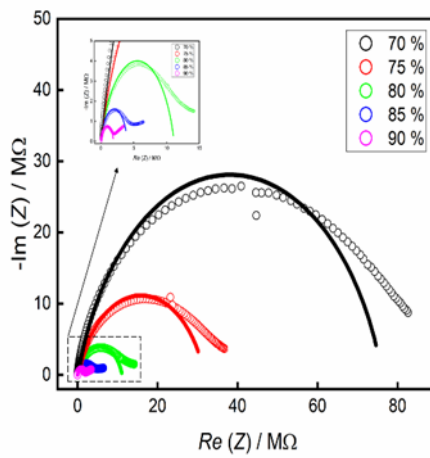
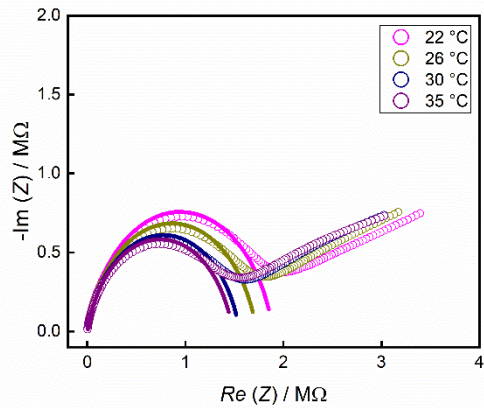


Figure 5.3.1. Nyquist plots for compound Mg-CP before and after thermal activation of sample at (a) 22 °C and 70 % rh (b) 22 °C and 75 % rh (c) 22 °C and 80 % rh (d) 22 °C and 85 % rh (e) 90 % rh and 22 °C ... 35 °C before thermal activation (f) 90 % rh and 22 °C ... 35 °C after thermal activation.

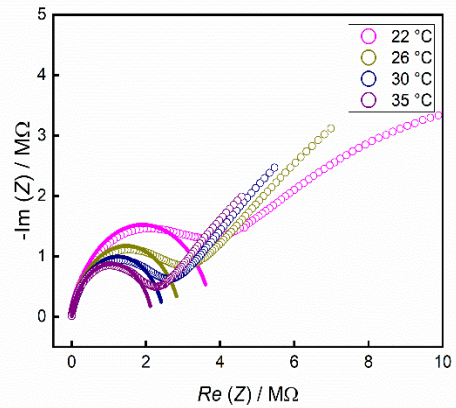
### 5.3.3.3 Nyquist Plots for Pb-MOF



(a)



(b)



(c)

Figure 5.3.2. Nyquist plots for compound Pb-MOF before and after thermal activation of sample at (a) 22 °C and 70 % ... 90 % rh before activation (b) 90 % rh and 22 °C ... 35 °C before thermal activation (c) 90 % rh and 22 °C ... 35 °C after thermal activation.

## 5.4 Studies on a Fringing Electric Field Sensor (Unpublished)

In addition to the studies presented in sections 5.1-5.3, further (unpublished) work was dedicated to the fabrication of a fringing electric field (FEF) sensor. The purpose of this sensor is the *in-situ* investigation of proton exchange membranes (PEMs) with respect to relative humidity and proton conduction. The sensor design comprises concentric, planar ring electrodes that create an electric field in any material placed on top of it (such as the PEM), as depicted in Figure 5.4.1. The field can be modulated for impedance measurements.

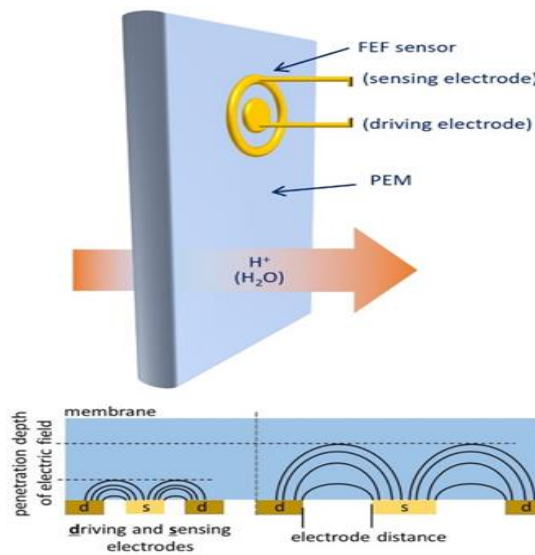


Figure 5.4.1: Conception of a fringing electric field (FEF) sensor.

To gain insight into the sensitivity of an in-plane probe, simulation was performed with the help of Finite Element Method Magnetics (FEMM) software. Figure 5.4.2 shows the voltage density and direction of electric field lines. The potential of 1 V was applied at the middle ring which originated the electric field lines. These potential lines terminate at the outer ring. It can be seen in Figure 5.4.2(a) that these lines pass through and below the printed circuit board (PCB). These are in fact undesirable electric field lines whose contribution can be reduced by using a grounded backplane as shown in Figure 5.4.2(b). The backplane blocks those lines which reach the outer ring below the PCB. Moreover, one more ring is introduced in between the higher potential and lower potential electrodes named as guard electrode. This electrode is also grounded, which acts as an obstruction for the direct path of field lines. This effect is exhibited in Figure 5.4.2(c). The color change in the pictures represents the voltage density where we can see that near the electrodes the potential is high and with the increase in distance it reduces.

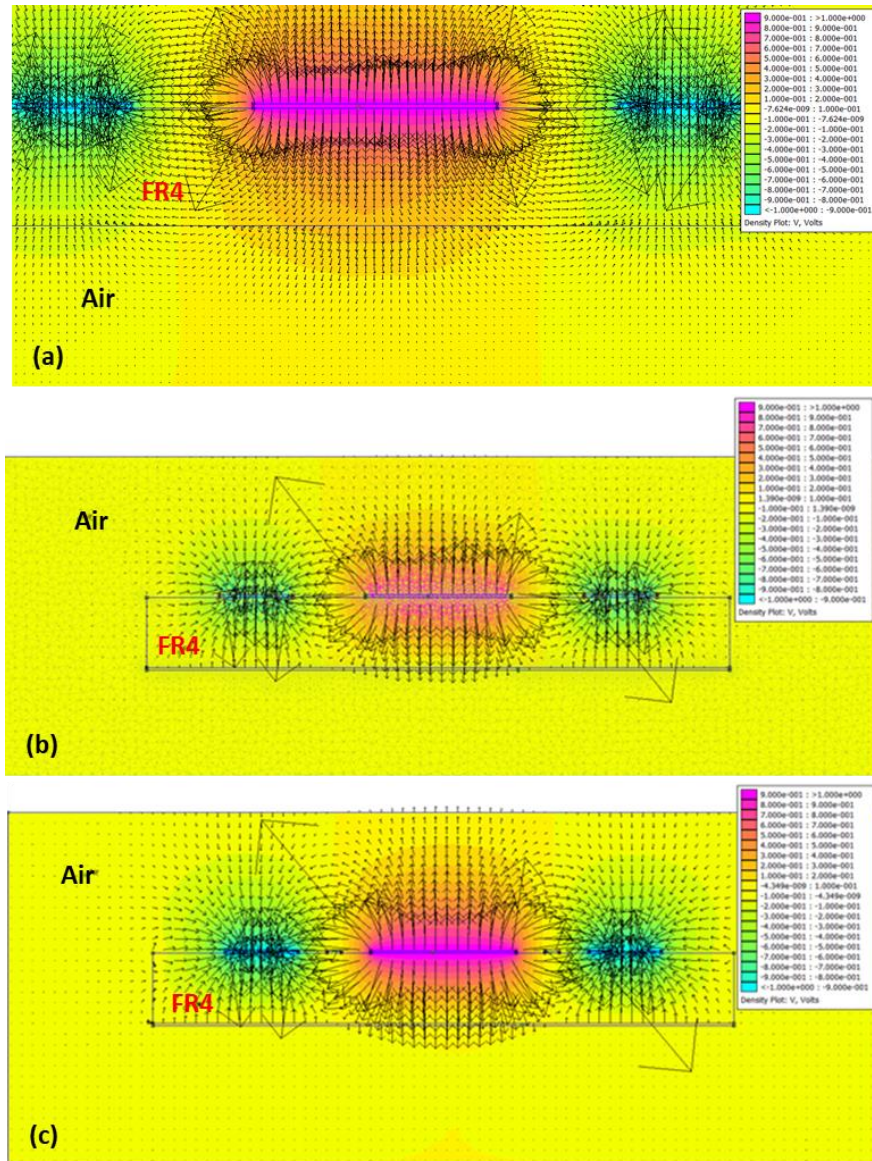


Figure 5.4.2: Simulation results of probe (a) without backplane (b) with backplane (c) with backplane and additional guard ring between electrodes. The simulation is done with empty probe in the presence of air as an environment.

FEF sensors were developed in four different layouts, as shown in Figure 5.4.3. The electrodes were printed on non-conducting FR4 epoxy laminate substrates of 1 mm thickness ('circuit board' design). They consist of copper (thickness: 35  $\mu\text{m}$ ), covered with layers of nickel (3-6  $\mu\text{m}$ ) and gold (0.05-0.1  $\mu\text{m}$ ). The inner and outer diameter of the outer ring electrode (and, thus, the inter-electrode distance) were varied (layouts 1-3). Either of the two electrodes can be used as the driving or as the sensing electrode. In addition, a third, grounded ring was placed between the driving and sensing electrodes in layout 4, to block the direct path of electric field lines. The rear sides of the FR4 boards are grounded to shield the electric field in the opposite direction.

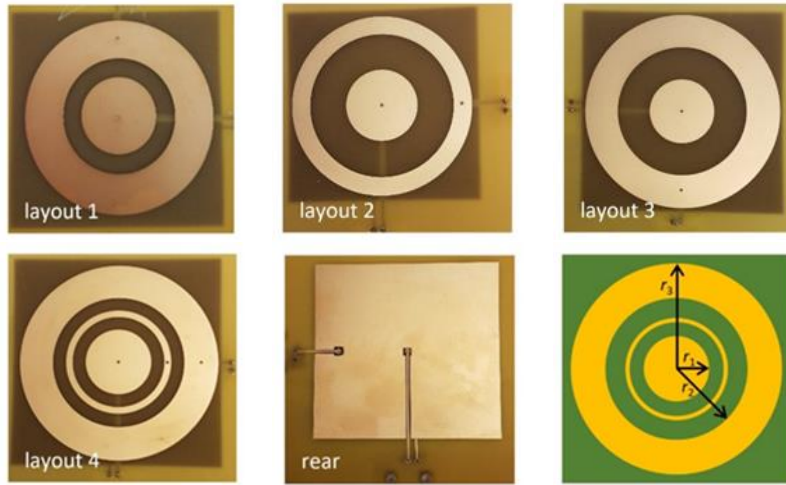


Figure 5.4.3: Photographs of layouts of FEF sensors.

As a first test of feasibility, the capacitance of dry air, teflon, and deionized water was recorded at variable alternating voltage frequency, as shown in Figure 5.4.4 for the sensor with layout 1. As expected, the capacitance is low and nearly frequency-independent for air and Teflon and increases drastically at low frequencies in case of water. Table 5.4.1 compares the results for the sensors with different layouts. Lower capacitance values are measured with sensors that possess larger inter-electrode distances and, in particular, with the sensor that features the above-mentioned grounded ring between the electrodes. Using Teflon as a reference material of known relative permittivity  $\epsilon_r$  ( $\epsilon_{r(Teflon)} = 2.1$ ),<sup>[100,101]</sup> we can determine the so-called empty electrode capacity constant  $C_e$ , which, in turn, allows for calculation of the relative permittivity of the substrate material,  $\epsilon_{r(sub)}$ . The respective values are shown in Table 5.4.1. The value obtained with the sensor of layout 4 is the closest to the literature value for the FR4 epoxy resin ( $\epsilon_{r(FR4)} = 4.6$ )<sup>[102]</sup>, which is why this sensor was used in further studies.

Table 5.4.1: Dimensions of layouts, empty electrode capacity constant  $C_e$  and permittivity  $\epsilon_{r(sub)}$  of the substrate material of the FEF sensor, calculated from measured capacitances.

layout	dimensions / mm			capacitance* / pF			$C_e$ / pF	$\epsilon_{r(sub)}$
	$r_1$	$r_2$	$r_3$	dry air	teflon	water		
1	10	15	25	0.616	0.852	4.488	0.215	1.90
2	10	20	25	0.316	0.423	0.704	0.097	2.30
3	10	20	30	0.485	0.608	0.735	0.112	3.38
4	10	20	30	0.504	0.621	0.699	0.106	3.85

where, \* stands for capacitance at 0.133 MHz

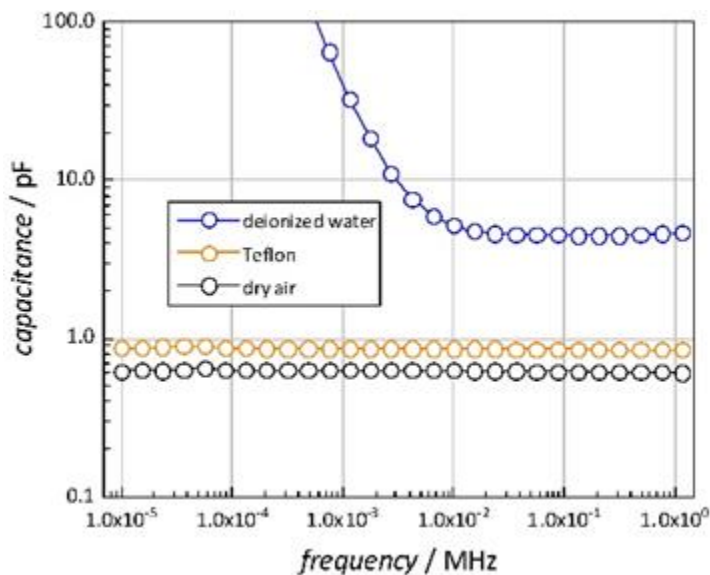


Figure 5.4.4: Capacitance values of pure water, Teflon, and dry air, measured with the FEF sensor.

The FEF probe (layout 4) was then used to characterize proton exchange membranes (PEMs) developed at the University of Oldenburg (group of Prof. Dr. Wark) within this project. They are composed of proton conducting coordination polymers in a PVDF/PVP (2:8) matrix. The respective membrane was placed on the sensor in a humidified (*i.e.* mechanically flexible) state, as shown in Figure 5.4.5. The humidity of the gas atmosphere was subsequently equilibrated at defined level. Figure 5.4.6 shows an example impedance spectrum (Nyquist plot) of a membrane containing the coordination polymer Ca-Etidronate,<sup>[103]</sup> ( $[\text{KCa}(\text{HO}_3\text{PC(OH)(CH}_3\text{-PO}_3\text{)}(\text{H}_2\text{O})]\cdot\text{H}_2\text{O}$ ), measured at 23 °C and 90 % relative humidity. A fit of the indicated equivalent circuit to the high-frequency part of the plot results in a proton conductivity of  $1.32 \times 10^{-9} \text{ S cm}^{-1}$ .

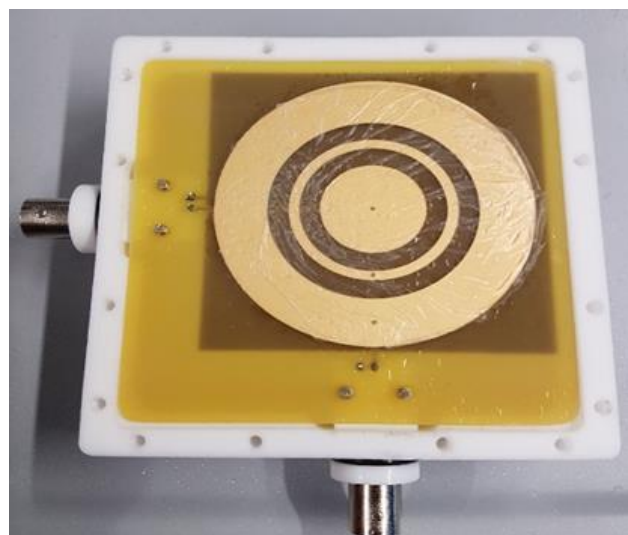


Figure 5.4.5: Mixed matrix membrane placed on the FEF probe.

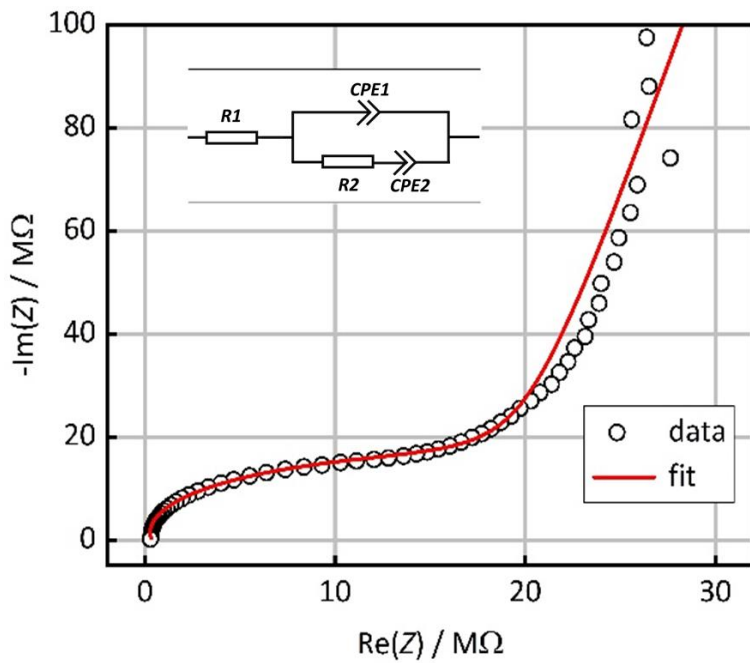


Figure 5.4.6: Impedance of the membrane (Nyquist plot; 23 °C, 90 % rh, 11 Hz - 1 MHz, 0.5 V).

The further impedance measurements of the membrane with the FEF probe were carried out at different relative humidities between 80 % and 95 %, as well as at variable temperature (23 °C and 30 °C). After each change in humidity, the membrane was allowed to equilibrate for 12 hours. Unfortunately, a significant humidity dependence is observed with this membrane (see Figure 5.4.7); future work will aim at developing membranes that are more moisture independent.

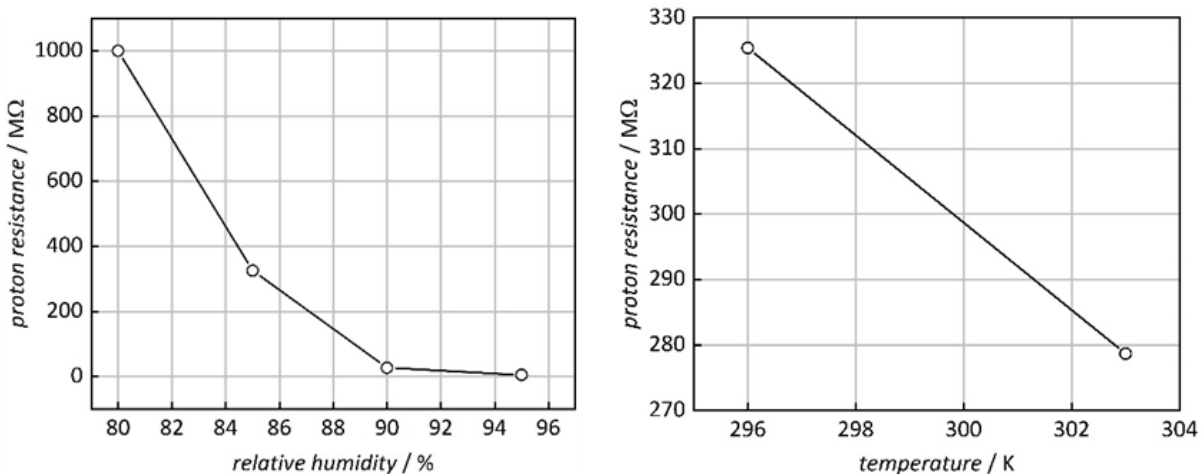


Figure 5.4.7: Proton resistance of the membrane at variable relative humidity and temperature.

## Chapter 6: Synopsis of Thesis

### 6.1 Summary of Findings

In this research work, the proton conductivity of coordination polymers (CPs) and metal-organic frameworks (MOFs) was successfully studied by impedance measurements. These materials stated moderate to low conductivity because of their large resistance ( $10^4 \Omega$  to  $10^9 \Omega$ ). As a result, contact resistance was excluded, and the two-wire mode for impedance measurements was preferred. A noteworthy achievement is the establishment of effective electrical contact between the sample and the electrodes without the use of additives.

The compounds of composition  $[\text{Ba}(\text{H}_3\text{L})(\text{H}_2\text{O})]\cdot\text{H}_2\text{O}$  (**Ba-CP**), Co-MOF-74 (**Co-MOF**),  $[\text{Mg}(\text{H}_2\text{O})_2(\text{H}_3\text{L})]\cdot\text{H}_2\text{O}$  (**Mg-CP**), and  $[\text{Pb}_2(\text{HL})]\cdot\text{H}_2\text{O}$  (**Pb-MOF**) were investigated in this regard. The same linker molecule, (4-[bis(phosphonomethyl)amino]methyl benzene-sulfonic acid), was used to synthesize Ba-CP, Mg-CP, and Pb-MOF, where the large size of Ba-CP enabled us to measure impedance of a single crystal on an in-plane arrangement of interdigitated electrodes. Mg-CP and Pb-MOF were measured in through-plane configuration using pressed pellets. Also, the proton conductivity of Co-MOF was determined in a single crystal form.

The impedance measurements were conducted under several conditions, including variations in relative humidity (rh) and temperature. Moreover, change in orientation was an additional parameter to examine anisotropy in single crystal measurements. The rh was controlled up to a maximum of 90 % to eliminate the contribution of condensed water inside the system, which offered better understanding of proton conduction mechanism. Figure 6 in section 5.2.2 clearly describes a massive rise in proton conductivity at 95 % rh.

The experimental impedance data was represented using a Nyquist plot, with a depressed semicircle in the high frequency range, and a tail in the low frequency domain. A semicircle denotes proton resistance, while a tail indicates proton blockage at the interface between the electrode and the sample. The resistance of the semicircle was determined by fitting it with an equivalent circuit model (ECM). Essentially, the model consists of a parallel combination of an ohmic resistor ( $R$ ) and a constant phase element (CPE), which delivers a fitting whose x-intercept with  $\text{Re}(Z)$  at low frequencies confers us the protons' resistance.

According to Table 3.3, the parameter  $Q$  and the shape of the semicircle are defined by the exponent  $n$ . Fitting results mentioned in Tables 5.1.1, 5.2.1, and 5.3.1 indicate that  $n$  lies

between 0.7 and 1.0, and  $Q$  is between  $10^{-10}$  and  $10^{-12}$ , implying that the samples between two electrodes function as a capacitor with a depressed profile. For this reason, a *CPE* was used instead of a capacitor in ECM.

At 22 °C and 90 % rh, the proton conductivities for Ba-CP are  $1.14 \times 10^{-4}$  S cm<sup>-1</sup> and  $1.17 \times 10^{-5}$  S cm<sup>-1</sup> for c-axis (along length of crystal) and orthogonal direction, respectively. This conductivity is anisotropic, with a difference of around one order of magnitude. The higher conductivity corresponds to the axis which exhibits channels inside the crystal. This demonstrates that protons conduct inside the crystal lattice, and it is an inherent property. After that, the proton conductivity of Co-MOF was measured in the same environment. It is worth noting that the above-mentioned results in two different orientations were attained with single crystals of this compound at 25 °C and 92 % rh. Under the condition of 21 °C and 90% rh, the conductivities in both directions are  $2.04 \times 10^{-5}$  S cm<sup>-1</sup> and  $8.62 \times 10^{-7}$  S cm<sup>-1</sup>, respectively. This indicates anisotropy of more than one order of magnitude and, as expected, lower conductivity. Furthermore, a 1°C increase in temperature along the c-axis increased conductivity to  $3.44 \times 10^{-5}$  S cm<sup>-1</sup>. Consequently, the c-axis, which contains the adsorbed water molecules inside the micropores, shows a higher conductivity. Both materials, in comparison, conducted protons at a moderate level and with anisotropic behavior. In contrast to Co-MOF, Ba-CP is a better proton conductor because it contains non-coordinated water molecules, and sulfonate group inside the channels. Sulfonate groups inside the channels enhance its surface hydrophilicity. As well as that, it facilitates H-bonding network formation by providing proton donors. This leads to an increase in proton conductivity.

Furthermore, the proton conductivity of Mg-CP and Pb-MOF materials as pressed pellets was recorded to be below moderate ( $3.0 \times 10^{-6}$  S cm<sup>-1</sup>) and low ( $2.0 \times 10^{-8}$  S cm<sup>-1</sup>), respectively, at 22 °C and 90% rh. This clearly demonstrates two orders of magnitude change, which corresponds to the presence of the free sulfonate group into the interlayer regions of layered structure of Mg-CP. An additional semicircle was observed as a grain boundary effect in Mg-CP, which was overlapped by a high frequency semicircle. Then both samples were thermally activated at 80 °C for 24 hours to explore the role of non-coordinated water, and the measurements were repeated later under the same conditions. Pb-MOF activation resulted in a slight change in conductivity ( $9.9 \times 10^{-9}$  S cm<sup>-1</sup>), indicating reversible water uptake. Water-sorption measurements revealed the same response. The activation of Mg-CP eliminated the

grain boundary effect, resulting in a conductivity of  $3.6 \times 10^{-6} \text{ S cm}^{-1}$ . By comparison, the anisotropy in proton conductivity was reported in single crystals testing, and powder samples exhibited lower conductivity than them, which could be attributed to stochastic distribution of crystals inside the pressed pellets. Thus, preferred pathway for protons to conduct inside the crystal structure is along the direction of H-bond extension.

To elucidate the influence of humidity on conductivity, the relative humidity was modulated at a fixed temperature, and plotted the data points on a logarithmic scale. According to the experimental data of Ba-CP, conductivity along the direction of channels measured at 22 °C and 70 % rh was  $1.56 \times 10^{-6} \text{ S cm}^{-1}$ . An exponential increase in conductivity was observed as the rh was increased, indicating a linear behavior on a logarithmic scale (see Figure 7 in section 5.1.2). As the rh approached 90%, this number increased by a factor of about 100. Furthermore, in the orthogonal direction at 22 °C and 75 % rh,  $1.11 \times 10^{-7} \text{ S cm}^{-1}$  conductivity was determined. And at 90 % rh, this figure also multiplied by a factor of about 100. In short, conductivity was found to be strongly mediated by humidity. In addition to that, it validated anisotropy at various setpoints of rh, with higher values along the c-axis.

Co-MOF was examined when the humidity was increased at two different fixed temperatures.  $7.32 \times 10^{-7} \text{ S cm}^{-1}$  conductivity was quantified at 21 °C and 75 % rh. As rh encountered 90 %, this value surged around two orders of magnitude.  $1.18 \times 10^{-6} \text{ S cm}^{-1}$  conductivity was valued at 30 °C and 75 % rh. At 90 % rh, a conductivity increase of around two orders of magnitude was marked once more. In short, high conductivity was obtained at high rh and, more precisely, at high temperature (here 30 °C, see Figure 6 in section 5.2.2).

Mb-CP showed a significantly large value of conductivity ( $6.00 \times 10^{-8} \text{ S cm}^{-1}$ ) than Pb-MOF ( $4.94 \times 10^{-10} \text{ S cm}^{-1}$ ) at 22 °C and 70 % rh. Upon the exposure to high humidity levels (here 90 % rh), both materials revealed strong increase in conductivity (approximately two orders of magnitude). Nonetheless, Pb-MOF had a poor conductivity, while Mg-CP had a moderate proton conductivity.

To summarize, the adsorption of water molecules by rh plays a crucial part in the proton conduction. More water molecules adsorbed can create prevalent hydrogen bonded networks to build proton conducting routes, as seen by an exponential rise in conductivity when humidity increased. This shows that water contents in the conduction channel play a vital role in proton transport.

A temperature dependent proton conductivity study was also conducted for all samples under 90% rh. The increase in temperature boosted proton mobility, which provided insight into the proton conduction mechanism. Using equation 2.10, activation energy ( $E_A$ ) was calculated via linear regression on the Arrhenius plot.

For Ba-CP single crystal (see Figure 8 in section 5.1.2),  $E_A$  is 0.31 eV along the c-axis (22-35) °C, and 0.54 eV in orthogonal direction to c-axis (22-28) °C. This reveals the anisotropic behavior by implying that the conducting mechanisms in the two orientations of the crystal are different. The hopping mechanism is followed by the low  $E_A$  in the direction of the long crystal axis. A distinct process is indicated in the orthogonal direction, which suggests surface water sorbate layers allow diffusion to occur at the crystal surface, most probably due to oxonium ( $\text{H}_3\text{O}^+$ ) ion. Moreover, the crystal structure analysis also confirms the presence of channels along the c-axis that can accommodate the water molecules (see Figure 9 in section 5.1.2).

Similarly, the proton conduction mechanism was investigated for Co-MOF single crystal in the two orientations in the temperature range (21-30) °C. The crystal structure study exposes the presence of 1-dimensional hexagonal micropores along the long axis of the crystal named as c-axis (see Figure 1 in section 5.2.2). As anticipated, the proton conduction along the c-axis has  $E_A$  of 0.37 eV, while the orthogonal direction to the c-axis has  $E_A$  of 0.87 eV. A different crystal, measured in the c direction at (30-60) °C, showed again  $E_A$  of 0.32 eV (see Figure 7 in section 5.2.2). Both  $E_A$  values along the micropores fall within the experimental error range. The evidence from this study signifies that proton conduction along the c-axis is mediated by the hopping mechanism (similar to the Grotthuß mechanism). The large value of  $E_A$  in the direction perpendicular to the long crystal axis is due to water molecules adsorption on the crystal surface, which follows the proton diffusion mechanism.

Finally, the pressed pellets of Mg-CP and Pb-MOF were subjected to temperature increase (22-35) °C to visualize the proton conducting mechanism. Prior to and after thermal activation, Mg-CP has  $E_A$  of 0.4 eV and 0.38 eV, respectively. This finding points to the mechanism in which non-coordinated sulfonate groups form dense H-bonding network with coordinated or non-coordinated water molecules, resulting in proton hopping. The second additional conducting mode, which emerged at ca. 10<sup>2</sup> Hz frequency only before activation (see Figure 4 in section 5.3.2), has a diffusion mechanism ( $E_A$  = 0.64 eV), confirming our grain boundary effect hypothesis. In case of Pb-MOF, the difference in  $E_A$  from 0.17 eV to 0.36 eV, as well as

the presence of coordinated sulfonate group (no free sulfonate chain available because it is coordinated to  $\text{Pb}^{+2}$ ), suggest that H-bonding network exists exclusively between non-coordinated water molecules (see Figure 1 and 6 in section 5.3.2).

## 6.2 Challenges and Perspectives

This research eradicates some of the major issues that the proton conducting materials community is dealing with. Although the requisite proton conductivity of  $10^{-2} \text{ S cm}^{-1}$  was not achieved at room temperature, significant efforts have been dedicated to meet the urgent need for single crystal proton conducting mechanism research. The use of a high-quality crystal of an acceptable size, its handling, and establishing electrical contact without additives are key issues when conducting these types of experiments. In this regard, two papers were successfully published. Because current impedance response is taken into consideration in the steady state, a large number of samples could not be analyzed. Because of this, it took many hours between measurements for equilibrium to become established. Furthermore, a dust-free atmosphere can improve the probability of data reproducibility, and here is reported a 10% standard deviation in reproducibility.

Another primary issue is to use a suitable ECM to produce accurate impedance data fitting. Due to the same time constant in complex systems, two separate phenomena can sometimes superimpose. As a result, two separate semicircles are difficult to discern with the naked eye. This phenomenon was demonstrated in this investigation, when employed pressed pellets. As a result, the Bode plot was adopted as another option for confirming the number of semicircles in a measurement. Furthermore, the DC conductivity determined by this method was corroborated by AC conductivity, which showed a plateau in the same range as the conductivity determined by the prior method.

In my view, the sample's stability under operating conditions, such as water stability, should be given specific attention. Secondly, sample decomposition must be considered. These two aspects are noticeable during impedance measurements with a significant shift in conductivity. Furthermore, a postmortem assessment of samples using PXRD and elemental analysis can recognize whether or not sample dissolution or phase transformation have occurred. Another strategy, employed in this research work, was to examine the samples prior to impedance measurements using the PXRD technique under the same conditions.

Based on the experimental results of this study and recent advancements in proton conducting MOFs and CPs materials, following are some of the vital factors to boost their proton conductivity:

- by molecular design of organic ligands that include several sulphonate groups and produce hydrophilic pores of suitable size
- through post-synthetic modification by introducing more free sulfonic acid groups and non-coordinated water molecules into the crystal lattice, which will increase proton carrier concentration
- via adding other additional functional groups to the organic ligand to increase the water stability of sulphonate-based compounds
- using those metal centers having high coordination number and hydrophilic characteristics

Mixed matrix-membrane is the only method to use these materials in real-world applications, such as PEM fuel cell membranes. Therefore, one of the most important demanding characteristics of these composites is their robustness. MEAs should be prepared and tested in PEM fuel cells in massive volumes. Furthermore, under hydration and dehydration regimes, these novel membranes must be able to withstand temperature range (22-80) °C. An ideal membrane or material that meet all the requisite parameters must function at room temperature without humidity, which is a future goal.

## Bibliography

- [1] Y. Sakamaki, M. Tsuji, Z. Heidrick, O. Watson, J. Durchman, C. Salmon, S. R. Burgin, M. Hassan Beyzavi, *J. Chem. Educ.* **2020**, *97*, 1109–1116.
- [2] R. Freund, O. Zaremba, G. Arnauts, R. Ameloot, G. Skorupskii, M. Dincă, A. Bavykina, J. Gascon, A. Ejsmont, J. Goscianska, M. Kalmutzki, U. Lächelt, E. Ploetz, C. S. Diercks, S. Wuttke, *Angew. Chem., Int. Ed.* **2021**, *60*, 23975–24001.
- [3] X. Shi, Y. Shan, M. Du, H. Pang, *Coord. Chem. Rev.* **2021**, *444*, 214060.
- [4] A. Radwan, H. Jin, D. He, S. Mu, *Nano-Micro Lett.* **2021**, *13*, 132.
- [5] C. Belver, J. Bedia, *J. Catal.* **2021**, *11*, 4–7.
- [6] P. Ramaswamy, N. E. Wong, G. K. H. Shimizu, *Chem. Soc. Rev.* **2014**, *43*, 5913–5932.
- [7] X. S. Xing, Z. H. Fu, N. N. Zhang, X. Q. Yu, M. S. Wang, G. C. Guo, *Chem. Commun.* **2019**, *55*, 1241–1244.
- [8] B. Joarder, J. Bin Lin, Z. Romero, G. K. H. Shimizu, *J. Am. Chem. Soc.* **2017**, *139*, 7176–7179.
- [9] S. S. Bao, K. Otsubo, J. M. Taylor, Z. Jiang, L. M. Zheng, H. Kitagawa, *Journal of the American Chemical Society* **2014**, *136*, 9292–9295.
- [10] W. X. Chen, H. R. Xu, G. L. Zhuang, L. S. Long, R. Bin Huang, L. S. Zheng, *Chem. Commun.* **2011**, *47*, 11933–11935.
- [11] R. Li, S. H. Wang, X. X. Chen, J. Lu, Z. H. Fu, Y. Li, G. Xu, F. K. Zheng, G. C. Guo, *Chem. Mater.* **2017**, *29*, 2321–2331.
- [12] S. Tominaka, A. K. Cheetham, *RSC Adv.* **2014**, *4*, 54382–54387.
- [13] D. Umeyama, S. Horike, M. Inukai, T. Itakura, S. Kitagawa, *J. Am. Chem. Soc.* **2012**, *134*, 12780–12785.
- [14] X. Zhao, C. Mao, X. Bu, P. Feng, *Chem. Mater.* **2014**, *26*, 2492–2495.
- [15] G. A. Jones, K. J. Warner, *Energy Policy* **2016**, *93*, 206–212.
- [16] United Nations, Department of Economic and Social Affairs, Population Division (2019),

*World Population Prospects 2019, 2019.*

- [17] B. Walsh, P. Ciais, I. A. Janssens, J. Peñuelas, K. Riahi, F. Rydzak, D. P. van Vuuren, M. Obersteiner, *Nature Communications* **2017**, *8*, 14856.
- [18] International Energy Agency, *IEA (2021), World Energy Outlook 2021*, Paris, France, **2021**.
- [19] G. Zachmann, M. Holtermann, J. Radeke, M. Tam, M. Huberty, D. Naumenko, A. Ndoye, *The Great Transformation: Decarbonising Europe's Energy and Transport Systems*, Brussels, Belgium, **2012**.
- [20] A. Arshad, H. M. Ali, A. Habib, M. A. Bashir, M. Jabbal, Y. Yan, *Therm. Sci. Eng. Prog.* **2019**, *9*, 308–321.
- [21] G. Xing, L. Wang, H. Fu, *Energy Technol.* **2021**, *9*, 1–18.
- [22] A. G. Olabi, T. Wilberforce, M. A. Abdelkareem, *Energy* **2021**, *214*, 118955.
- [23] O. Z. Sharaf, M. F. Orhan, *Renew. Sust. Energ. Rev.* **2014**, *32*, 810–853.
- [24] W. H. Tanveer, H. Rezk, A. Nassef, M. A. Abdelkareem, B. Kolosz, K. Karuppasamy, J. Aslam, S. O. Gilani, *Energy* **2020**, *204*, 117976.
- [25] A. M. Nassef, A. Fathy, E. T. Sayed, M. A. Abdelkareem, H. Rezk, W. H. Tanveer, A. G. Olabi, *Renew. Energy* **2019**, *138*, 458–464.
- [26] S. P. Jiang, Q. Li, *Introduction to Fuel Cells*, Springer, Singapore, **2022**.
- [27] M. M. Tellez-Cruz, J. Escorihuela, O. Solorza-Feria, V. Compañ, *Polymers* **2021**, *13*, 3064.
- [28] S. Khosravi H, Q. Abbas, K. Reichmann, *Int. J. Hydrogen Energy* **2021**, *46*, 35420–35447.
- [29] F. N. Büchi, M. Inaba, T. J. Schmidt, Eds. , *Polymer Electrolyte Fuel Cell Durability*, Springer New York, New York, NY, **2009**.
- [30] F. Maillard, P. A. Simonov, E. R. Savinova, in *Carbon Materials for Catalysis*, John Wiley & Sons, Inc., Hoboken, NJ, USA, **2008**, pp. 429–480.
- [31] J. Durst, A. Siebel, C. Simon, F. Hasché, J. Herranz, H. A. Gasteiger, *Energy Environ. Sci.* **2014**, *7*, 2255–2260.

[32] H. A. Gasteiger, S. S. Kocha, B. Sompalli, F. T. Wagner, *Appl. Catal. B* **2005**, *56*, 9–35.

[33] M. F. Mathias, J. Roth, J. Fleming, W. Lehnert, in *Handbook of Fuel Cells*, John Wiley & Sons, Ltd, Chichester, UK, **2010**.

[34] N. Esmaeili, E. M. Gray, C. J. Webb, *ChemPhysChem* **2019**, cphc.201900191.

[35] Y. Ye, L. Gong, S. Xiang, Z. Zhang, B. Chen, *Adv. Mater.* **2020**, *32*, 1907090.

[36] Y. Wang, K. S. Chen, J. Mishler, S. C. Cho, X. C. Adroher, *Appl. Energy* **2011**, *88*, 981–1007.

[37] K. A. Mauritz, R. B. Moore, *Chem. Rev.* **2004**, *104*, 4535–4586.

[38] M. Casciola, G. Alberti, M. Sganappa, R. Narducci, *J. Power Sources* **2006**, *162*, 141–145.

[39] S. Wang, G. Zhang, M. Han, H. Li, Y. Zhang, J. Ni, W. Ma, M. Li, J. Wang, Z. Liu, L. Zhang, H. Na, *Int. J. Hydrogen Energy* **2011**, *36*, 8412–8421.

[40] A. Carbone, R. Pedicini, G. Portale, A. Longo, L. D’Ilario, E. Passalacqua, *J. Power Sources* **2006**, *163*, 18–26.

[41] E. G. Sorte, B. A. Paren, C. G. Rodriguez, C. Fujimoto, C. Poirier, L. J. Abbott, N. A. Lynd, K. I. Winey, A. L. Frischknecht, T. M. Alam, *Macromolecules* **2019**, *52*, 857–876.

[42] M. Adamski, T. J. G. Skalski, B. Britton, T. J. Peckham, L. Metzler, S. Holdcroft, *Angew. Chem., Int. Ed.* **2017**, *56*, 9058–9061.

[43] K. Shiino, T. Otomo, T. Yamada, H. Arima, K. Hiroi, S. Takata, J. Miyake, K. Miyatake, *ACS Appl. Polym. Mater.* **2020**, *2*, 5558–5565.

[44] J. Escorihuela, J. Olvera-Mancilla, L. Alexandrova, L. F. del Castillo, V. Compañ, *Polymers* **2020**, *12*, 1861.

[45] D. Aili, D. Henkensmeier, S. Martin, B. Singh, Y. Hu, J. O. Jensen, L. N. Cleemann, Q. Li, *EER* **2020**, *3*, 793–845.

[46] J. Escorihuela, A. García-Bernabé, V. Compañ, *Polymers* **2020**, *12*, 1374.

[47] A. Verma, K. Scott, *J. Solid State Electrochem.* **2010**, *14*, 213–219.

[48] H. Pu, W. H. Meyer, G. Wegner, *J. Polym. Sci. B Polym. Phys.* **2002**, *40*, 663–669.

[49] X. Glipa, B. Bonnet, B. Mula, D. J. Jones, J. Rozière, *J. Mater. Chem.* **1999**, *9*, 3045–3049.

[50] R. Bouchet, *Solid State Ion.* **1999**, *118*, 287–299.

[51] J. . Fontanella, M. . Wintersgill, J. . Wainright, R. . Savinell, M. Litt, *Electrochim. Acta* **1998**, *43*, 1289–1294.

[52] J. Escorihuela, R. Narducci, V. Compañ, F. Costantino, *Adv. Mater. Interfaces* **2018**.

[53] S. R. Batten, N. R. Champness, X.-M. Chen, J. Garcia-Martinez, S. Kitagawa, L. Öhrström, M. O’Keeffe, M. Paik Suh, J. Reedijk, *Pure Appl. Chem.* **2013**, *85*.

[54] N. F. H. Nik Zaiman, N. Shaari, N. A. M. Harun, *Int. J. Energy Res.* **2021**.

[55] D.-W. Lim, H. Kitagawa, *Chem. Rev.* **2020**, *120*, 8416–8467.

[56] G. Zhang, L. Jin, R. Zhang, Y. Bai, R. Zhu, H. Pang, *Coord. Chem. Rev.* **2021**, *439*, 213915.

[57] S. Sanda, S. Biswas, S. Konar, *Inorg. Chem.* **2015**, *54*.

[58] M. Yoon, K. Suh, S. Natarajan, K. Kim, *Angew. Chem., Int. Ed.* **2013**, *52*, 2688–2700.

[59] K. Biradha, A. Goswami, R. Moi, S. Saha, *Dalton Trans.* **2021**, *50*, 10655–10673.

[60] S.-S. Bao, G. K. H. Shimizu, L.-M. Zheng, *Coord. Chem. Rev.* **2019**, *378*.

[61] W.-H. Li, W.-H. Deng, G.-E. Wang, G. Xu, *EnergyChem.* **2020**, *2*, 100029.

[62] X.-X. Xie, Y.-C. Yang, B.-H. Dou, Z.-F. Li, G. Li, *Coord. Chem. Rev.* **2020**, *403*, 213100.

[63] X. Fang, Q. Fernando, S. O. Ugwu, J. Blanchard, *Pharm. Res.* **1995**, *12*, 1423–1429.

[64] M. Namazian, S. Halvani, *J. Chem. Thermodyn.* **2006**, *38*, 1495–1502.

[65] T. Bock, H. Möhwald, R. Mülhaupt, *Macromol. Chem. Phys.* **2007**, *208*, 1324–1340.

[66] R. Liu, W. Qu, B. Dou, Z. Li, G. Li, *Asian J. Chem.* **2020**, *15*, 182–190.

[67] Nikolai Bagdassarov, in *Fundamentals of Rock Physics*, Cambridge University Press, **2021**, pp. 292–360.

[68] J. Owen, in *Comprehensive Polymer Science and Supplements*, Elsevier, **1989**, pp. 669–686.

[69] J.-H. Fang, in *Advanced Polyimide Materials*, Elsevier, **2018**, pp. 323–383.

[70] C. O. Colpan, Y. Nalbant, M. Ercelik, in *Comprehensive Energy Systems*, Elsevier, **2018**, pp. 1107–1130.

[71] T. M. Lim, M. Ulaganathan, Q. Yan, in *Advances in Batteries for Medium and Large-Scale Energy Storage*, Elsevier, **2015**, pp. 477–507.

[72] S. B. Aziz, Z. H. Z. Abidin, *J. Soft Matter* **2013**, *2013*, 1–8.

[73] Z. Osman, K. B. M. Isa, L. Othman, N. Kamarulzaman, *Defect Diffus. Forum* **2011**, *312–315*, 116–121.

[74] K. W. Dawson, PhD Thesis, Modification of Proton Conducting Metal-Organic Frameworks for Improved Performance in Fuel Cell Applications, **2013**.

[75] X. Deng, J.-Y. Hu, J. Luo, W.-M. Liao, J. He, *Top. Curr. Chem.* **2020**, *378*, 27.

[76] Z. Zuo, Y. Fu, A. Manthiram, *Polymers* **2012**, *4*, 1627–1644.

[77] N. Agmon, *Chem. Phys. Lett.* **1995**, *244*, 456–462.

[78] K.-D. Kreuer, A. Rabenau, W. Weppner, *Angew. Chem., Int. Ed.* **1982**, *21*, 208–209.

[79] D. I. Kolokolov, D. Lim, H. Kitagawa, *Chem. Rec.* **2020**, *20*, 1297–1313.

[80] S. Cukierman, *Biochim. Biophys. Acta - Bioenerg.* **2006**, *1757*, 876–885.

[81] M. Aljarrah, F. Salman, *J. Inst. Eng. India Ser. D* **2021**, *102*, 237–242.

[82] M. E. Orazem, *J. Solid State Electrochem.* **2020**, *24*, 2151–2153.

[83] M. E. Orazem, B. Tribollet, *ChemTexts.* **2020**, *6*, 12.

[84] S. Wang, J. Zhang, O. Gharbi, V. Vivier, M. Gao, M. E. Orazem, *Nat. Rev. Methods Primers* **2021**, *1*, 41.

[85] A. I. Zia, S. C. Mukhopadhyay, in *Electrochemical Sensing: Carcinogens in Beverages*, Springer, Cham, Switzerland, **2016**, pp. 21–37.

[86] X.-Z. Yuan, C. Song, H. Wang, J. Zhang, *Electrochemical Impedance Spectroscopy in PEM Fuel Cells*, Springer, London, UK, **2010**.

[87] E. Barsoukov, J. R. Macdonald, *Impedance Spectroscopy*, John Wiley & Sons, Inc., Hoboken, NJ, USA, **2018**.

[88] E. Bogatin, *Signal and Power Integrity*, Prentice Hall PTR, Upper Saddle River, NJ, United States, **2010**.

[89] E. Von Hauff, *J. Phys. Chem. C* **2019**, *123*, 11329–11346.

[90] D. K. Singh, M. Pradhan, A. Materny, *Modern Techniques Of Spectroscopy*, Springer, Singapore, **2021**.

[91] E. Stavrinidou, M. Sessolo, B. Winther-Jensen, S. Sanaur, G. G. Malliaras, *AIP Adv.* **2014**, *4*, 017127.

[92] C. H. Chan, H. W. Kammer, *Ionics* **2017**, *23*, 2327–2337.

[93] D. Sharon, P. Bennington, C. Liu, Y. Kambe A Ban, X. Dong, V. Burnett, M. Dolejsi, G. Grocke, S. N. Patel, P. F. Nealey, *J. Electrochem. Soc.* **2018**, *165*, H1028–H1039.

[94] C. H. Chan, H.-W. Kammer, *Pure Appl. Chem.* **2018**, *90*, 939–953.

[95] M. A. Careem, I. S. M. Noor, A. K. Arof, in *Polymer Electrolytes*, **2020**, pp. 23–64.

[96] E. Barsoukov, Macdonald. J. Ross, *Impedance Spectroscopy*, John Wiley & Sons, Inc., Hoboken, NJ, USA, **2005**.

[97] A. Schönhals, F. Kremer, *Broadband Dielectric Spectroscopy*, Springer , Berlin, Heidelberg, Germany, **2003**.

[98] S. Wöhlbrandt, A. Igleska, E. Svensson Grape, S. Øien-Ødegaard, A. Ken Inge, N. Stock, *Dalton Trans.* **2020**, *49*, 2724–2733.

[99] P. D. C. Dietzel, Y. Morita, R. Blom, H. Fjellvåg, *Angew. Chem., Int. Ed.* **2005**, *44*, 6354–6358.

[100] P. Ehrlich, N. J. De, *J. Res. Natl. Bur. Stand.* **1953**, *51*, 185–188.

[101] H. Li, Y. Zhou, Y. Liu, L. Li, Y. Liu, Q. Wang, *Chem. Soc. Rev.* **2021**, *50*, 6369–6400.

[102] Multi Circuit Boards Ltd., Germany, **n.d.**

[103] F. Niekiel, N. Stock, *Cryst. Growth Des.* **2014**, *14*, 599–606.

## List of Tables

Table 2.1: Characteristics of different types of fuel cells based on electrolyte material .....	5
Table 3.1: Ideal circuit elements with basic description and impedance. ....	21
Table 3.2: Phase angle, real and imaginary parts of impedance derived from series and parallel combination of $R$ and $C$ .....	23
Table 3.3: Definition of coefficient $Q$ based on $n$ .....	25
Table 5.1.1. Summary of fittings produced using the equivalent circuit model for Ba-CP, and the calculated proton conductivities at distinct setpoints of relative humidity and temperature, and in particular at different orientations of crystals relative to IDE. ....	42
Table 5.2.1. Description of the fittings produced using the equivalent circuit model for Co-MOF-74, at different setpoints of relative humidity and temperature, specifically for crystal orientation with respect to IDE.....	56
Table 5.3.1. An overview of fittings produced using equivalent circuit models for compounds Mg-CP and Pb-MOF, as well as calculations of proton conductivities at multiple temperatures and relative humidity setpoints. ....	72
Table 5.4.1: Dimensions of layouts, empty electrode capacity constant $C_e$ and permittivity $\epsilon_{r(\text{sub})}$ of the substrate material of the FEF sensor, calculated from measured capacitances..	77

## List of Figures

Figure 1.1: Chronological advancement on publications of MOFs and CPs: a) in all possible sectors, b) in proton conductance world (ISI Web of Science, accessed 18.01.2022). ....	1
Figure 2.1: Flow diagram presenting the comparison of energy generation by conventional method and electrochemical process. ....	4
Figure 2.2: Schematic diagram presenting the operating principle of single PEMFC. ....	6
Figure 2.3: Schematic structure of 1D, 2D and 3D coordination networks. ....	9
Figure 2.4: Schematic illustration of MOFs to regulate proton conductivity. ....	10
Figure 2.5: Schematic representation of impedance measurement methods a) through-plane and b) in-plane. ....	13
Figure 2.6: Schematic representation of the Grotthuß Mechanism (top), in which protons transfer along hydrogen bonds, and the vehicle Mechanism (bottom), in which protons travel in solvated form, like $\text{H}_3\text{O}^+$ . General color scheme: O: red, H: blue, H-Bonds: black dotted line arrow. ....	15
Figure 2.7: Schematic diagram of proton conduction via hydrogen bonds in bulk water. General color scheme: O: red, H: green (1 <sup>st</sup> $\text{H}_2\text{O}$ molecule), H: blue (2 <sup>nd</sup> $\text{H}_2\text{O}$ molecule), H: gold (3 <sup>rd</sup> $\text{H}_2\text{O}$ molecule), H: gray (4 <sup>th</sup> $\text{H}_2\text{O}$ molecule), H-Bonds: black dotted line. ....	16
Figure 3.1: Schematic representation of black box subjected to a sinusoidal signal with frequency ( $\omega$ ). ....	17
Figure 3.2: Phase diagram between response current $I(t)$ and applied excitation potential $U(t)$ . General color scheme of sinusoidal waves: black: applied potential, green: response current after passing through resistor ( $I_R$ ), blue: response current after passing through inductor ( $I_L$ ), red: response current after passing through capacitor ( $I_C$ ). The dotted lines display the peaks position. ....	19
Figure 3.3: Complex plane representing a frequency dependent single data point of $Z$ . ....	20
Figure 3.4: Graphical representation of $RC$ circuits in complex plane: left) serial, right) parallel. The black solid vertical line and curve show the exemplary data points, and red dotted vertical line and curve depict fittings produced by ECM. ....	22
Figure 3.5: Typical $RC$ circuit arrangements in complex planes and respective ECMS to fit the data. ....	24
Figure 3.6: Graphical representation of change in impedance spectra with respect to exponent $n$ in complex plane when: left) $R$ and CPE are in series, right) $R$ and CPE in parallel. ....	25

Figure 4.1: Schematic diagram of laboratory test bench for single crystal impedance measurement. ....	28
Figure 4.2: Substrate with interdigital electrodes for impedance measurements of single crystals (left); the measurement is carried out in a Faraday cage (middle) that is placed in a climate chamber with temperature and humidity control (right). ....	29
Figure 4.3: top) Solartron SI 1260 with Chelsea Interface, middle) Alpha-A Analyzer setup, and bottom) ZG4 Interface connection to cell placed inside climate chamber. ....	30
Figure 4.4: Schematic diagram of laboratory test bench for pressed pellets impedance measurement. ....	31
Figure 4.5: left) top-view of cell, middle) exemplary sample placed between the electrodes, and right) cell placed inside the climate chamber. ....	31
Figure 5.2.1. Nyquist plots for single crystal Co-MOF-74 samples (a) Co-74_2: along c-axis at 21 °C and 70 % ... 90 % rh (b) Co-74_3: along c-axis at 90 % rh and 22 °C ... 30 °C temperature (c) Co-74_4: along orthogonal direction at 90 % rh and 21 °C ... 30 °C temperature.....	57
Figure 5.2.2. Nyquist plots for single crystal Co-MOF-74 sample, Co-74_5 along c-axis (a) at 30 °C and 70 % ... 95 % rh (b) zoom-in view of (a), and (c) zoom-in view of (b), and (d) at 90 % rh and 30 °C ... 60 °C temperature.....	58
Figure 5.3.1. Nyquist plots for compound Mg-CP before and after thermal activation of sample at (a) 22 °C and 70 % rh (b) 22 °C and 75 % rh (c) 22 °C and 80 % rh (d) 22 °C and 85 % rh (e) 90 % rh and 22 °C ... 35 °C before thermal activation (f) 90 % rh and 22 °C ... 35 °C after thermal activation.....	73
Figure 5.3.2. Nyquist plots for compound Pb-MOF before and after thermal activation of sample at (a) 22 °C and 70 % ... 90 % rh before activation (b) 90 % rh and 22 °C ... 35 °C before thermal activation (c) 90 % rh and 22 °C ... 35 °C after thermal activation. ....	74
Figure 5.4.1: Conception of a fringing electric field (FEF) sensor. ....	75
Figure 5.4.2: Simulation results of probe (a) without backplane (b) with backplane (c) with backplane and additional guard ring between electrodes. The simulation is done with empty probe in the presence of air as an environment.....	76
Figure 5.4.3: Photographs of layouts of FEF sensors. ....	77
Figure 5.4.4: Capacitance values of pure water, Teflon, and dry air, measured with the FEF sensor. ....	78
Figure 5.4.5: Mixed matrix membrane placed on the FEF probe. ....	78

Figure 5.4.6: Impedance of the membrane (Nyquist plot; 23 °C, 90 % rh, 11 Hz - 1 MHz, 0.5 V).	79
Figure 5.4.7: Proton resistance of the membrane at variable relative humidity and temperature.	79

## Appendix

### List of Publications

---

**2022** Colossal increase in ionic conductivity for a polymer electrolyte, induced by Magic-Angle-Spinning  
Waldemar Keil, Ali Javed, Hossam Elgabarty, Christian Weinberger, Michael Tiemann, Claudia Schmidt  
(DOI: [to be submitted](#))

---

**2022** The Role of Sulfonate Groups and Hydrogen Bonding in the Proton Conductivity of Two Coordination Networks  
Ali Javed, Felix Steinke, Stephan Wöhlbrandt, Hana Bunzen, Norbert Stock, and Michael Tiemann  
(DOI: [10.3762/bjnano.13.36](https://doi.org/10.3762/bjnano.13.36))

---

**2021** New isoreticular phosphonate MOFs based on a tetratopic linker  
Felix Steinke, Ali Javed, Stephan Wöhlbrandt, Michael Tiemann, Norbert Stock  
(DOI: [10.1039/D1DT02610K](https://doi.org/10.1039/D1DT02610K))

---

**2020** Humidity-Mediated Anisotropic Proton Conductivity through the 1D Channels of Co-MOF-74  
Ali Javed, Ina Strauss, Hana Bunzen, Jürgen Caro, Michael Tiemann  
(DOI: [10.3390/nano10071263](https://doi.org/10.3390/nano10071263))

---

**2020** Proton Conduction in a Single Crystal of a Phosphonato-Sulfonate-Based Coordination Polymer: Mechanistic Insight  
Ali Javed, Thorsten Wagner, Stephan Wöhlbrandt, Norbert Stock, Michael Tiemann  
(DOI: [10.1002/cphc.202000102](https://doi.org/10.1002/cphc.202000102))

---

**2020** Chemical and Morphological Transition of Poly(acrylonitrile)/Poly(vinylidene Fluoride) Blend Nanofibers during Oxidative Stabilization and Incipient Carbonization  
Martin Wortmann, Natalie Frese, Al Mamun, Marah Trabelsi, Waldemar Keil, Björn Büker, Ali Javed, Michael Tiemann, Elmar Moritzer, Andrea Ehrmann, Andreas Hütten, Claudia Schmidt, Armin Gölzhäuser, Bruno Hüsgen, Lilia Sabantina  
(DOI: [10.3390/nano10061210](https://doi.org/10.3390/nano10061210))

---

**2018** Anisotropic Water-Mediated Proton Conductivity in Large Iron(II) Metal-Organic Framework Single Crystals for Proton-Exchange Membrane Fuel Cells  
Hana Bunzen, Ali Javed, Danielle Klawinski, Anton Lamp, Maciej Grzywa, Andreas Kalytta-Mewes, Michael Tiemann, Hans-Albrecht Krug von Nidda, Thorsten Wagner, Dirk Volkmer  
(DOI: [10.1021/acsanm.8b01902](https://doi.org/10.1021/acsanm.8b01902))

---

## List of Posters

---

<b>2021</b>	New isoreticular phosphonate MOFs based on a tetratopic linker <u>Felix Steinke, Ali Javed, Stephan Wöhlbrandt, Michael Tiemann, Norbert Stock</u>  33. German Zeolite Conference, Frankfurt am Main, Germany
<b>2020</b>	Humidity-mediated Proton Conductivity through the 1D Channels of Co-MOF-74 <u>Ali Javed, Ina Strauss, Hana Bunzen, Jürgen Caro, Michael Tiemann</u>  Jung-Chemiker-Forum GDCh, Paderborn, Germany
<b>2019</b>	Anisotropic Proton Conduction Properties of a Coordination Polymer Studied by Impedance Spectroscopy <u>Ali Javed, Stephan Wöhlbrandt, Nobert Stock, Thorsten Wagner, Michael Tiemann</u>  31. German Zeolite Conference, Dresden, Germany
<b>2019</b>	Humidity Dependent Proton Conduction Study of Coordination Polymers by Impedance Imaging Approach <u>Ali Javed, Stephan Wöhlbrandt, Nobert Stock, Konrad Wolkersdörfer, Michael Wark, Thorsten Wagner, Michael Tiemann</u>  COORNets Doctoral Symposium 2019, TUM-CRC, Germany
<b>2018</b>	Impedance of Metal-Organic Framework Single Crystals <u>Ali Javed, Danielle Klawinski, Thomas Homburg, Nobert Stock, Michael Tiemann, Thorsten Wagner</u>  1. European Doctoral Symposium on MOFs 2018, Raitenhaslach, Germany

---

## Oral Presentations

---

<b>2021</b>	Anisotropic Proton Conduction in Metal-Organic Frameworks (MOFs) and Coordination Polymers (CPs) <u>Ali Javed, Stephan Wöhlbrandt, Nobert Stock, Ina Strauss, Jürgen Caro, Hana Bunzen, Michael Tiemann</u>  32. German Zeolite Conference, Online, Germany
-------------	--

---

## Workshops

---

<b>2019</b>	At the heart of MOF chemistry: Topology Technical University of Munich, Germany
<b>2018</b>	Broadband Dielectric and Electrochemical Impedance Spectroscopy Novocontrol Technologies GmbH & Co. KG, Montabaur, Germany
<b>2018</b>	Electrochemical and electrical characterization of films of coordination network compounds Carl von Ossietzky University of Oldenburg, Germany
<b>2017</b>	COORNets Workshop Wissenschaftszentrum Schloss Reisensburg, Germany

---

# Curriculum Vitae

## ALI JAVED

Date of Birth 01.01.1986

Place of Birth Chak Jhumra Faisalabad, Pakistan

## QUALIFICATION

<b>2017-2022</b>	University of Paderborn, Germany PhD in Natural Science (Inorganic and Analytical Chemistry) Thesis: Proton Conduction in Metal-Organic Frameworks and Coordination Polymers Studied by Impedance Spectroscopy Advisor: Prof. Dr. Michael Tiemann
<b>2012-2015</b>	Otto von Guericke University, Magdeburg, Germany Master in Chemical and Energy Engineering Thesis: Investigation of Redox/Catalytic Properties of Novel Formulation for Solid Oxide Fuel Cell Anode Advisors: Dr. Aitor Hornes (German Aerospace Center, Stuttgart) Dr. Abdolreza Kharaghani (Otto von Guericke University, Magdeburg)
<b>2004-2008</b>	University of Engineering and Technology, Lahore, Pakistan Bachelor in Chemical Engineering Major Thesis: Production of Ammonia from Coal Design Thesis: Designing and Fabrication of Spiral Coil and Transparent Shell Heat Exchanger Advisors: Dr. Shahid Raza Malik Engr. Muhammad Tahir Ishfaq
<b>2002-2004</b>	Govt. Higher Secondary School, Chak Jhumra Faisalabad, Pakistan Pre-Engineering (Chemistry, Physics and Mathematics)
<b>2000-2002</b>	Govt. Higher Secondary School, Chak Jhumra Faisalabad, Pakistan Matriculation (Science)